SMA Actuator Priming using Resistance Feedback

by

Mohamed El Dib

A thesis
presented to the University of Waterloo
in fulfillment of the
thesis requirement for the degree of
Master of Applied Science
in
Electrical & Computer Engineering

Waterloo, Ontario, Canada, 2010

I hereby declare that I am the sole author of this thesis. This is a true copy of the thesis, including any required final revisions, as accepted by my examiners.

I understand that my thesis may be made electronically available to the public.

Abstract

Shape memory alloys (SMAs) are a group of alloys that demonstrate the unique ability of returning back to a previously defined shape or size if subjected to the appropriate thermal procedure. They have been implemented as actuators in a wide range of applications spanning several fields such as robotics, aeronautics, automotive and even in medicine. Several controllers, linear and nonlinear, have been designed to control these actuators. However, controlling these actuators is no simple task as they are highly nonlinear due to the hysteresis inherent in them. In fact, their control depends on two important factors: the thermal conditions they are subjected to and the stress applied to them. The former can be further divided into air flow and ambient temperatures. These thermal conditions determine the amount of power needed to heat the SMA wire. In the SMA data sheets, manufacturers specify what they refer to as the "*safe current*" which is the maximum current value that can be applied to the SMA wire indefinitely without burning it. However, they specify this current value at room temperature and under certain convection conditions. In the work presented here, the focus was the control of SMA actuators under different ambient temperatures. Thus, in this research, the main goal was to design and implement a controller that will actuate, or contract, the SMA wire in approximately the same amount of time regardless of the ambient temperatures with a fixed load applied to it.

Acknowledgements

I would like to thank several people for their support during my graduate studies. First and foremost, I would like to thank my supervisor, Professor Rob Gorbet, not only for his mentorship and guidance, but also for his assistance since the very first day I arrived in Canada.

I would also like to extend my thanks and gratitude to Dr. Eric Kubica and Mr. Kevin Krauel for their assistance with my research. Most importantly, I would like to thank them for their friendship.

Many thanks are due to my colleagues: Li Wang, Shailaja Sajja and Brandon DeHart for their support during the past two and a half years.

Also, I would like to thank our collaborators from GM: Dr. Jay Gao, Dr. Nancy Johnson, Dr. Alan Browne and Mr. Nicholas Pinto.

Finally, I would like to thank the most important people in my life for their continuous support and encouragement throughout the years: my mother, my brother and my wife. And last but not least, my little angel Hoda for all the joy she has brought into my life.

To my late father . . .

Contents

List of Tables

List of Figures

Chapter 1

Introduction

Shape memory alloys (SMAs) are a group of metallic materials that demonstrate the ability of returning back to a previously defined shape or size if subjected to the appropriate thermal procedure. There are several examples of SMAs. These include Ag-Cd, Au-Cd, Cu-Al-Ni, Cu-Sn, Ni-Al, Ni-Ti and Mn-Cu. Of all these alloys, Ni-Ti, also referred to as Nitinol, is the most widely used. This is because it is typically less expensive, easier to work with and also safer to work with from a health standpoint [1]. SMAs are metals that exhibit two unique properties: shape memory effect and pseudo-elasticity. These properties are best described in terms of a solid state phase transformation that occurs in shape memory alloys between two states known as martensite and austenite.

SMAs have gained popularity in actuator design because they enjoy several desirable characteristics. These include high recovery stress [2] which enables the production of large forces [3], tolerance to high strain [2], and high strength-to-weight ratio that makes it suitable for miniature actuators [4]. However, the most important advantage of SMAs is probably its simple actuation mechanism. The transformation of the alloy from one state to another can take place either due to a change in temperature (shape memory effect) or a change in the stress applied to it (pseudoelasticity). The investigation conducted in this research is on the control of SMA actuation by regulating the temperature of the SMA wire. This is done by passing a current through it, a method referred to as joule heating.

1.1 Motivation

In their data sheets, SMA manufacturers specify what they refer to as the "*safe current*" which is the maximum current that can actuate the SMA wire indefinitely without damaging it. However, this current is typically specified at room temperature and under specific convection conditions. It will be demonstrated later in this thesis that this so-called "safe" current could be, under specific ambient conditions, insufficient to actuate the SMA wire, and under other conditions too large which will damage it. Even in regimes where this value will actuate the wire safely, the actuation times depend on ambient temperatures.

To avoid the variability associated with using "safe" currents, a different methodology had to be investigated to control SMA actuation. Given the fact that the resistance of SMAs can be used as a self-sensing characteristic to detect phase transformations [5], the behaviour of the resistance, R, of the SMA wire during actuation was investigated. Figure 1.1 shows the resistance response of the wire as it is subjected to a triangular current pulse at room temperature. The resistance, R, first increases as the SMA in martensite phase is heated. It reaches a ***cusp*** just prior to actuation, then goes through the phase transition from martensite to the lower-resistivity austenite phase. Further heating of the austenite material causes another relative increase in resistance, and the process reverses as the current drops and the wire cools again back to martensite. Using this observation, the primary goal of the controllers developed in this research was to detect this cusp in SMA resistance as the wire actuates.

Several researchers have used absolute resistance to control SMA actuators. For example, in [6], Featherstone and Yee use absolute resistance measurements to determine the current needed to heat SMA actuators. However, since these absolute resistance values depend on the stress applied to the wire, variations in the wire and fatigue, implementing a control strategy that aims to detect the cusp would be more beneficial.

1.2 Objective

Consequently, the focus of this research was to develop different ways and methodologies that will result in the *robust actuation* of SMA actuators designed for automotive applications. In this research, *robust actuation* was taken to mean actuating, or contracting, the SMA wire in a consistent period of time across a range of oper-

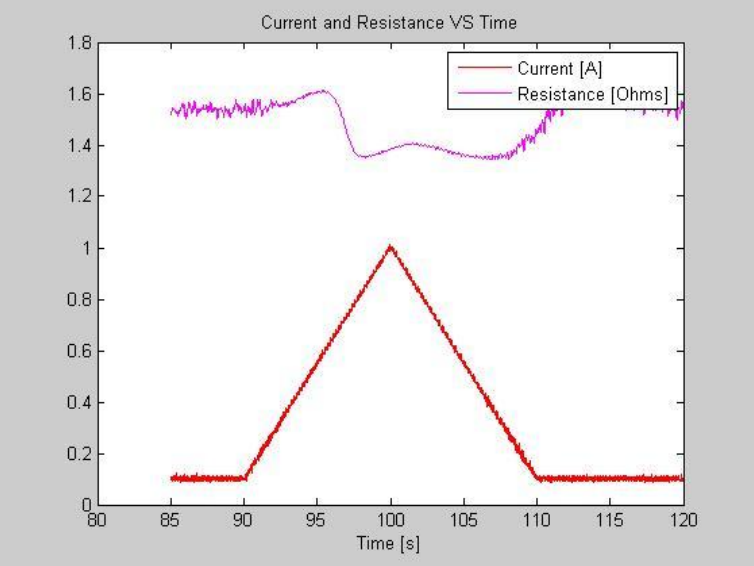

Figure 1.1: Current and resistance vs time for SMA wire during actuation

ating temperatures of interest to automotive applications, by including a priming segment which prepares the wire for actuation. To achieve this goal, a number of different open- and closed-loop priming strategies were developed and tested.

1.3 Outline

The thesis is divided as follows: background information on SMA wires and the literature review are presented in Chapter 2. The chapter is divided into 3 major sections. In Section 2.1, background information on SMA wires is presented: its unique characteristics and its advantages and disadvantages. The different feedback control algorithms that have been implemented by researchers for SMA actuation are discussed in Section 2.2 with each subsection focusing on one of these algorithms: temperature, force, position and electrical resistance. Subsection 2.2.5 states the advantages of using electrical resistance as feedback signal versus other signals with regard to automotive applications. In Section 2.3, the different "priming" and actuation techniques that have been implemented in the literature are presented. The literature review conducted on the actuation techniques developed by other researchers is discussed in Section 2.3.1, while Subsection 2.3.2 discusses the different priming techniques.

However, it should be noted that, in this research, a slightly different definition of priming is used. While all the techniques discussed in Subsection 2.3.2 can be

collectively considered as "fixed" priming techniques i.e. priming techniques that operate under fixed ambient conditions, the goal here is to devise an "adaptive" priming technique that would aid in actuating the SMA wire in approximately the same amount of time regardless of the surrounding ambient conditions. This definition of priming is given in Subsection 2.3.3 along with the actuation technique implemented in this work.

Another important aspect to consider when talking about robust actuation is the robustness of measurements to noise. In previous work [7], a linear-current priming controller was used to actuate the SMA wire. However, it was found that, at low currents, the computed resistance of the SMA wire was adversely affected by noise. Therefore, the prospect of employing PWM signals instead was considered. Several experiments were conducted to compare the results obtained from employing a linear-current priming controller versus a PWM-based priming controller. Chapter 3 discusses the experimental setup used and the results obtained.

Chapter 4 introduces the microcontroller-based embedded system that was built to test the effectiveness of the controller design under various ambient temperatures. Section 4.1 highlights the objective of migrating to a microcontroller-based embedded system from the previous in-lab setup and its advantages. The experimental setup with all its components is detailed in Section 4.2. Section 4.3 discusses the primary experimental results that were obtained. As will be seen later, the obtained results were found to be quite noisy consequently degrading the effectiveness of the proposed controller. Thus, several techniques were developed and tested to help reduce this noise. These are detailed in Subsections 4.3.1-4.3.3.

The development of priming strategies is discussed in Chapter 5. Because ambient conditions affect the currents used in control, the wire undergoes a regular process called "probing" which effectively determines an appropriate actuation current given present conditions. The probing process implemented in this research is explained in Section 5.1. To ensure the proper operation of the closed-loop priming strategies before implementing them on the hardware, a simple model of the SMA wire was developed in Simulink to test their functionality. This model is greatly simplified compared to other models that appear in the literature due to the fact that only the behaviour of the SMA just prior to actuation and as it undergoes actuation is of interest. The steps taken to develop this model are highlighted in Section 5.2. Four different priming strategies were investigated; two open-loop and two closed-loop. These are detailed in Section 5.3 along with a number of test cases that verified their proper functionality.

In Chapter 6, the experimental results obtained after testing the different priming strategies are presented. The test procedure employed and the different segments implemented in each experimental run are mentioned in Section 6.1. Section 6.2 explains the experimental protocol that was carried out. Two strategies were developed as benchmarks against which the performance of the priming strategies is evaluated in Section 6.3. Section 6.4 talks about the post-priming actuation strategy which was kept common to all experiments. Two metrics were formulated to compare the performance of the different priming strategies, presented in Section 6.5. Section 6.6 presents all the experimental results. The discussion of these results is left for Section 6.7.

The conclusions and future work are discussed in Chapter 7. It highlights the major contributions of this work towards the robust actuation of SMA actuators under varying ambient conditions and the different techniques and methodologies employed to achieve this goal. It also presents a number of suggestions aimed at developing this research further and improvements to the hardware that will help bring it closer to the final product.

Chapter 2

Background & literature review

The literature review for this work is divided into three sections. The first section spans background information on SMAs including its properties, advantages and disadvantages.

In the second section, review and discussion is provided for pertinent closed-loop algorithms that have been implemented by researchers to control SMA actuators, highlighting their relative advantages and disadvantages. The section ends with a comparison between the various control algorithms emphasizing the reasons that inspired the work on resistive feedback in this thesis.

In the third section, the different actuation and priming techniques that have been designed and implemented by various researchers are discussed. Moreover, the similarities and differences between the actuation and priming techniques presented in this thesis and these approaches are highlighted.

2.1 Background information on SMAs

Shape Memory Alloys (SMAs) are metals that exhibit two unique properties: the shape memory effect and pseudo-elasticity. These properties are best described in terms of a solid state phase transformation that occurs in shape memory alloys. The two phases involved in the transformation are known as martensite and austenite.

The martensite phase exists at lower temperatures. In this phase, the molecules are arranged in a twinned structure. As a result, the SMA is relatively soft and can be easily deformed by subjecting it to mechanical stress in which case it becomes arranged in a de-twinned structure. The strain or deformation remains even after

removal of the stress. On the other hand, the austenite phase exists at higher temperatures. The molecules in this phase tend to be arranged in a cubic structure making it relatively rigid and more difficult to deform.

The transformation of one phase into another is characterized by four temperatures: the martensite start temperature (M_s), the martensite finish temperature (M_f), the austenite start temperature (A_s) and the austenite finish temperature (A_f). This can be seen in Figure 2.1. Three factors determine the values of these four variables. The first factor is the amount of load placed on a shape memory alloy: as the load increases, the values of these four temperatures also increase. The second factor is the composition of the wire i.e. the relative amount of each element present in the alloy. Figure 2.2 shows how the percentage of Ni in Nitinol affects M_s [8]. It demonstrates that as the percentage of Ni in the composition increases, M_s decreases to sub-zero temperatures. Finally, training and processing of the material can also affect the transformation temperatures. For example, Flexinol wire, which is manufactured by Dynalloy and used in this study, undergoes a proprietary processing sequence that improves its longevity and repeatability and tailors its properties for repeated electrical actuation.

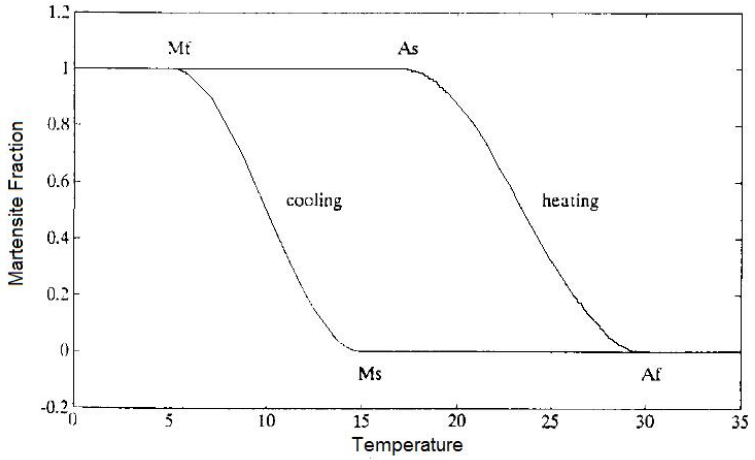

Figure 2.1: Martensite fraction vs temperature [9]

The shape memory effect can be observed when the temperature of the SMA is cycled between $T < M_f$ and $T > A_f$. At temperatures below M_f, the alloy is composed entirely of martensite and therefore can be easily deformed by applying a load to it. By simply heating the alloy, it starts to transform from the detwinned martensitic phase to the cubic austenitic phase. At temperatures above A_f the alloy is entirely austenite and, if the load is removed, the alloy returns to its original shape (see Figure 2.3).

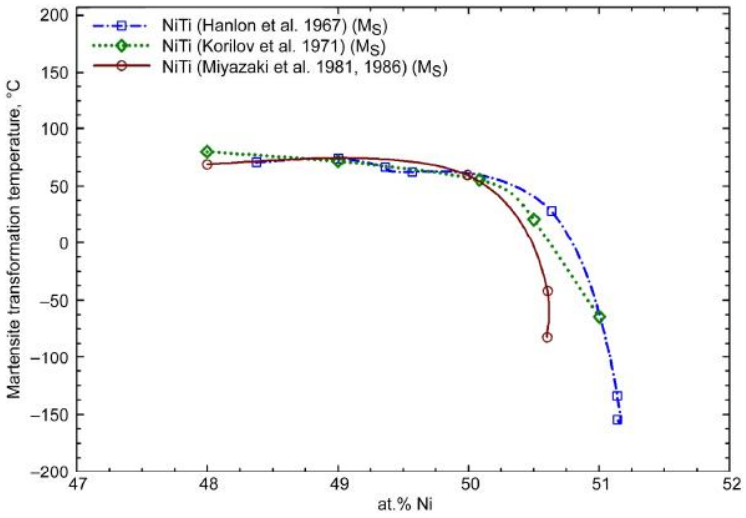

Figure 2.2: Effects of %Ni in Nitinol on M_s [8]

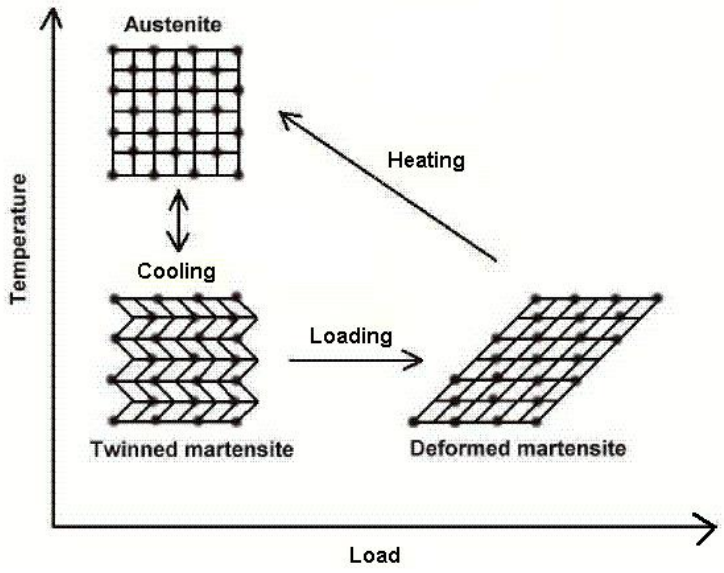

Figure 2.3: Shape Memory Effect of SMA [10]

The shape memory alloy is pseudo-elastic only when it is completely composed of austenite i.e. when $T > A_f$. Unlike the shape memory effect, pseudo-elasticity does not involve a change in temperature. If the load on the alloy is increased, a transformation from the austenite phase to the martensite phase takes place as shown in Figure 2.4. The loading is absorbed by the softer martensite, but as soon as the loading starts to decrease, the alloy transforms back into austenite as its temperature is still above A_f.

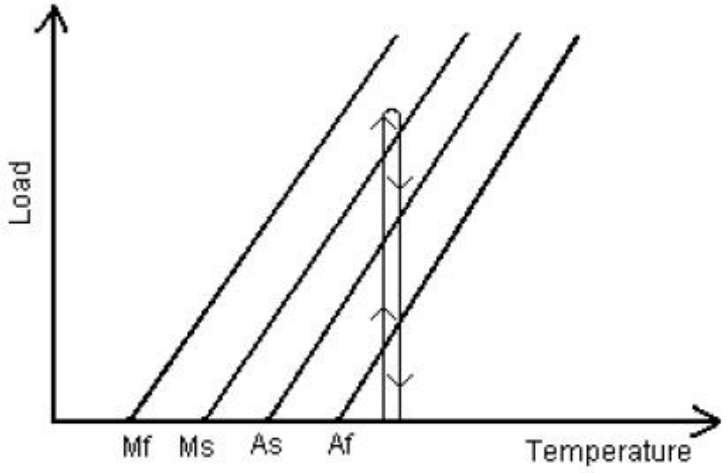

Figure 2.4: Pseudo-elasticity of SMA [10]

Shape memory alloys have several advantageous characteristics that make them particularly attractive in the design of mini- or micro-actuators. Ikuta [5], Choi *et al* [3], Pons *et al* [4] and Song *et al* [2] mention a number of these advantages:

- Simplicity of the actuator mechanism: the principle behind SMA actuation lies in the phase transformation of the alloy. This results in an extremely simple actuator system that can be easily miniaturized. This reduces production costs and enhances reliability [5], [3].
- Cleanliness: this makes it feasible to use in such fields as microelectronics, biotechnology and medical treatment [5].
- Silent actuation: no noise is produced during the phase transformation of SMAs [5], [4].
- Self-sensing capabilities: the change in several material properties of SMA is related to the shape memory effect [5], [4].

- Low driving voltage: actuation of SMA wires requires low voltages. This enables the use of regular power supplies such as 5 V and 12 V [5].
- High recovery stress (> 500 MPa) [2]: this enables SMA actuators to produce large forces [3].
- Tolerance to relatively high strain (up to 6% repeatedly recoverable strain) [2].
- High strength-to-weight ratio making it suitable for miniature actuators [4].

However, shape memory alloys have a number of drawbacks that continue to hamper the usefulness of SMA actuators in a wide range of applications. The first being the hysteresis in the phase transformation of SMA which would require the use of relatively complex controllers to accurately control SMA actuators [4], [11]. During the phase transformation, energy is dissipated due to internal friction and the creation of structural defects [11]. This results in hysteresis in the strain-temperature relationship of a loaded SMA wire actuator as shown in Figure 2.5.

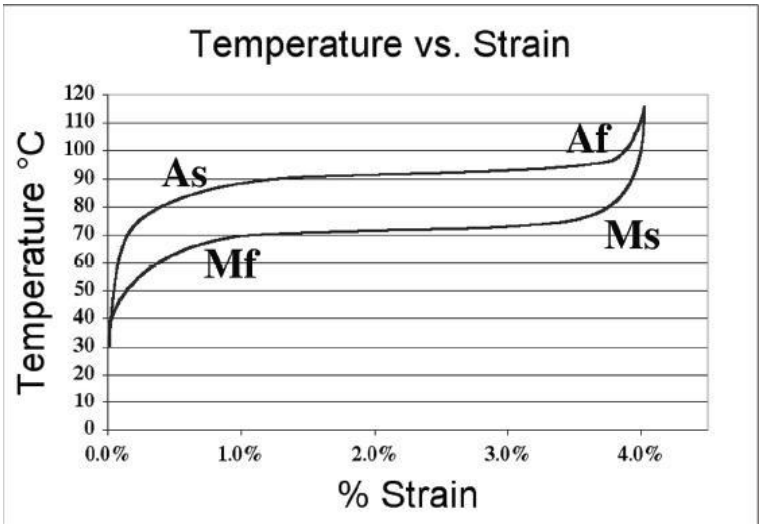

Figure 2.5: Temperature vs Strain hysteresis curve [12]

The second major disadvantage of SMA is its relatively slow cooling response [4]. The time it takes an SMA element to go through an entire actuation cycle (heating and then cooling or vice versa) depends to a large extent on the heat transfer characteristics of the cooling system employed [11]. The bandwidth of SMA actuators is affected by a number of parameters: the temperature and type of the surrounding medium, the type of heat transfer to the surrounding medium and

the surface to volume ratio of the SMA elements [11]. Therefore, depending on the surrounding environment, heat dissipation can pose limitations. If, for example, the surrounding environment has low convection, then the rate of heat transfer to this medium is small resulting in a lower bandwidth. On the other hand, a high convection environment improves heat transfer increasing bandwidth. However, this occurs at the expense of more power needed to achieve the required actuation temperature [11].

Low energy efficiency is another disadvantage of SMA. Given the temperature ranges where typical SMA actuators operate, the efficiency of a Carnot cycle does not exceed 10% [11]. In [13], Thrasher *et al* calculated the "ideal" efficiencies of a fixed-load biased SMA actuator and an SMA biased antagonistic pair to be 3.8% and 2.2% respectively. They indicated that the practical efficiency calculations will be even lower. An additional disadvantage is the small absolute strains achieved by SMA [11]. With 8% strain being the typical maximum one-time recoverable strain for most NiTi-based shape memory alloys, the design of applications creating large motions tends to be more challenging [11]. Another disadvantage is its short fatigue life when subjected to high stresses and heating rates. This would change the properties of SMAs making their functionality inconsistent for the application they were designed for [5]. However, if these extreme conditions are avoided, SMA actuators can be designed to get millions of repeated cycles.

2.2 Feedback control algorithms for SMA actuation

One can think of the control algorithms used for SMA actuation as generally falling under one of two main categories: *open-loop control* - this involves the use of models (such as the Preisach model) [14] for the inverse dynamics of the SMA actuator in an attempt to eliminate or at least reduce the effect of hysteresis, and *closed-loop feedback control* - this typically uses the output error as a feedback signal to produce the corrective input [15], [16]. Although, the former does not require sensors, it has the drawback that many of the parameters needed to develop such a model have to be determined experimentally which increases its practical difficulty. Furthermore, in high-performance applications open-loop feed-forward model-based controllers used for linearization are usually implemented along with closed-loop feedback controllers which help account for modelling error. Therefore, in this literature review, attention is focused on the different closed-loop feedback control

systems that have been implemented in SMA actuation, mainly temperature, force, position and resistance.

2.2.1 Temperature as a feedback control signal

In [17], Kuribayashi proposed a control method that uses the temperature of the SMA wire as a feedback signal to control SMA actuation. A block diagram of the control system used is shown in Figure 2.6.

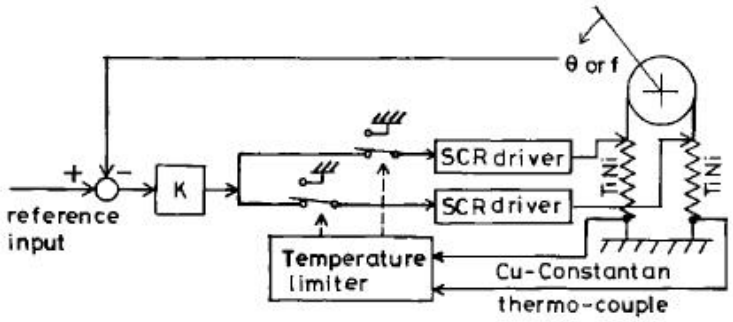

Figure 2.6: Block Diagram of Kuribayashi's Temperature Control System [17]

The system consists of a joint of the Push-Pull type. The two SMA wires making the joint are powered using Silicon Controlled Rectifier (SCR) drivers. The Cu-Constantan thermocouples are attached to the SMA wires to monitor their temperature.

Looking closely at Figure 2.6, one finds that the proposed control method entails two feedback loops: (1) an inner feedback loop where temperature is the feedback signal and, (2) an outer feedback loop that uses the the joint angle θ (position) as the feedback signal. The idea behind this control scheme is to measure the joint angle θ using a potentiometer. The error signal between the desired and measured positions is multiplied by a proportional gain, K, that in turn powers the SCR drivers. If the temperatures of the SMA wires, measured using the Cu-Constantan thermocouples, exceed a certain maximum value, the temperature limiter opens the switches cutting power off from the SCR drivers. Consequently, their output voltages drop down to zero allowing the wires to cool down.

Despite the fact that the temperature control system proposed by Kuribayashi [17] achieved accurate angular displacement control with several reference inputs, Kuribayashi highlights three difficulties he faced in developing the temperature sensor. The first problem lied in the fact that SMA wires have very small diameters

and therefore, a small-sized temperature sensor was needed for this system. It must also have a fast response because the temperature of the SMA wire must be controlled quickly. He overcame this problem by using a 0.1 mm-diameter Cu-Constantan thermocouple which is commonly found in the market. Its very small diameter made it appropriate for use with SMA wires and most importantly, the temperatures it could track matched the range needed in SMA transformation.

The second problem was attaching the temperature sensor to the SMA wire. Typically, temperature sensors are attached to a surface using glue or epoxy. This, however, would be difficult in the case of SMA wires due to the strain it experiences during heating and cooling, increasing the possibility of slippage between the thermocouple and the SMA wire. To solve this problem, Kuribayashi [17] attached the temperature sensor to the SMA wire as shown in Figure 2.7.

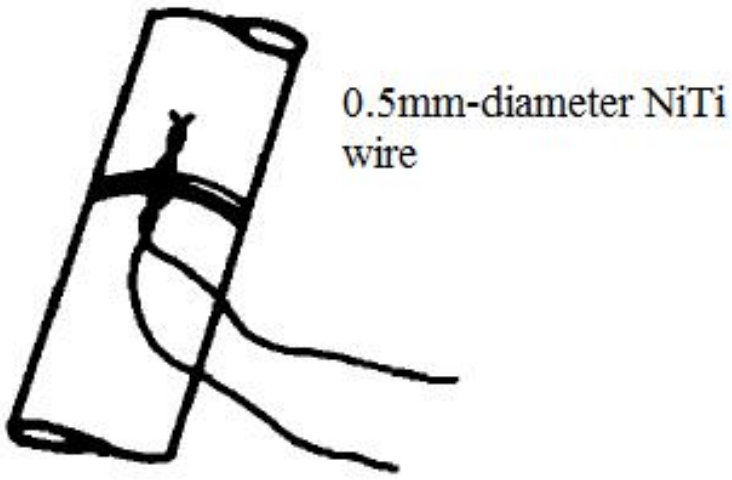

Figure 2.7: Connection between SMA wire and Cu-Constantan thermocouple [17]

According to Kuribayashi [17], this connection had an advantage: it helped avoid bad noise on the signal of the temperature sensor due to the current flowing through the SMA wire.

The last problem that Kuribayashi [17] faced in developing his temperature control system was to electrically isolate the temperature sensors detecting circuit from the driver for the SMA wire. To achieve this, he used transformers in the design of the source of the SMA driver. This helped in ensuring that the source floated from other electric circuits.

In [18], Russell and Gorbet present an SMA actuator whose control depends on temperature sensing. They introduce two new developments to the SMA actuator

design which improves its dynamic performance. The first development involves the use of an infrared temperature sensor. This is to allow the rapid heating of the SMA wire without running the danger of overheating it. The second development entails the use of a mobile heat sink to improve the cooling response of the SMA wire.

Russell and Gorbet [18] state two key reasons for choosing temperature as the feedback signal for their control scheme. The first reason is that, for short periods of time, the effects of heat dissipation can be largely ignored. Under this condition, the time taken by the SMA wire to actuate (i.e. contract) decreases as larger currents are used to heat it. However, manufacturers of SMAs warn against applying large currents for long periods of time as it may damage the wire and cause it to lose its properties. To avoid using the *safe current* [1] given by manufacturers and employed by some researchers in their work, Russell and Gorbet [18] state that if the wire temperature can be measured, then higher currents can be used to actuate the wire faster without overheating it. The second reason that Russell and Gorbet [18] give for using temperature as the feedback signal is to prevent excessive heating of the SMA wire that would slow down the wire's cooling response.

To avoid facing the same problems that Kuribayashi [17] had in using a thermocouple to measure the temperature of the SMA wire, Russell and Gorbet [18] opt for the use of a non-contact temperature sensor. The only drawback to such sensors is that they only respond to changes in infrared radiation and not its absolute value. This resulted in Russell and Gorbet [18] going to great length in developing and calibrating an infrared temperature sensor consisting of a pyroelectric sensor, a spring steel, a magnet and an electromagnet.

Indeed, the actuator design developed by Russell and Gorbet [18] was able to accurately track a square wave input. Moreover, compared to an experimental trial where the current flowing through the SMA wire was limited to only 1.8 A, measuring the temperature of the SMA wire helped increase the current safely to 2.4 A bringing about a reduction in contraction time.

Since the focus of the research in this thesis is to develop SMA actuators for automotive applications, the use of temperature as a feedback signal will not be the best choice for a number of reasons. In [17], Kuribayashi does overcome the difficulties associated with designing a temperature sensor only to do so at the expense of the system's size. Having used six transformers to isolate the detecting circuit of the temperature sensor from the driver of the SMA actuator makes it less

[1] The safe current can be supplied to an SMA wire indefinitely without damaging it

practical for use in micro-/miniature- applications such as automotive applications. The same applies to the infrared temperature sensor developed by Russell and Gorbet in [18].

A second reason for not using the temperature as a feedback signal relates to system cost. In [17], the use of a thermocouple and isolation transformers and the use of a non-contact infrared sensor in [18], increase the overall system cost. This is often unacceptable in automotive applications where optimizing system cost is considered a high priority.

The use of sensors and other hardware components has repercussions on yet another important aspect of system design: power consumption. In [17] and [18], the use of temperature sensors and the transformers would increase power consumption. In fact, this is supported by Kuribayashi's experimental results [17]: he found that his proposed control system needed 4.5 times the voltage needed by the PWM control scheme proposed by himself in [19] to effectively control the SMA actuator. Assuming that the currents used to heat the SMA wire in [17] and [19] were the same (nothing is mentioned about the current in either reference), then consequently, the control scheme proposed in [17] would consume 4.5 times the power used in [19]. This is a very important point to consider in automotive applications where power consumption should be kept to a minimum.

2.2.2 Force as a feedback control signal

In [20], Grant and Hayward presented experimental results indicating that SMA actuators can be used to control forces rapidly and precisely. This is due to the fact that SMAs have a high strength-to-weight ratio and makes them well-suited for force control applications that do not entail a lot of motion. One example which they were investigating was a robot gripper.

The experimental setup used in [20] consisted of two antagonistic SMA actuators. The setup also consisted of a force sensor and an ultra-precision mini load-cell connected to the SMA actuators through a rigid beam. Grant and Hayward [20] also included relay controllers in the design of their control system citing the following advantages of their use:

- They are robust to uncertainties in the different parameters.
- They are easy to implement both physically and computationally.

- They circumvent the hysteresis behaviour of SMA.

The two-stage multi-relay controller used operates as follows: depending on the magnitude of the error signal, one of two current values is used to drive the SMA actuator. When the error is large, the higher value current is used to drive the system quickly to the desired value. This current was referred to as I_H. As the error decreases and approaches zero, the smaller value current, denoted by I_L, is used to minimize the limit cycle magnitude. A block diagram of the complete control system is shown in Figure 2.8.

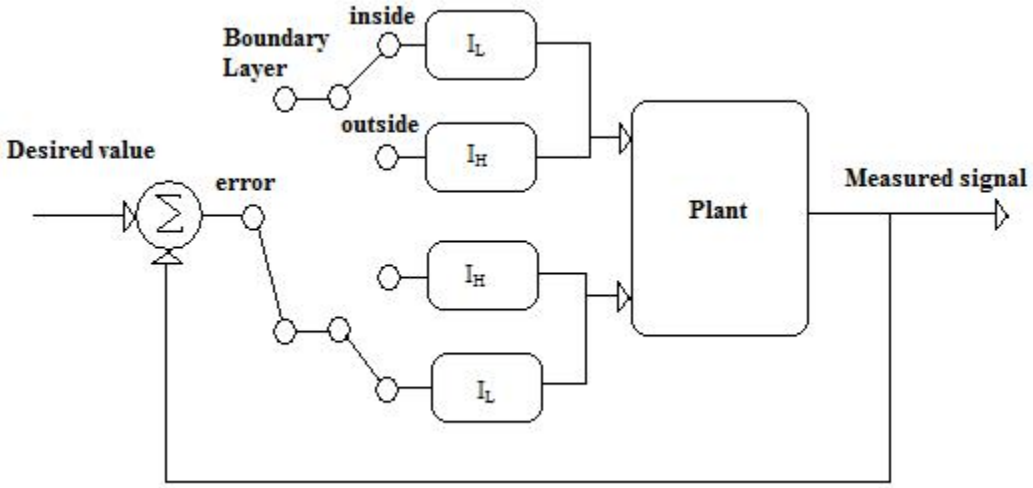

Figure 2.8: Control system developed by Grant and Hayward [20]

To examine the closed-loop step response and the tracking response of their control system, Grant and Hayward [20] conducted several simulations and physical experiments using a series of desired force steps as well as sine waves of varying amplitude and frequency. Indeed, the controller design proposed by Grant and Hayward in [20] succeeded in rapidly changing the desired force value through the range of forces. Moreover, the controller design resulted in a smoother motion that ensured both stability of the system and a quicker response.

In [21], Choi *et al* use force as the feedback signal in controlling the SMA actuators used in a small-sized flexible gripper (shown in Figure 2.9). They demonstrate the use of a two degree-of-freedom H_∞-controller to achieve robust stability and improved force tracking performance. The experimental setup used by Choi *et al* [21] is shown in Figure 2.10.

The flexible gripper is set up inside a thermal insulating chamber where the temperature is maintained at $12 \pm 1\,^{\circ}\mathrm{C}$. The force exerted by the gripper is measured

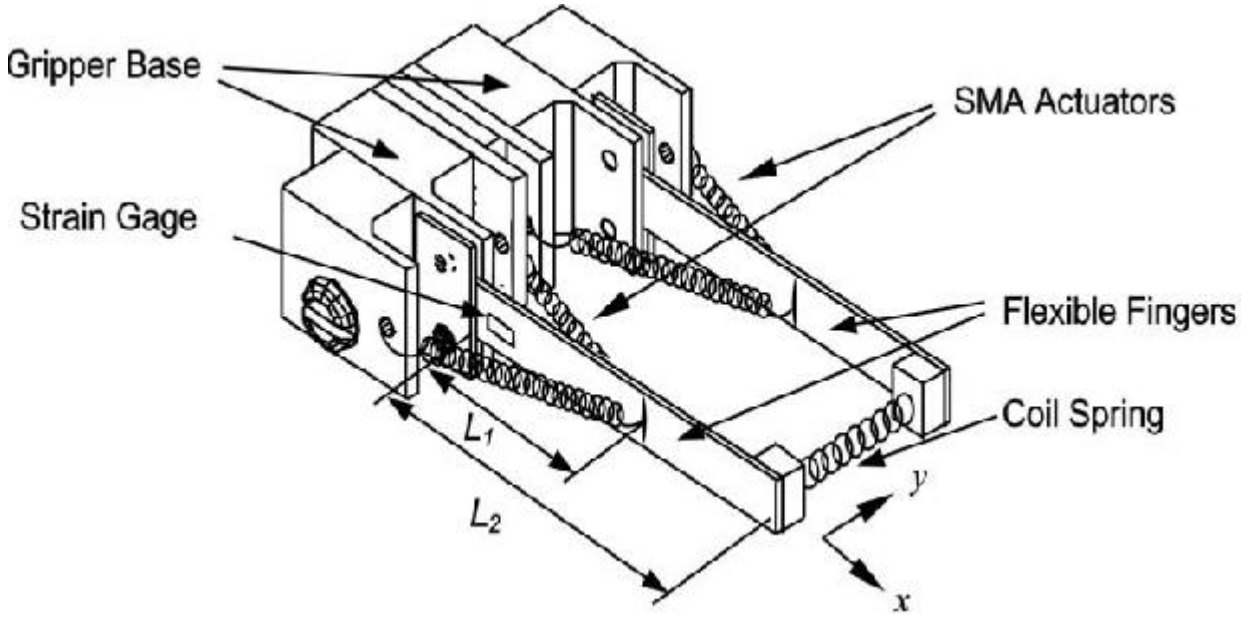

Figure 2.9: Flexible gripper proposed by Choi *et al* [21]

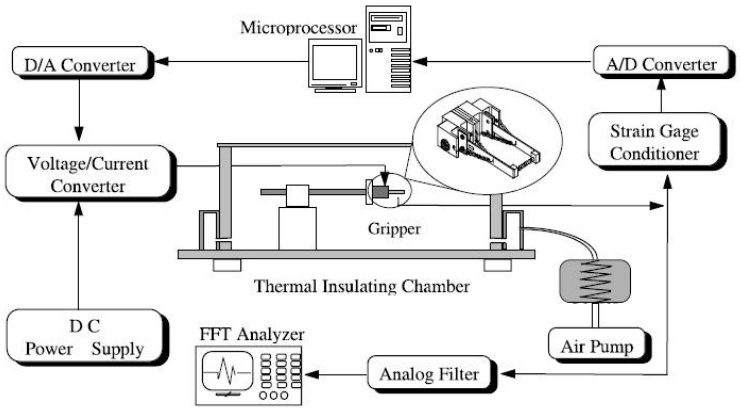

Figure 2.10: Experimental setup proposed by Choi *et al* [21]

by a strain gauge whose output (a voltage signal) is calibrated to yield a gripping force. The strain gage conditioner amplifies the measured force before being fed back into the microprocessor through an analog-to-digital converter. The H_∞-controller calculates the control input current supplied to the SMA actuators via the digital-to analog converter and the voltage/current converter. The sampling frequency was chosen to be 1 kHz.

To test the effectiveness of their proposed controller design, Choi *et al* [21] conducted several experiments with varying step and sinusoidal force trajectories to investigate the force tracking control responses. They set out two goals to achieve:

- That robust stability of the gripper is maintained in the presence of $\pm 40\%$ variation of time constant (they define the time constant as the average of the heating and cooling time constants [2] of the SMA wire).
- That the tracking error should be less than 2% in steady state.

Indeed, Choi *et al* [21] succeeded in achieving these goals using their flexible gripper system under varying force trajectories. Moreover, they found that the simulation and experimental results matched very closely indicating the validity of the dynamic model they proposed as well as their control logic. One thing they noted was that tracking performance deteriorated as the trajectory frequency increased. They attributed this, not only to the dynamic characteristic of the SMA actuator, but also to the system parameters and the hardware and software components used in the experimental setup.

Just as in temperature sensing, the use of force in the control of SMA actuators requires a sensor. Again, this would increase system cost, system size and power consumption, three very important factors that must be optimized in automotive applications.

2.2.3 Position as a feedback control signal

Another feedback signal that has been widely used by researchers is position. One example is the work by Song *et al* [2]. In [2], Song *et al* designed an experiment to actively control the tip position of a composite beam. They accomplished this by embedding SMA wires into its face sheet. An infrared laser sensor was used to measure the deviation of the beam tip from its desired position. To correct this

[2] Choi *et al* [21] define the *time constant* as the time to reach 63.2% of the steady state value

error, a calculated current was driven through the SMA wires actuating it, thus returning the tip to its desired position. The elasticity of the beam provided the restoring force.

The control system they proposed, given as $i = i_f - K_D r - \rho tanh(ar)$ [2] and shown in Figure 2.11, consisted of three main parts: a PD control (- $K_D r$) , a feed forward current (i_f) and a robust compensator (- $\rho tanh(ar)$). The proportional part in the PD control was used to decrease the steady-state error in the position of the beam tip, while the derivative part was used to increase damping to stabilize the actuator. The purpose of the feed forward current was to pre-heat the SMA actuators and compensate for environmental heat losses. As for the robust compensator, it was used to compensate for the hysteresis inherent in SMA actuators to help increase control accuracy and stability.

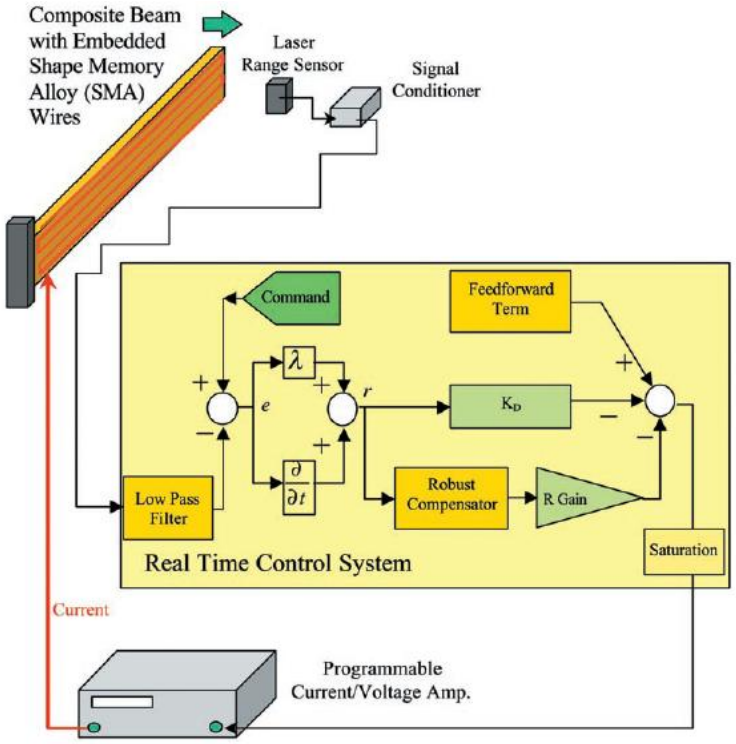

Figure 2.11: Block diagram of control system proposed by Song *et al* [2]

Experimental results, shown in Figure 2.12, verified that the proposed control system was able to accurately and rapidly control the position of the beam tip. No overshoot was observed and according to Song *et al* [2] the transient response was satisfactory. Moreover, the results showed that the proposed controller's response was 3 times faster compared to an earlier controller that did not incorporate a robust compensator: with a robust compensator, it only took 25 s for the tip to

reach 7 mm deflection from a 4 mm deflection, whereas it took triple that time to move the same distance in the case without a robust compensator.

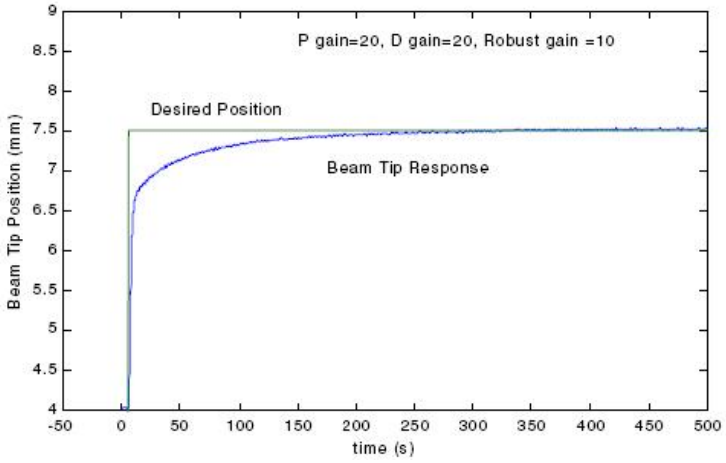

Figure 2.12: Results of tip position control using a robust compensator [2]

With these results, Song *et al* [2] concluded that their proposed control design successfully controlled the tip position of the composite beam.

In [22], Ahn and Nguyen presented a self-tuning fuzzy [3] PID [4] controller for SMA position control. They stated that the effectiveness of this system stems from its ability to compensate for unknown parameters such as the surrounding environment as well as the hysteresis inherent in SMA actuators. The experimental setup used by Ahn and Nguyen [22] is shown in Figure 2.13. A high precision potentiometer was used to measure displacement.

To investigate the effectiveness of their proposed controller design, Ahn and Nguyen [22] experimented with different reference inputs (step and sine of different frequencies) and compared the obtained results with those obtained from implementing a conventional PID controller. According to Ahn and Nguyen [22], their proposed controller design was indeed able to adaptively achieve good tracking response to varying references and performed better than a conventional PID controller.

Again, just as with temperature and force feedback, the use of position as a feedback signal requires the use of sensors as observed in [2] and [22]. Consequently,

[3]Fuzzy logic, a form of multi-valued logic, was developed by Dr. Lotfi Zadeh in 1965. Contrary to crisp set theory, where an element either belongs to a set or not, an element of a fuzzy set may partially belong to a given set and therefore its degree of membership may vary over the range [0,1].

[4]PID: proportional-integral-derivative control

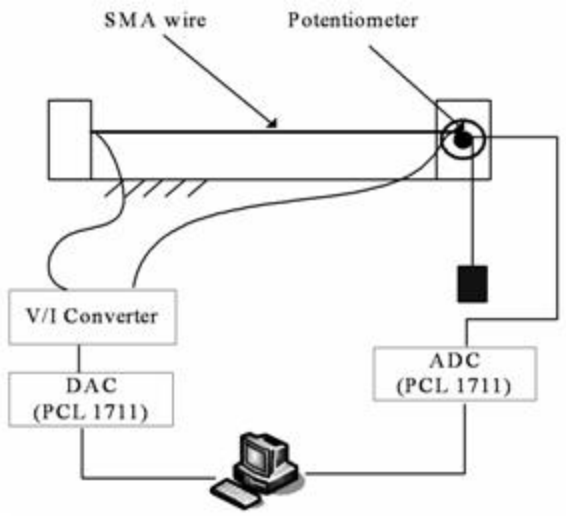

Figure 2.13: Experimental Apparatus used by Ahn and Nguyen [22]

this increases system size and cost which is undesirable in automotive applications.

2.2.4 Electrical resistance as a feedback control signal

The use of the electrical resistance of SMA wires as a feedback signal in the closed loop control of SMA actuators was investigated by Allston *et al* [23] and Ma *et al* [15]. In [23], Allston *et al* present the design of a shape memory alloy fuel injector that uses electrical resistance feedback to open or close the fuel injector. To commence fuel injection the valve is opened quickly by applying a large enough voltage. This supplies enough power to the SMA element causing it to transform quickly to its contracted austenite state. To close the injector, no voltage is applied across the SMA element causing it to transform to its martensite state. This is made possible by making use of the fact that the resistivity of the SMA is different in its martensite and austenite states. Thus, the electrical resistivity of the SMA element is monitored and used to indicate when the phase transformation is complete.

Allston *et al* [23] state a number of advantages for the proposed controller design, two of which can be attributed to the use of electrical resistance feedback. First, monitoring the resistance of the SMA wire will indicate when the SMA element has transformed into austenite. Consequently, the supplied power can be reduced to a lower value preventing the SMA element from overheating. Secondly, the use of electrical resistance feedback will not require any external sensors.

In [15], Ma *et al* indicate that their proposed control scheme achieves stable and

accurate position control eliminating the need for a position sensor. The relationship between electrical resistance and displacement of SMA actuators is investigated through several experiments. To compensate for the hysteresis inherent in SMA wires, Ma *et al* [15] resort to the use of a neural network which upon training, is used to model this relationship and to predict the position of the SMA actuator using only electrical resistance. The proposed control scheme also incorporates a PD controller.

Ma *et al* [15] support their choice of using the electrical resistance of SMA actuators as a feedback signal by stating that the relationship between varying electrical resistance and strain of an SMA actuator during phase transformation, despite being nonlinear, is deterministic and repeatable. They go on to explain that, under certain stress conditions, the strain was only a function of the fraction of the alloy that is in the martensite phase. Since the variation in electrical resistance is determined by this fraction and the strain, electrical resistance can be used to predict the strain in SMA actuators.

Ma *et al* [15] conduct a number of open-loop experiments to investigate the relationship between the displacement and electrical resistance of a Nickel Titanium (NiTi) wire under varying activation conditions such as different pre-tensions, different stresses and different magnitudes of the input voltage. From these experiments, Ma *et al* [15] obtain several loops relating displacement and electrical resistance under the different activation conditions. These loops are similar to the major loops used to model SMA hysteresis in the Preisach model [14]. Ma *et al* [15] model the hysteresis between electrical resistance and displacement using one of the major loops produced by the open-loop experiments. The major loop used is shown in Figure 2.14.

The relationship between the electrical resistance and the displacement for the representative loop in Figure 2.14 is modelled by a three-layer neural network that takes two inputs: the electrical resistance of the SMA actuator and a tag signal. Due to the hysteresis inherent in SMA wires, the electrical resistance value can correspond to more than one displacement value. Therefore, the representative loop is divided into 3 segments (AB, BC and CD) as shown in Figure 2.14. These divisions are made based on the slope of the loop. The tag signal indicates a specific segment of the representative loop and thus, a corresponding single value for the displacement. Data from the representative loop, obtained from the open-loop experiments, is used in training the neural network. The electrical resistance of the SMA actuator is obtained by dividing the value of the applied voltage by the current flowing through the SMA actuator. The model of the electrical resistance-strain

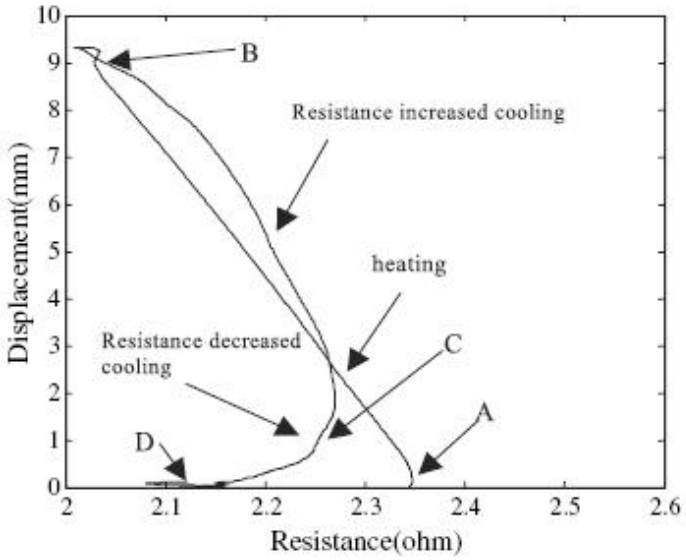

Figure 2.14: Major loop representing the electrical resistance hysteresis [15]

relationship outputs a certain displacement. The error between this value and the measured displacement is then fed into the Back Propagation algorithm [5] which infers the strain of the SMA wire by adjusting the weights of the model. This is done iteratively until the produced output closely resembles the actual output. The error in the prediction made by the neural network is then fed into a PD controller which in turn, produces a control signal that gets amplified by a programmable power amplifier before being applied to the SMA wire.

To verify the accuracy of the proposed control system, Ma *et al* [15] conduct several experiments using a multi-step position signal. An important finding is that control accuracy is much higher during the heating process than during cooling. The results also reveal that there was an average position error of about 7% in steady state. Although they declare that this error was much larger than in the case of feedback control using a position sensor, they state that their choice of the representative loop used to model the hysteresis between displacement and electrical resistance could be the source of that error. Nevertheless, they claim that the performance is still considered reasonable for many applications. In fact, they advocate that the major advantage in their proposed control system is that, apart from using the LVDT sensor to verify their results, no sensor is needed.

The findings of [15] and [23] are very important for this research as they prove

[5] A supervised learning method used to teach neural networks how to perform a given task by propagating error backwards from the output nodes to the input nodes.

that an SMA wire can be accurately controlled using electrical resistance feedback. What is of particular importance is that this can be achieved without the need for special external sensors thus reducing the system's size and cost, two very important aspects of automotive applications. In fact, the current used in computing the resistance of the SMA wire can be sensed using a simple resistor. This has a further advantage: this resistor can be easily incorporated on the circuit board used to control the actuator which can be placed at some distance from the actual wire. However, the other sensors (temperature, position and force) require that they be placed at the SMA wire itself or at very close proximity. Finally, the results of [15] and [23] show that electrical resistance feedback can be intelligently used to control SMA actuation.

2.2.5 Advantages of electrical resistance feedback vs other feedback systems

One metric by which the various proposed control systems can be compared is via the system size. The designs of the first three control systems discussed all incorporate the use of sensors, whether to measure temperature, displacement or force. Of course, this does result in a more complex system. In [17], not only did Kuribayashi use a temperature sensor, but he also mentioned three difficulties in designing it. Although he overcame these difficulties, he did so at the expense of the system's size. Having used six transformers to isolate the detecting circuit of the temperature sensor from the driver of the SMA actuator makes it less practical for use in micro-/miniature- applications. The same applies to the infrared temperature sensor developed by Russell and Gorbet in [18]. In the control system proposed by Grant and Hayward [20] the use of relay controllers further increased the size of the system. In [2], [15]and [23], an LVDT sensor was used. In this case, using the electrical resistance of the SMA wire as a feedback control signal has a comparative advantage over the other signals: with electrical resistance used as feedback, no special external sensor is needed as the current used in computing the resistance of the SMA wire can be sensed using a simple resistor. Moreover, this resistor can be placed at some distance from the SMA actuator while the other sensors have to be placed at the wire itself or very close to it.

Another important aspect to consider is system cost. The temperature sensor and the isolation transformers that Kuribayashi used in his design increase the overall cost of the control system. The same applies to the ultra-precision mini load cell from Transducer Techniques (MDB-2.5) which Grant and Hayward [20]

used for their system, not to mention the additional cost incurred due to the relay controllers. The same applies to the NAIS laser analog sensor that Song *et al* [2] used in their design. However, the control system proposed by Ma *et al* [15] does not entail the use of any special sensors or additional hardware thus keeping system cost low.

The use of sensors and other hardware components have repercussions on yet another important aspect of system design: power consumption. In [17], the use of the temperature sensor and the transformers would increase power consumption. In fact, this is supported by Kuribayashi's experimental results [17]: he found that his proposed control system needed 4.5 times the voltage needed by the PWM control scheme employed in [19] to effectively control the SMA actuator. This is also bound to be the case with the control systems developed by Grant and Hayward in [20] and Song *et al* in [2] with the use of sensors and other hardware components such as relay controllers. Given the fact that the control system proposed in [15] does not include any additional hardware components, one can infer that it would have the lowest power consumption among all the designs.

2.3 Priming & actuation techniques in the literature

Priming can be defined as the process of bringing an SMA element close a transition point in preparation for actuation, and then maintaining it at that point. Actuation on the other hand, refers to transforming the wire from one state to another (martensite to austenite or vice versa). The majority of the actuator designs are based on actuating the wire upon heating, which will be the focus of this thesis. Looking into the literature, a lot of researchers have designed and implemented various priming and actuation techniques in their work. In fact, the references reviewed in this section are divided into two major categories: actuation techniques aimed at reducing the latency associated with transforming from one state to another (i.e. martensite to austenite or vice versa), and priming techniques whose goal is to reduce what one may refer to as the *pre-move time* which is the time required for the SMA wire to reach an intermediate state between A_f and M_f prior to a change of state.

2.3.1 SMA actuation techniques

One of the major disadvantages of SMA, which has hindered its use in a wide range of applications, is its slow cooling response [4]. The time it takes an SMA element to go through an entire actuation cycle (heating and then cooling or vice versa) is limited to a large extent on the heat transfer characteristics of the cooling method employed [24]. The bandwidth of SMA actuators is affected by a number of parameters: the temperature and type of the surrounding medium, the convection of the surrounding medium and the surface to volume ratio of the SMA elements [24]. Therefore, depending on the surrounding environment, heat dissipation might pose a problem. If, for example, the surrounding environment has low convection, then the rate of heat transfer to this medium is small resulting in a lower bandwidth. A high convection environment improves heat transfer increasing bandwidth. However, this occurs at the expense of increased power needs to achieve the required actuation temperature [24].

Numerous researchers have studied techniques to help improve the cooling response time of SMAs. Russell and Gorbet [18] introduced two new developments to SMA actuators which helped improve its dynamic performance. The first development was the use of a non-contact infrared temperature sensor for temperature control. The second development consisted of the design of a mobile heat sink. According to Russell and Gorbet [18], several static cooling methods such as water immersion, heat sinking and forced air cooling have been implemented and tested in previous work. Indeed, these methods have helped improve the cooling response of SMA wires but at the same time suffered from the major drawback of increased power consumption due to heat lost to the cooling medium. Thus, they proposed the idea of a mobile heat sink with the goal of achieving the same improved performance as with static heat sinks, but without an increase in power consumption.

As for the non-contact infrared temperature sensor, it played an important role in improving the cooling response of the SMA actuator by preventing excessive heating which does not produce any additional strain but rather adds to the cooling problems. For example, if the required strain is achieved when the wire temperature is 70 °C, the non-contact infrared temperature sensor would maintain the wire at this temperature and prevent it from increasing to, say, 80 °C. If the wire then needs to be cooled down to 20 °C, then it would take less time to cool it down from 70 °C than from 80 °C. However, the improved cooling response was not the only advantage of monitoring the SMA wire's temperature using the non-contact infrared temperature sensor proposed by Russell and Gorbet [18]. In fact, it also

helped in speeding up the heating response. Traditionally, researchers specified a maximum *safe current* that the SMA wire can withstand for long periods of time without overheating. However, Russell and Gorbet [18] indicated that measuring the wire temperature using the infrared sensor enabled heating the wire using higher transient currents and thus achieving faster contraction. For the work presented in this research, only the contraction upon heating is of interest since the target applications are not cyclic.

Also of interest is the work presented by Featherstone and Yee [6] where they describe a method for improving the speed of the heating response by increasing the rate at which an SMA element can safely be heated. Whereas SMA manufacturers state in their data sheets a safe value for the heating current which can be used to heat the SMA wire indefinitely without damaging it, Featherstone and Yee [6] found that a better strategy would be to monitor the state of the SMA wire by measuring its electrical resistance, and then use that value to compute a maximum safe heating current suitable for the SMAs current state. For example, if the SMA wire is cool, then the time required to actuate it can be significantly reduced by applying a large heating current, larger in magnitude than the manufacturer-specified safe current, as long as the SMA remains below a certain threshold temperature.

However, due to the hysteretic behaviour inherent in SMA wires which complicates the relationship between temperature and resistance, Featherstone and Yee [6] identified 5 different quantities which they used to implement their proposed strategy shown in Figure 2.15. They started off by identifying a threshold resistance, R_{thresh}, that marks the boundary between what they refer to as safe resistances and possibly unsafe resistances when the SMA wire is at risk of overheating. They defined this threshold value as the resistance of the hot SMA element. They added to it a safety margin that accounts for errors in resistance measurements, strain-induced resistance changes and possible variations in this value from one SMA element to another. Featherstone and Yee [6] then used this value to define a maximum safe heating current I_{max} which is a function of the SMAs measured resistance. They also defined a current I_{safe} that can be safely applied to an element indefinitely without risk of overheating, and at the same time maintain the temperature of the SMA wire above A_f. Of course, the obvious value for I_{safe} would be the values of safe currents found in the SMA wire data sheets [6]. As for the maximum heating current aimed at speeding up the heating response Featherstone and Yee [6] defined a current I_{high} whose value is typically determined by the limits on the power supply. Finally, they defined an optional additional resistance threshold, R_{ramp}, that is larger than R_{thresh} with the purpose of allowing a smooth transition

between I_{safe} and I_{high}.

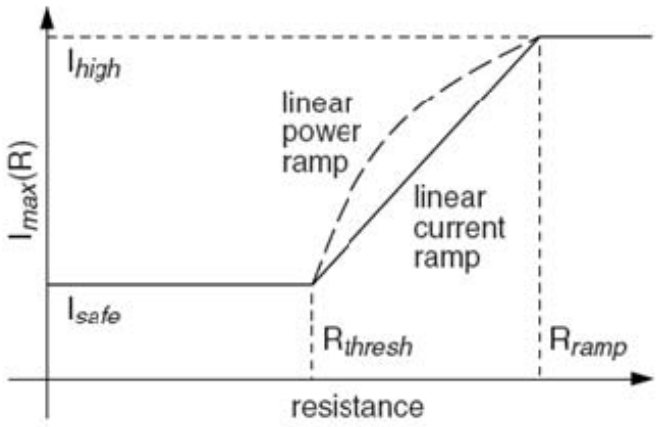

Figure 2.15: The 5 different quantities identified by Featherstone and Yee [6] to implement their improved heating strategy

Incorporating the improved heating method proposed in [6] is depicted in Figure 2.16.

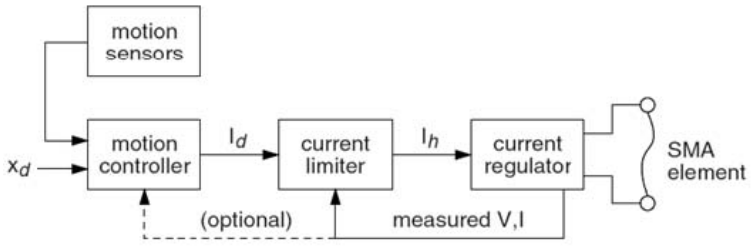

Figure 2.16: Motion control system implementing proposed heating strategy [6]

The desired position signal, x_d, and input signals from motion sensors are input into a motion controller which in turn, calculates an output signal I_d representing the desired heating current for the SMA element. The current limiter then uses this signal to compute the actual heating current that will be applied to the SMA element according to the following formula [6]:

$$I_h = min[I_d, I_{max}(R_{measured})]$$

The current regulator serves two purposes as it applies the current I_h to the SMA wire and also feeds back the measured voltage across the SMA element and the current flowing through it to the current limiter where the resistance of the SMA element gets calculated.

Featherstone and Yee [6] incorporated this method into a two-stage relay controller controlling the motion of a pantograph robot actuated by two antagonistic pairs [6] of SMA wires. Indeed, experimental results showed that the proposed heating strategy doubled the maximum speed of the actuators compared to the traditional heating regime where the safe current depicted in the SMA data sheets was applied while employing the same cooling technique [6].

The idea presented in [6] of monitoring the state of the SMA wire through its resistance and using it to determine certain controller strategy parameters, is also employed in the work presented here. As will be seen later, monitoring the wire's resistance during an experiment aids in the determination of other important parameters such as the priming current, the actuation current and the maintenance current which will be defined in Section 2.3.3.

In [23], Allston *et al* presented the design of a shape memory alloy fuel injector whereby they improve both the heating and cooling responses of the SMA. To commence fuel injection the valve is opened quickly by applying a large enough voltage that heats the SMA element transforming it quickly into its contracted austenite state. Again, using the fact that the resistivity of the SMA is different in its martensite and austenite states, the electrical resistivity of the SMA element is monitored and used to indicate when the phase transformation is complete. Consequently, a lower hold voltage is applied to prevent the SMA from overheating. If the electrical resistance measurement indicates that the SMA element is beginning to cool down and is transforming back to the martensite state, the high voltage is re-applied and a new control cycle begins. To close the injector, the voltage across the SMA element is set to zero. In order to reduce its cooling response, the design included a metering orifice plate which directs fuel across the SMA (forced convection) and helps maximize the area of contact between the SMA and the fuel.

There is an important criticism to the work presented by Allston *et al* [23]. They talk about applying a "large enough voltage" that will actuate the SMA wire regardless of the ambient conditions. However, the results of the work presented in this research will indicate that the amount of power needed to actuate an SMA wire varies with ambient conditions. In some cases (e.g. very low ambient temperatures) this *maximum power* may not be sufficient to actuate the SMA wire and in other cases (e.g. high ambient temperatures) may be too high which may result in the SMA wire overheating.

[6] An actuator configuration consisting of two wires connected to one another; when one SMA wire is heated, the other is cooled.

Loh *et al* [25] implemented a very similar idea to the one in Allston *et al* [23] to control a robotic finger. They did so by combining two different methodologies. For the first method, aimed at improving the cooling response of the SMA, they implemented a simple, light-weight heat sink which consisted of an outer metal tube concentric with the SMA wire and silicon grease occupying the volume in between the metal tube and the SMA wire. The second method, aimed at speeding up the heating response, involved actuating the alloy using high current pulses in the order of milliseconds. These methodologies came about to counter what Loh *et al* [25] state as the two causes for the slowness of the actuation speed of the SMA actuator: (1) the slowness of the of heat dissipation from the alloy to the environment and, (2) inappropriate heating of the SMA wire.

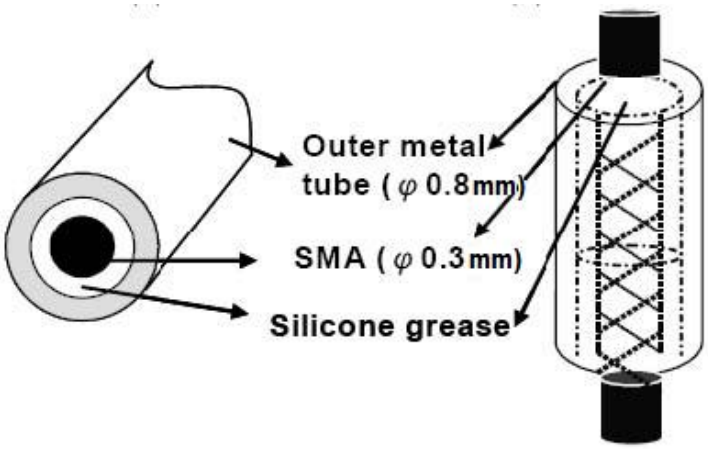

Figure 2.17: Heat sink proposed by Loh *et al*

The outer metal tube and the silicone grease have a thermal conductivity of 315 and 2.0 respectively [25]. This is much larger than the thermal conductivity of air (0.0386) and therefore, heat is conducted faster to the surrounding environment. Compared to natural cooling, simulation results showed that the proposed heat-sink mechanism (outer metal tube with silicon grease) reduced the temperature of the SMA wire (measured using a thermocouple) by an additional 7 °C in 4 s [25]. Moreover, Loh *et al* [25] conducted experiments whereby an SMA actuator was used to lift a 3 kg mass periodically. The experiments were conducted at a temperature of 27-28 °C with minimum wind conditions and an asymmetric square wave was applied to the SMA wire to lift the 3kg mass periodically. An SMA wire manufactured by Nilaco with a diameter of 0.3 mm and a length of 60 cm was used in the experiments. Two sets of experiments were conducted: one with the proposed heat sink and one without it. Experimental results, shown here in

Figure 2.18, showed that, with the heat sink present, the position of the mass oscillated consistently within 7.5 mm even after 25 s of actuation compared to an oscillation of only 3 mm of the mass position achieved by natural cooling [25]. The results also showed that, with the use of the proposed heat sink, the mass did not rise as fast as its counterpart but when the input voltage was cutoff, the SMA wire extended at a faster rate compared to when no heat sink was used [25]. The fact that the mass did not rise as fast when a heat sink was used can be explained by heat being dissipated even when the SMA wire was being heated.

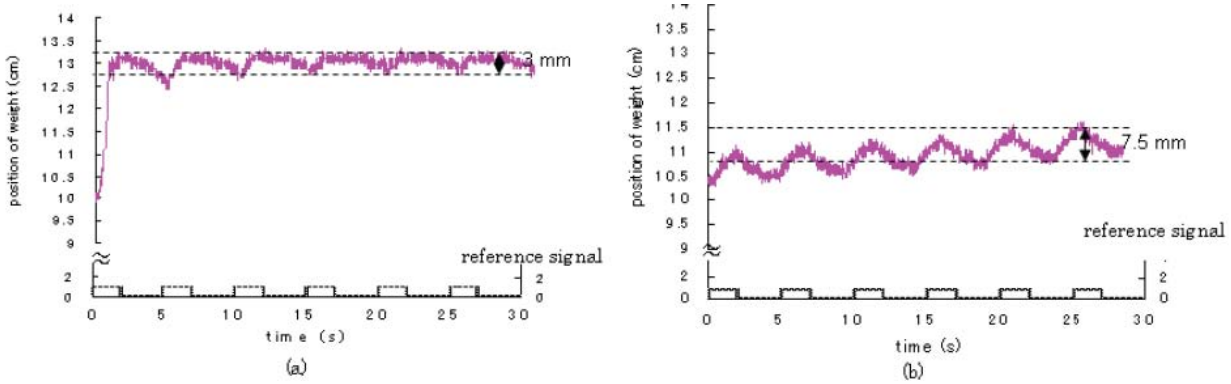

Figure 2.18: Position control of SMA actuator (a) without heat sink (b) with heat sink [25]

As for the actuation method proposed by Loh *et al* [25] which consisted of heating the SMA wire using high currents in the form of short pulses, the authors hypothesized that the electrical energy supplied to the SMA wire gets transformed into kinetic energy, due to the phase transformation in the SMA, and heat energy [25]. The authors put forth two hypotheses for describing this characteristic of the SMA [25]:

1. The increase in temperature is reduced when the SMA is actuated.
2. Rate of heat transfer decreases as the actuation speed of the SMA increases.

Again, a number of experiments were conducted to compare the increase in temperature and the rate of increase in temperature for a strained SMA wire versus a non-strained SMA. The only difference between both sets of experiments was that for non-strained SMA, the 3 kg mass was substituted with a 1 g mass which was light enough so as to not strain the SMA. The experimental results showed that the strained SMA experienced a lower increase in temperature and a lower rate of increase in temperature when actuated when compared to the non-strained SMA

[25]. This was the case for three different power inputs: 7.5 W for 5 s, 12.5 W for 5 s and 26.25 W for 2 s. According to Loh *et al* [25], these results support their two hypotheses.

To compare the effectiveness of this actuation method with the traditional gradual heating method Loh *et al* [25] conducted more experiments where, for gradual actuation, a periodic current of 0.75 A with an ON time equal to 3 s and an OFF time equal to 3 s was applied to the SMA wire to achieve a contraction of 12.5 mm. On the other hand, the proposed actuation method was tested by applying a periodic current of 3 A with ON time equal to 30 ms and OFF time equal to 3 s achieving the same contraction of 12.5 mm. It was found that in gradual heating, each actuation cycle dissipated 23.6 J to the SMA whereas for the proposed method, 3.8 J were consumed for each actuation cycle. Using all these results, Loh *et al* [25] concluded that the advantages of their proposed actuation method were two-fold: it achieves fast actuation of the SMA by applying a high current, and also a faster cooling response when the input is switched off because the high current was only applied for short ON pulses.

The work presented in [25] differs from the work presented in this thesis in that the results obtained in [25] were achieved at a constant temperature. However, the ultimate goal in this thesis is to actuate the SMA wire in a consistent period of time **regardless** of the ambient conditions. On the other hand, the idea of actuating the wire quickly using high current pulses as in [25] is used in this thesis. In this research, a PWM signal of varying duty cycle is used to control an SMA wire; the duty cycle is increased or decreased to heat or cool the SMA wire respectively. For example, when the *Safe Duty* priming strategy (explained in Section 6.3.1) was run at room temperature, a 26 cm-long wire was actuated by a periodic current of approximately 2.1 A with an ON time of 3.2 ms and a period equal to 20 ms.

2.3.2 Priming techniques

Selden *et al* [24] and Allston *et al* [23] both implement the concept of priming in their work. In [24], Selden *et al* present a new approach in the design and control of SMA actuators whereby an SMA wire is divided into multiple segments whose thermal states (*hot* or *cold*) are controlled individually using Peltier junctions [7].

The idea is that rather than actuating the entire length of the wire, the proposed

[7]Peltier Junctions are thermo-electric heating and cooling devices that feature reliable solid state temperature control.

method controls the thermal state of each individual segment. As a result, the total strain of the SMA wire will be proportional to the length of the heated segments. Selden *et al* [24] implement what they call a *Hysteresis Loop Control* (HLC) to control the actuation of the SMA wire. This control method uses four user-specified temperatures as follows:

- Hot temperature (T_H): this is the temperature that the SMA segment must temporarily reach to ensure that it has reached its austenite state and the required strain has been achieved.
- Hot-to-cold transition temperature (T_{HC}): the temperature at which the SMA segment should be maintained after reaching T_H before receiving an input command to change state to the cold temperature T_C.
- Cold temperature (T_C): the temperature the SMA segment should reach after T_{HC} to ensure that it is in the martensite state and that the segment has expanded to its original length.
- Cold-to-hot temperature (T_{CH}): the temperature at which the SMA segment should be maintained after reaching T_C and before receiving an input command to change state to T_H.

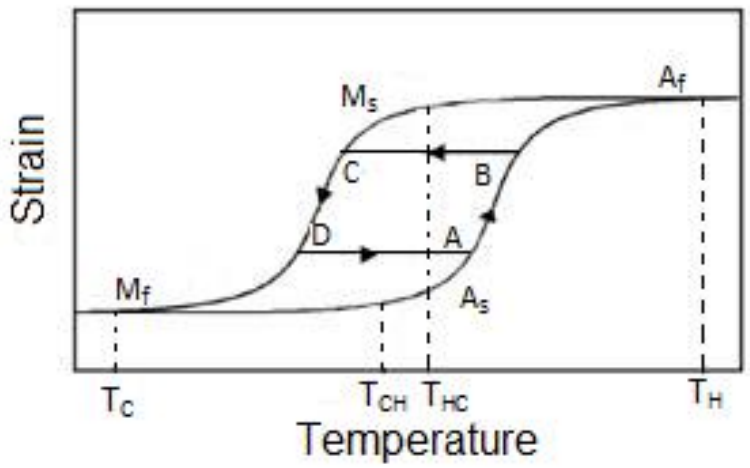

Figure 2.19: The four user-specified temperatures in HLC [24]

When a segment receives a command to switch from the OFF state to the ON state, the control method heats the SMA segment from T_{CH} to T_H and then immediately cools it down to T_{HC}. On the other hand, if it is instructed to switch

in the opposite direction, the segment is cooled from T_{HC} to T_C and then heated up to T_{CH}. The two intermediate temperatures, T_{CH} and T_{HC}, are chosen close enough to the austenite start, A_s, and martensite start, M_s, temperatures respectively as this helps reduce the heating and cooling latency times. Selden *et al* [24] also state energy efficiency as an advantage of HLC method since the extreme temperatures T_H and T_C are only needed for short time intervals.

To further reduce latency times in switching between states, Selden *et al* [24] improved their HLC by incorporating an algorithm for selectively controlling a specific group of segments. If for example, the SMA wire is to be extended, a group of segments, different from those that have been heated to contract the SMA, are simultaneously cooled from T_{HC} to T_C. The overall control system is depicted in Figure 2.20.

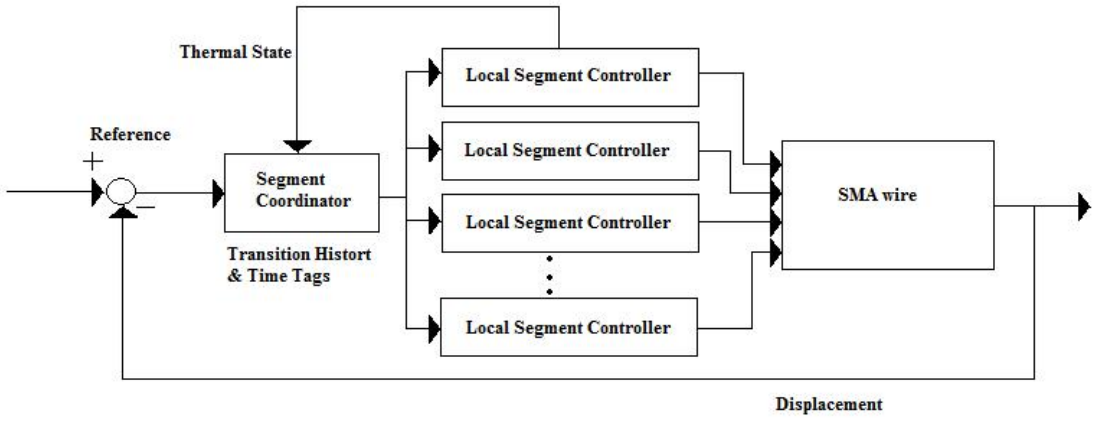

Figure 2.20: HLC with segment coordinator and local segment controllers [24]

However, an inherent characteristic of SMAs is that changes in stress cause shifts in the temperature-strain curves. If a shift takes place resulting in the operating temperatures T_{HC} and T_{CH} moving into the transitional areas of hysteresis, HLC will no longer be valid. Therefore, Selden *et al* [24] emphasize the importance of having a stress margin to ensure that phase transition does not occur within a specific stress range.

As in [24], the idea of maintaining the SMA wire at an intermediate state to help reduce the transformation latency times is employed in the work presented here. In particular, the same concept will be used in reducing the heating latency time as this research is only concerned with the consistent actuation of the SMA wire under different ambient temperatures and does not consider the aspect of cooling

it. As will be shown later, this will be the purpose of the *priming segment* where the wire will be maintained at a transition state before its complete transformation to austenite.

Allston *et al* [23] also implemented a form of priming. Their technique involved using electrical resistance feedback during the application of the high voltage to detect when the SMA element has transformed into austenite. Once this happens, voltage control is switched to a lower value maintaining the SMA element at a state from which it can quickly cool down to its martensite state. They stated that this priming technique, together with the forced convection technique mentioned earlier, helped reduce the cooling response of the SMA wire [23].

One note to make here is that the priming technique employed in [23] is opposite to the one used in this research. In [23], priming was used to maintain the SMA at a state that will reduce the transformation time to martensite. However, in this research, priming is used to maintain the SMA at a state from which it can quickly transform to austenite.

2.3.3 Actuation and priming research in this thesis

The actuation techniques discussed in Section 2.3.1 are very similar to the one employed in this research. However, the goal of the actuation strategy that will be presented here is not only to contract the SMA wire in the shortest period of time, but also to actuate it in approximately the same amount of time regardless of the ambient temperatures. As for priming, all the techniques that have been described in this thesis thus far, can be qualified as *fixed* priming techniques. The word *fixed* refers to the fact that parameters such as resistance targets or feed forward currents are fixed and not changing according to varying temperatures and stresses. Despite the fact that some of the techniques discussed above were designed to achieve robust actuation under varying ambient conditions, they did so at the expense of performance. For example, the 'stress margin' introduced by Selden *et al* in [24] and the safety margin that Featherstone and Yee [6] added to the threshold resistance value, R_{thresh}, will adversely affect the bandwidth of the SMA wire. Therefore, despite the benefits afforded by the aforementioned priming techniques, further improvements are necessary to allow SMAs to be utilized in more dynamic environments.

Having said this, the focus of this research is to develop and implement *adaptive* priming whereby resistance targets and feed forward currents are set according to

the ambient conditions and the stresses applied to the SMA elements. The research goal is realized in the design and implementation of a controller that will actuate an SMA wire in a consistent time regardless of the ambient temperature. This is achieved with adaptive priming along with intelligent thermal control by using parameters obtained through an investigative probing segment. *Probing* is an open-loop adaptation process used to determine a driving current value that will result in wire actuation under a given set of environmental conditions and applied stresses [7]. The current at which actuation begins, as determined in the probing segment, is defined as the maintenance current [7]. This current, which inherently incorporates the effect of ambient thermal and stress conditions, is then used to determine the priming and actuation currents applied by the controller.

Chapter 3

Pulse width modulated- vs analog- current drivers

In the original set of experiments that were conducted using the in-lab setup [7], an analog current signal was used to drive the SMA wire. However, at low current values, e.g. 0.1 A, the resistance values, calculated by dividing measured voltage by measured current, were very noisy. This can be attributed to the relatively constant amplitude of the power supply noise that degrades the signal-to-noise ratio (SNR) at low currents. One solution to this problem is to use a PWM-based current driver. The idea is to sample the voltage across the SMA wire and the current flowing through it during the on-cycle of the PWM pulse. This means, that even when the effective current flowing through the SMA wire is low, the resistance is computed using a high current. This ensures a high enough SNR that would yield "cleaner" resistance values.

In [26], Ma and Song designed a PWM-PD controller to control the position of SMA actuators. They cited a number of advantages for using PWM. First, it is robust to disturbances [26]. This can be explained by the example given in the previous paragraph where, the noise introduced by the power supply will not have any significant impact on the computed resistance if the voltage and the current are sampled during the on-cycle of the PWM signal. Second, it can be easily implemented using microprocessors. Another advantage of using a PWM signal to actuate the SMA wire is that it will reduce the amount of energy dissipated or wasted during the actuation process. As will be seen later in this thesis, the amount of energy needed to actuate the wire depends on the ambient temperature. For example, 10 J of energy may be needed to actuate the wire at 0 °C in 1 s while at 20 °C, 5 J of energy may be sufficient to contract the wire completely during

the same period of time. Now, if the power supply provides 10 J of energy every second, this means that in the latter case, 5 J will have to be dissipated elsewhere to ensure that the wire does not overheat and consequently get damaged. Thus, 50% of the energy provided by the power supply will be wasted. However, with PWM signals, the duty cycle can be varied such that only the amount of energy required to actuate the SMA wire is provided, minimizing the amount of energy wasted elsewhere in the circuit. The PW-modulator implemented in [26] is depicted in Figure 3.1.

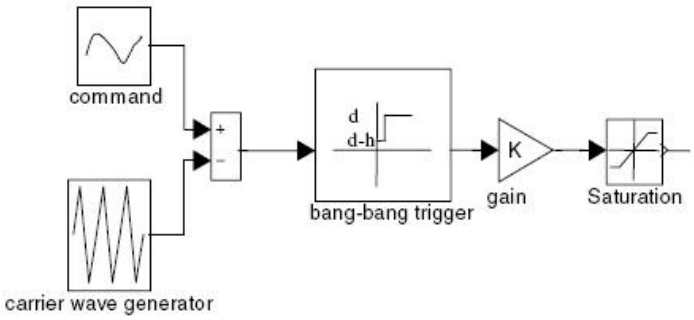

Figure 3.1: Pulse width modulator developed by Ma and Song [26]

To assess the effectiveness of their controller design, Ma and Song [26] conducted the same experiments under the same conditions using regular PD control, a pulse width pulse frequency (PWPF)-modulated PD control and PW-modulated PD control. It was found that the PW-modulated PD controller achieved the most accurate position control and the least energy consumption among the three controllers [26]. Although it had the longest settling time, no oscillations were observed in steady state as was the case with the other two types of controllers. This means that it added robustness to the system as the external disturbances now had little impact on the displacement of the SMA wire compared to the 3 V PWM signal that Ma and Song [26] used to drive the SMA wire. This, they point out, is vital in the case of SMA actuators especially when they are exposed to an open environment where they are susceptible to changes in convection conditions [26].

Having Ma and Song [26] demonstrate experimentally that using PWM adds robustness to the control of SMA actuators prompted the consideration of using PWM currents signals in the research of this thesis. Moreover, as Ma and Song [26] mentioned, the fact that PWM can be easily implemented using microprocessors made it a viable option.

3.1 PWM current driver testing

An experiment was carried out to measure the resistance of a 2 Ω 1% 25 W power resistor (Dale, model# 18602) while passing a PWM-driven current through it. The objective of this experiment was to compare the calculated resistance values obtained using PWM to those obtained when an analog current driver was applied, as implemented in the previous experiments [7], in terms of the resistance values' robustness to noise. The experimental setup also consisted of a 3 A N-channel MOSFET (IRF520V), a Xantrex power supply, a Quanser MultiQ-3 DAQ board, a Hall effect sensor (L01Z-050-S05) and a PC with MATLAB/Simulink installed on it.

The first step was to develop a testbed to compute the resistance of a load powered by a PWM-based current driver. This was done in Simulink [1] using a model that consists of 3 main parts. The model is shown in Figure 3.2. The first part, shown in Figure 3.2, is simply a constant voltage block of 5 V that is used to power up a Hall effect sensor that is used to measure the current flowing through the power resistor. The second part, also shown in Figure 3.2, consists of two sample & hold blocks that sample the voltage across the resistor and the current flowing through it at a rate of 10 kHz (the voltage and current input into the data acquisition board (DAQ) get sampled at the rising edge of every pulse of the PWM signal produced by the PWM generator). The last part, shown in Figure 3.3, was a PWM generator that transforms a square wave into a PWM signal with amplitude 5 V and a duty cycle that is a function of the analog command signal and that ranges from 5% to 100%.

[1] Simulink is a software package that comes with MATLAB for modeling, simulating, and analyzing dynamic systems

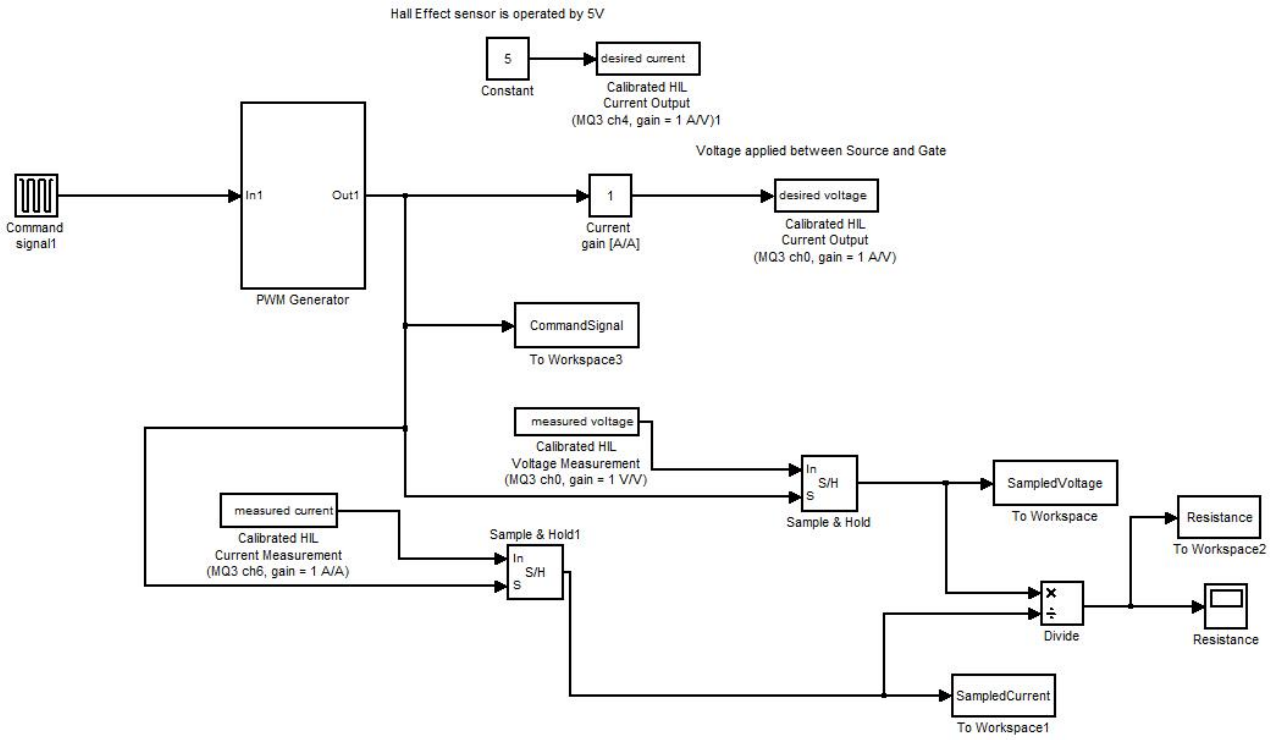

Figure 3.2: Simulink model of controller including PWM generator and DAQ board

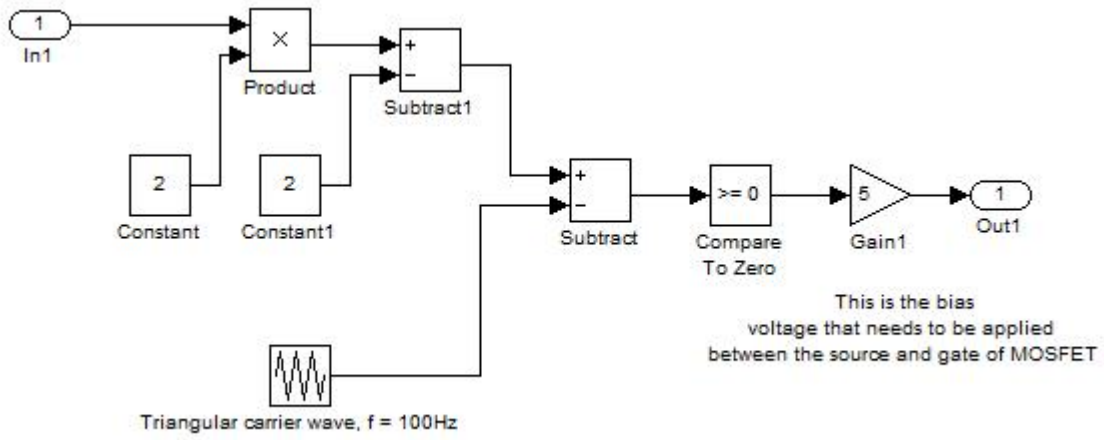

Figure 3.3: Simulink model of PWM generator

The experimental apparatus is shown in Figure 3.4. The Xantrex power supply was configured to operate in constant current-mode supplying a constant current of 2 A. The 2 Ω Dale power resistor and the N-channel power MOSFET were connected in series. The MOSFET was operated as a switch by applying a PWM signal with a magnitude of 5 V from the DAQ board across the gate and the drain. This resulted in a PWM current signal with a maximum amplitude of 2 A flowing through the resistor. The voltage across the resistor was input on one of the analog input channels on the DAQ board. The current flowing through it was measured using a Hall effect sensor and in turn input to another analog channel of the DAQ.

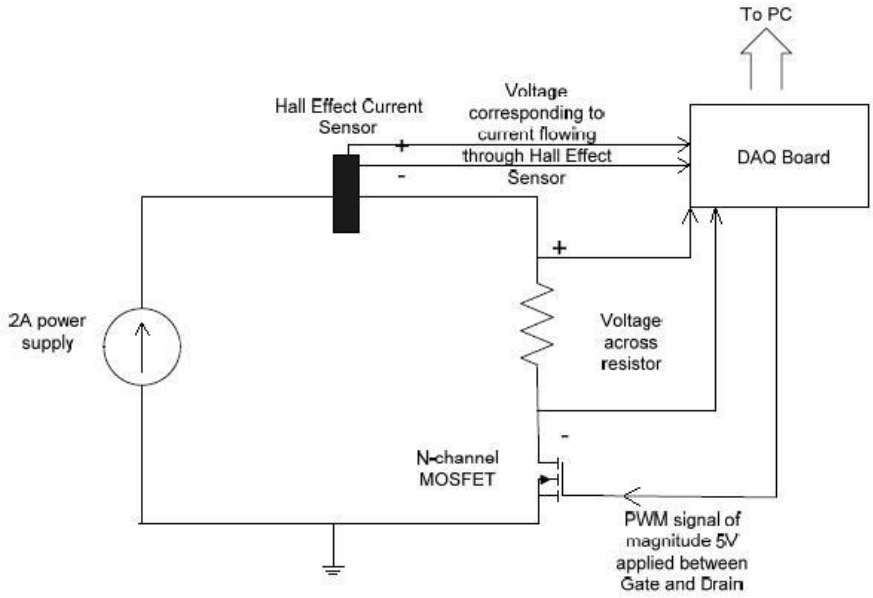

Figure 3.4: Block diagram of experimental setup

The Hall effect sensor, connected between the power supply and the load in Figure 3.4, was calibrated by passing several different currents through an SMA wire and measuring the voltage output from it to determine its gain and offset. The procedure followed was to increase the current in increments of 0.2 A and record the corresponding voltage. The values obtained are shown in Table 3.1.

Table 3.1: Calibration of Hall effect sensor

Current(A)	Output(V)
0	2.536
0.2	2.546
0.4	2.551
0.6	2.556
0.8	2.563
1.0	2.570
1.2	2.575
1.4	2.583
1.6	2.588
1.8	2.594
2.0	2.600
2.2	2.606
2.4	2.612
2.6	2.617
2.8	2.624
3.0	2.629
3.2	2.634

Excel [2] was then used to find the best fit line through the data points, the graph of which is shown in Figure 3.5. The sensor gain and offset were found to be 33 A/V and 2.5388 V respectively as seen in Figure 3.5.

[2]Excel is an application of Microsoft Office. It is a spreadsheet program which allows one to enter numerical values or data into the rows or columns of a spreadsheet, and to use these numerical entries for such things as calculations, graphs, and statistical analysis.

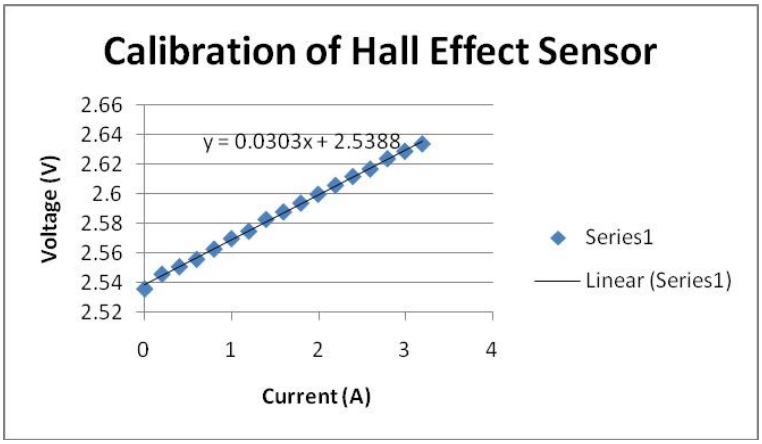

Figure 3.5: Best fit line through data points collected while calibrating the Hall effect sensor

Given Figure 3.5, the conversion from the voltage output from the sensor to the current it senses can be given by Equation 3.1.

$$Current = 33.\overline{0033} * (Voltage - 2.5388) \tag{3.1}$$

3.2 Experimental results

Once the Hall effect sensor was calibrated, the voltage measured across the SMA wire and the current flowing through it were sampled at a frequency of 10 kHz in Simulink. The voltage was divided by the current to give resistance values. A plot of the computed resistance values can be seen in Figure 3.6.

Indeed, the calculated resistance values obtained were robust to noise except for the spikes that appear in Figure 3.6. However, looking closely at the figure, one can observe that these spikes occur every 10 ms. In fact, these spikes occur at the rising edge of every 100^{th} sample. To get rid off these spikes, a unit delay was placed before the Sample and Hold blocks that appear in Figure 3.2 to delay the sampling of the voltage across the Dale power resistor and the current flowing through it by one period so that these signals are sampled at their steady-state values. Figure 3.7 depicts the new Simulink model.

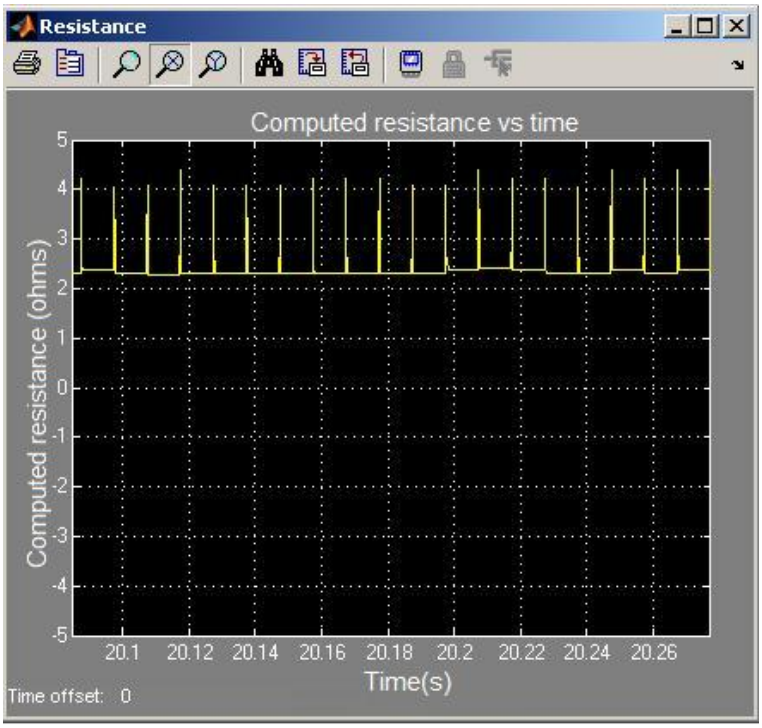

Figure 3.6: Plot of the computed resistance values with PWM current

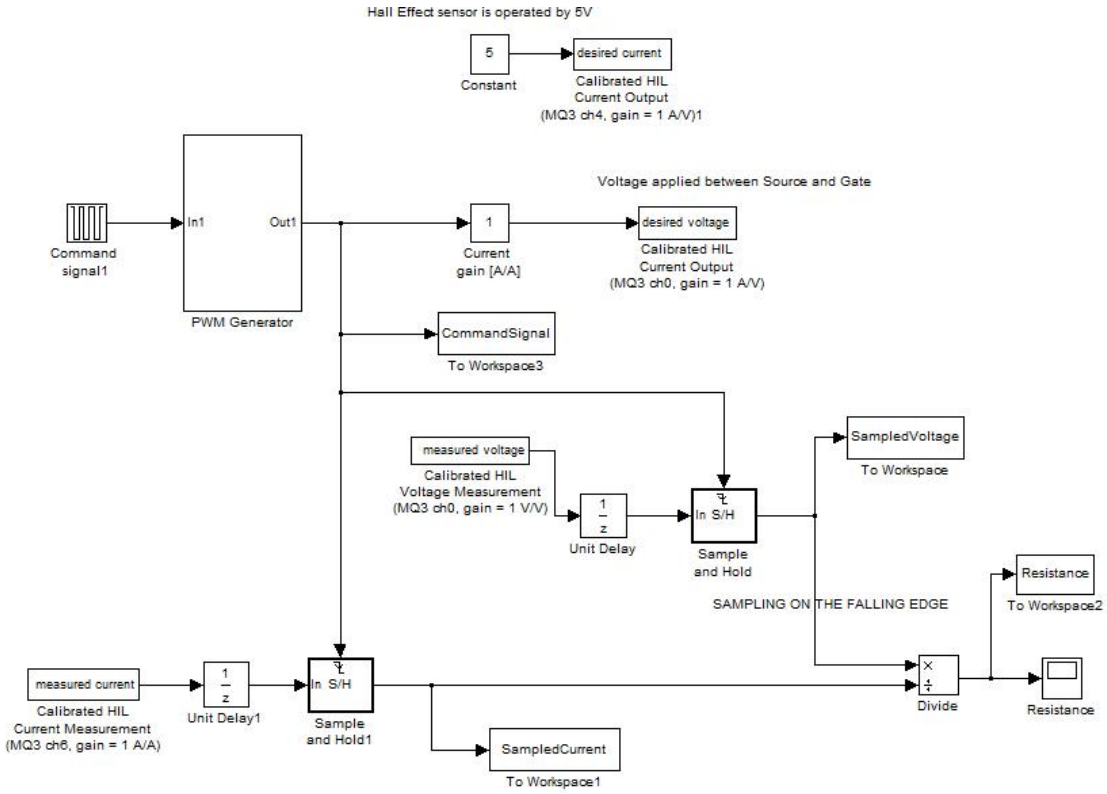

Figure 3.7: Modified Simulink model to remove spikes

3.3 Comparison between PWM- & continuous-priming current

To verify that a PWM current will indeed yield better resistance computations than those obtained via a continuous current, an experiment was conducted where a ramp current was passed through the Dale power resistor. Two runs were carried out: in the first run, a continuous current ramp was supplied. In the second run, a current ramp was supplied using PWM by varying the duty cycle. The timing sequence for the first run was as follows: 0.1 A for the first 20 s, the current then increases linearly from 0.1 A to 1 A between 20 s and 30 s and then decreases linearly back to 0.1 A for the following 10 s. Finally, the current is maintained at 0.1 A for the final 10 s of the experiment. The second run had a similar timing sequence except that this time, the PWM duty cycle was varied. The duty cycle is set to 5% for the first 20 s, the duty cycle then increases linearly from 5% to 50% at a rate of 5%/s between 20 s and 30 s and then decreases back to 5% at the same rate for the following 10 s. Finally, the duty cycle is maintained at 5% for the final 10 s of the experiment. The resistance computed from the collected voltage and current samples using the analog and PWM-based current drivers are shown in Figure 3.8 and Figure 3.9 respectively.

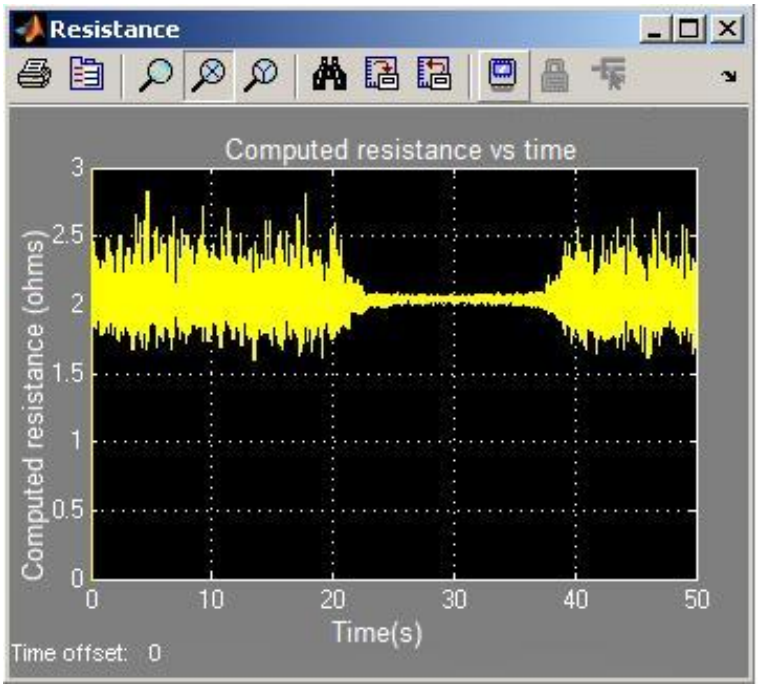

Figure 3.8: Resistance computations from applying a continuous current ramp

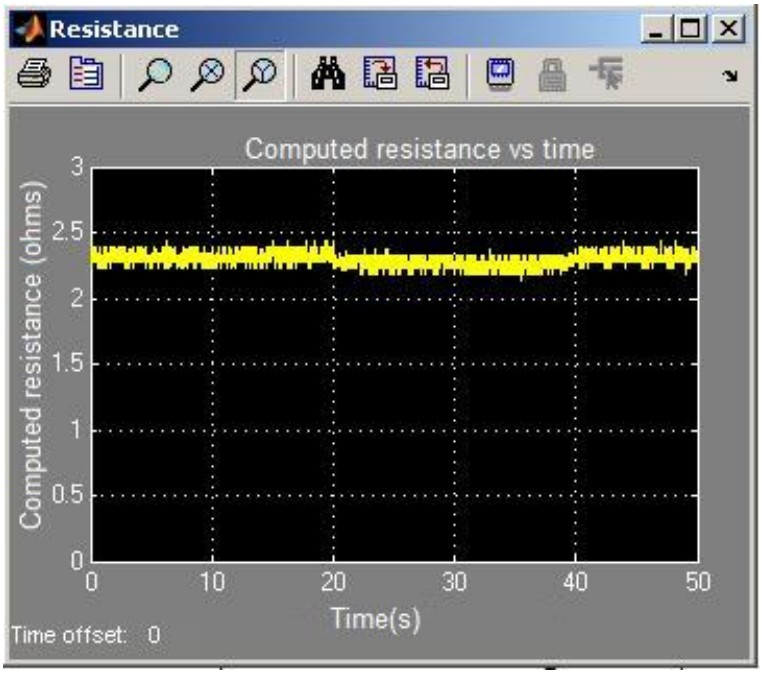

Figure 3.9: Resistance computations from applying a PWM-based current ramp

Looking at Figures 3.8 and 3.9, one can observe that applying a PWM current ramp made resistance computations more robust to noise compared to using a continuous current ramp. In Figure 3.8 the resistance varies between approximately 1.6 Ω and 2.9 Ω, whereas in Figure 3.9, resistance values are strictly between 2.1 Ω and 2.4 Ω. This is due to the fact that the voltage and current were sampled during the ON-pulse of the PWM signal thus increasing the signal-to-noise ratio (SNR). Thus, it can be concluded that employing PWM signals make resistance computations more robust to noise.

Chapter 4

Microcontroller-based embedded system

The goal of this research is to investigate an adaptive priming strategy for SMA wires with a view towards automotive applications. Thus, while in-lab experiments carried out in [7] were important for the initial proof-of-concept studies, subsequent work was required in a framework geared towards automotive applications. Hence, the next step in this research was to migrate the controller design to a microcontroller-based embedded system to run experiments outdoors under various ambient conditions. In this research, a 9S12 microcontroller from Freescale was used because it is tailored for automotive applications.

4.1 Objective

The advantages of migrating to a microcontroller-based system are two-fold. First, an embedded system achieves a more application-oriented setup compared to the in-lab setup that was used in initial work on this thesis and in [7]. The second benefit of migrating to an embedded system is that the hardware setup will now be mobile. Because the current in-lab setup is immovable, experiments on the SMA wire were only conducted under varying ambient wind conditions by operating fans at different speeds. This, however, cannot be used as a proxy for varying ambient temperature conditions. On the other hand, ambient temperature is difficult to regulate in the lab. The mobile embedded system, however, can be moved to a temperature-controlled chamber (or, potentially, outdoors) where the wire can be exposed to different ambient temperatures. This will ultimately aid in assessing the

effectiveness of the priming controller design presented in this thesis in actuating the SMA wire in a consistent time period under different temperatures.

4.2 Experimental setup

Figure 4.1 depicts the block diagram of the embedded setup.

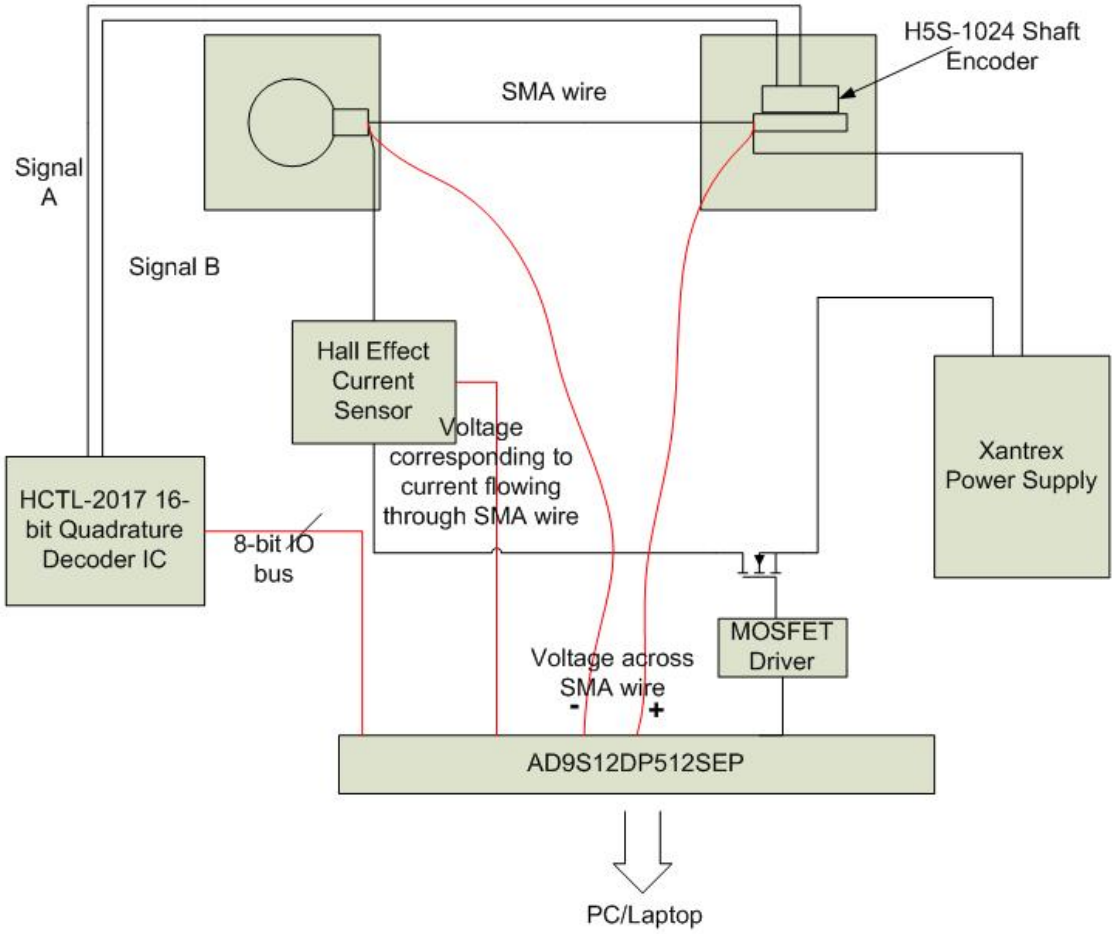

Figure 4.1: Block diagram of experimental setup

The major components of this experiment include: one Xantrex XPD 33-16 programmable power supply, one Xantrex XPD 7.5-67 programmable power supply (both configured to operate in constant voltage mode), a H5-1024-I-S ball bearing optical shaft encoder, an HCTL-2017-A00 decoder chip from Avago, a 5-pin latching /unterminated 5-wire discrete cable to connect the encoder and decoder chips, a AD9S12DP512M2 microcontroller board from TechnologicalArts, two solderless experimental boards connected to the Adapt12 board, an IRL3502PBF N-channel MOSFET, an ICL7667 Intersil dual power MOSFET driver, an ACS712 Allegro Hall effect based linear current sensor, a 22 cm 250 μm 90 °C Flexinol wire from Dynalloy, a Newport XYZ stage to which the SMA wire will be connected, a 0.85 kg mass which will be the load connected to the SMA wire, a MicroBDM12LX pod to download code onto the Flash memory of the microcontroller, a 25LC1024 1Mbit SPI bus serial EEPROM chip to store the collected data, a USB-RS232 serial converter cable, a commercial temperature controller from Omega, a refrigerator, a 40 W incandescent bulb, two thermocouples and finally a PC.

One end of the SMA wire is connected to a stationary XYZ stage while the other end is attached to a 0.85 kg mass. The H5S-1024 Shaft Encoder is mounted on the shaft of the pulley to measure the displacement of the wire. The shaft encoder signals A & B are decoded by the HCTL-2017-A00 quadrature decoder chip whose 8-bit IO bus is routed to one of the 8-bit input ports on the Adapt9S12DP512 board. With quadrature decoding of 4096 counts/revolution, a pulley diameter of 2.0 cm, the linear displacement measurement resolution is 0.0153 mm/count. The XPD 33-16 power supply is set to a constant voltage of 12 V, and used to power the microcontroller board. The XPD 7.5-67 power supply is set to 5 V, and provides switched power to the SMA wire. The positive end of this power supply is connected to one end of the SMA wire while its GND is connected to the source of the N-channel MOSFET. The drain terminal is connected to the opposite end of the wire while the gate terminal is connected to one of the PWM channels on Adapt9S12DP512. Thus, the MOSFET acts as a switch resulting in a PWM current flowing through the SMA wire. Finally, the voltage measured across the SMA wire and the voltage produced by the Hall effect sensor, corresponding to the current flowing through it, are input to 3 Analog-To-Digital (ATD) channels (2 channels for the differential voltage across the SMA wire and 1 channel for the output voltage from the current sensor). The conversion of the voltage output from the Hall effect sensor to the corresponding current value is done in software. Also, the resistance calculation is done in software on the Adapt9S12DP512 board.

The refrigerator is used as a temperature-controlled chamber. A commercial

temperature controller, shown in Figure 4.2, is used to regulate the temperature inside the freezer compartment of the fridge. The controller's relay output is connected to both the refrigerator compressor, used to cool the compartment, and an incandescent 40 W bulb within the compartment which is used for heating. One of the thermocouples is placed about 8 cm away from the wire to measure ambient temperature within the compartment. The second thermocouple is connected to the experimental jig to which the SMA wire is connected (shown here in Figure 4.3). This is to indicate when steady state temperature has been reached inside the refrigerator.

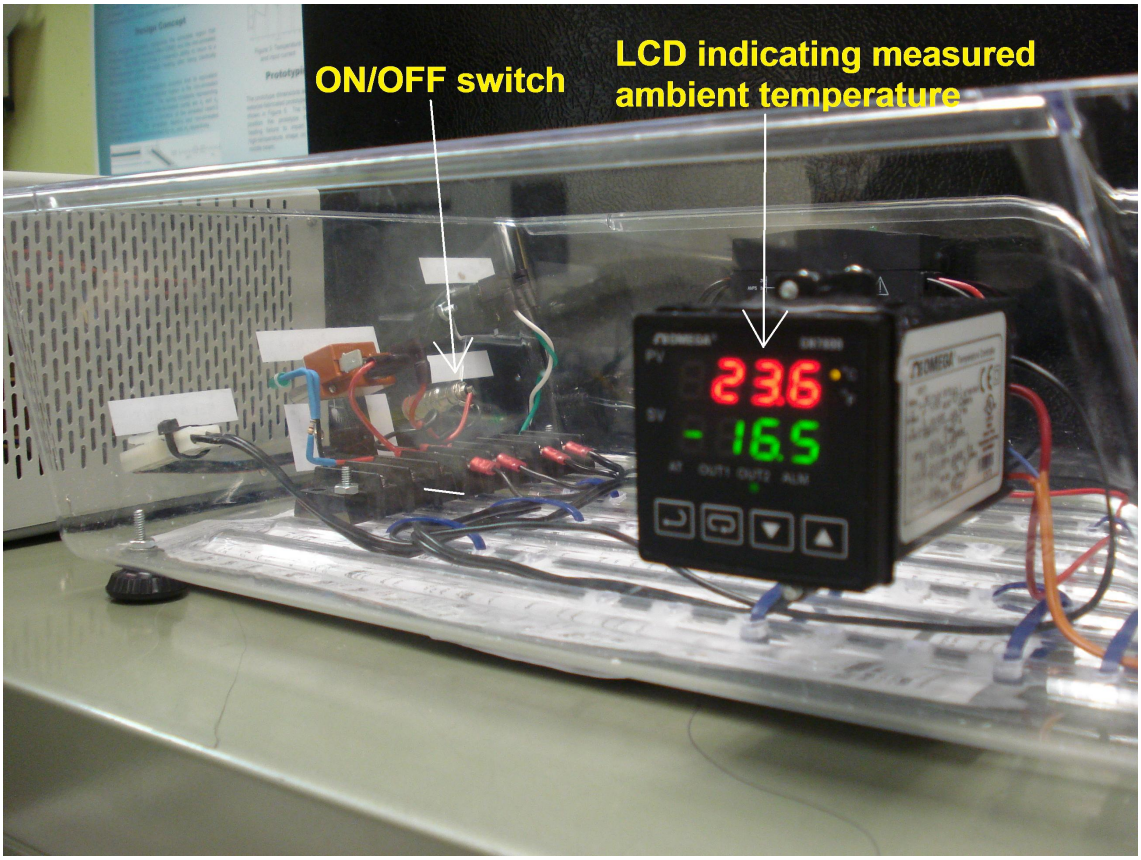

Figure 4.2: Temperature controller used to regulate temperature in freezer

4.3 Preliminary experimental results

Preliminary results were obtained by running an experiment where no priming technique was used. Figure 4.4 - Figure 4.6 show samples of the voltage across the SMA wire, the current flowing through it and the computed resistance of the SMA wire respectively.

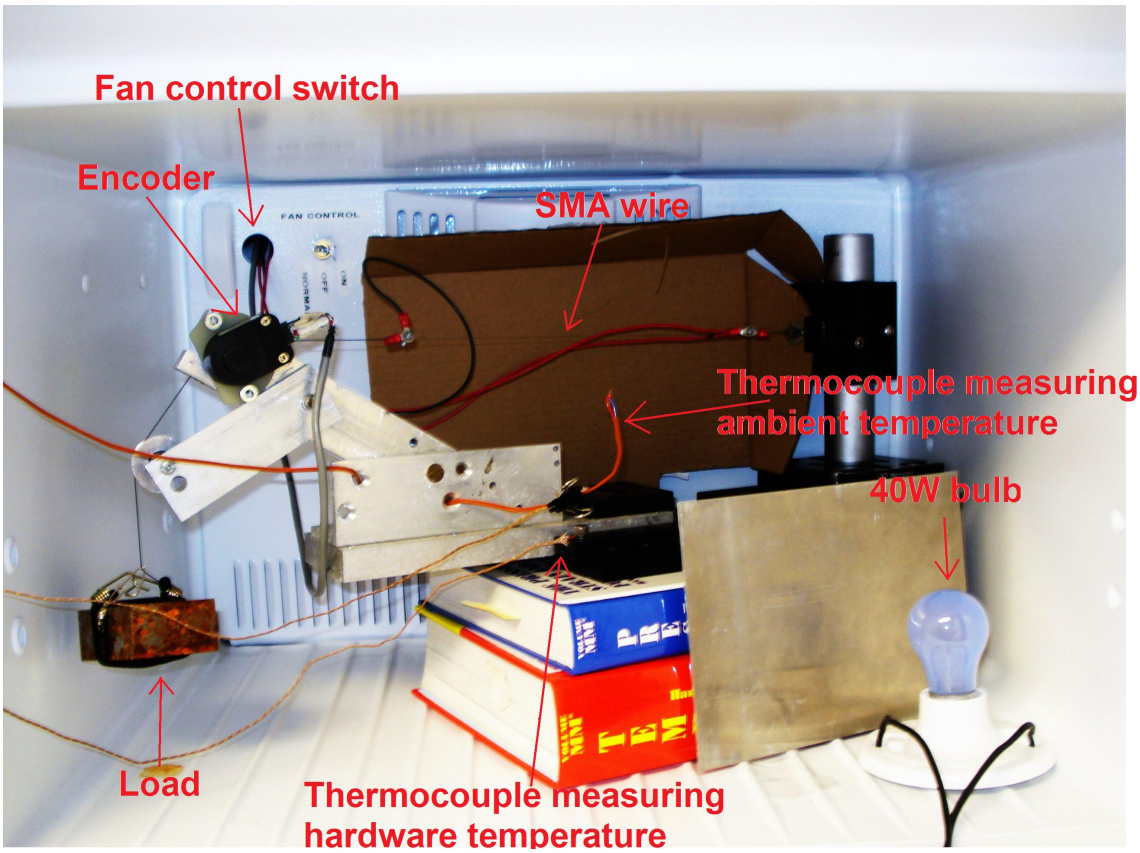

Figure 4.3: Experimental setup in the freezer

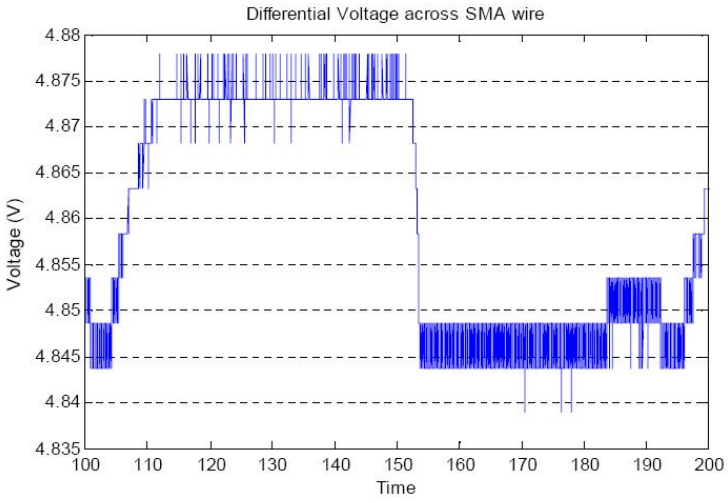

Figure 4.4: Differential voltage measured across the SMA wire

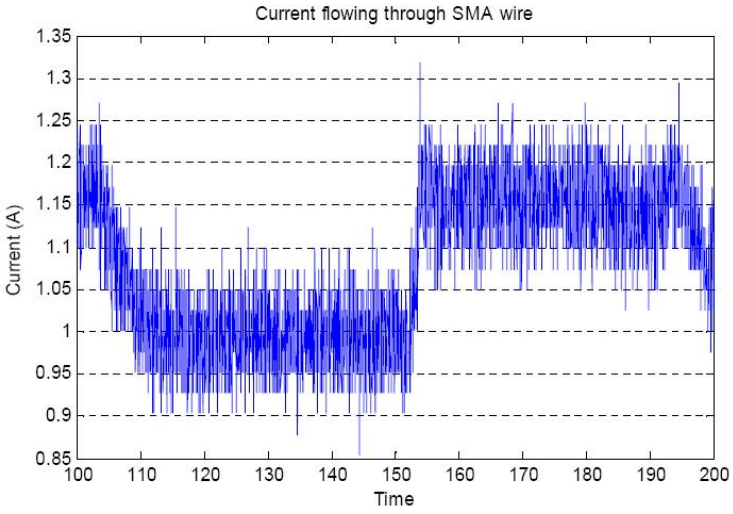

Figure 4.5: Current flowing through the SMA wire

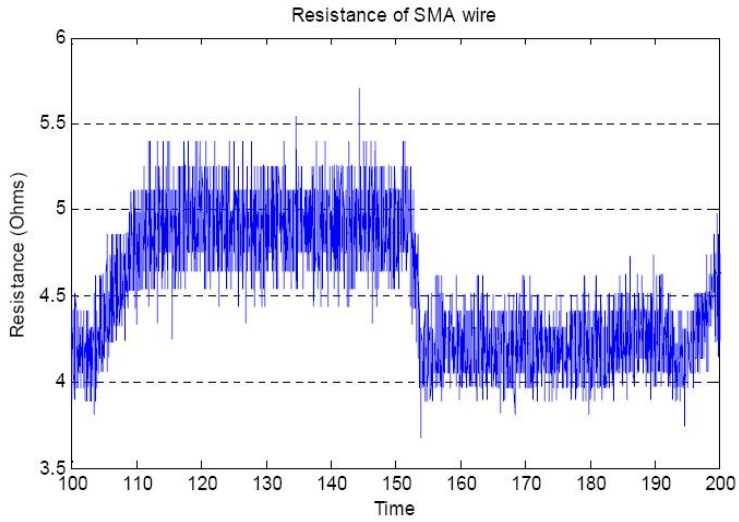

Figure 4.6: Computed resistance of the SMA wire

As can be seen in Figure 4.6, the resistance computed from the collected voltage and current measurements was found to be very noisy [1]. By closely looking at Figures 4.4 and 4.5, it is apparent that there was more noise on the current sensor output samples as compared to the voltage samples. The noise on the current produced an error of up to 8 levels (a level corresponding to a resolution of 0.00488 V) whereas the noise on the voltage produced a maximum error of only 2 levels. This is easily reflected in the computed resistance curve shown in Figure 4.6.

The control strategies implemented for priming rely on detecting the change in resistance levels from the high martensite values to the relatively low austenite values. If noise levels are too great, the transition may be masked by noise or conversely, noise spikes may give false indication of transition. Consequently, it was essential to investigate methods and techniques that could help in reducing this noise. In the next few subsections, the results obtained from investigating with noise filtering techniques implemented in software, Butterworth filters, and even the use of a different current sensor are presented.

4.3.1 Noise filtering techniques

To achieve better noise immunity, the first technique investigated was employing noise filtering techniques. Indeed, two filtering techniques were implemented in software:

1. Collecting 64 samples of the current sensor output voltage at 0 A and then taking the average. That average will be subtracted from the subsequent current sensor output voltages. The purpose of this technique is to remove the DC offset from the output of the current sensor. This is necessary as the offset resulted in erroneous current values. This is called Technique 1.

2. Collecting 32 samples during the on-cycle of the PWM signal, taking their average and then subtract from it the average obtained in Technique 1. This is to average out the noise on the current measurements due to white noise, noise on the V_{CC} and V_{DD} pins on the current sensor, etc. This is called Technique 2.

The mechanism of Technique 2 is shown in Figure 4.7. This represents the PWM signal that is generated by the PWM module of the microcontroller (the

[1] Note that the transition in mean value of resistance around t = 150 s is expected, as the wire undergoes a transition to austenite, which has a lower resistance than martensite.

PWM signal driving the SMA wire is the inverse of the one shown in Figure 4.7 due to the use of the ICL7667 Intersil dual power MOSFET driver which is basically an inverter). Rather than sampling at the falling edge, the sampling process takes place $\approx 20\,\mu s$ after the onset of the falling edge of the PWM signal. This is to ensure that the collected samples do not suffer from noise due to the high frequency content existing at the edges.

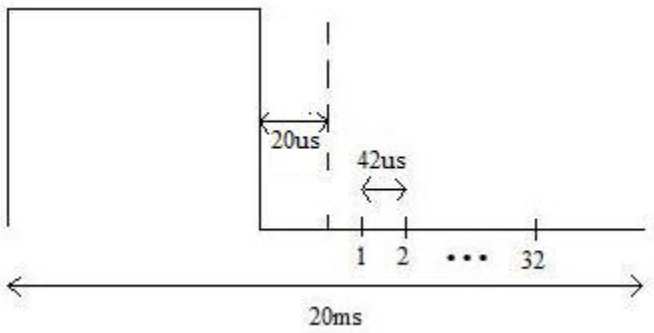

Figure 4.7: 32 samples taken during the on-cycle of the PWM signal

In a new experimental run, Technique 1 was implemented first. As can be seen in Figure 4.8, there was a slight improvement in the resistance computations. The calculated resistance values in Figure 4.8 lie in the range between $3.7\,\Omega$ and $4.9\,\Omega$ whereas in Figure 4.6, the range was between $3.8\,\Omega$ and $5.5\,\Omega$.

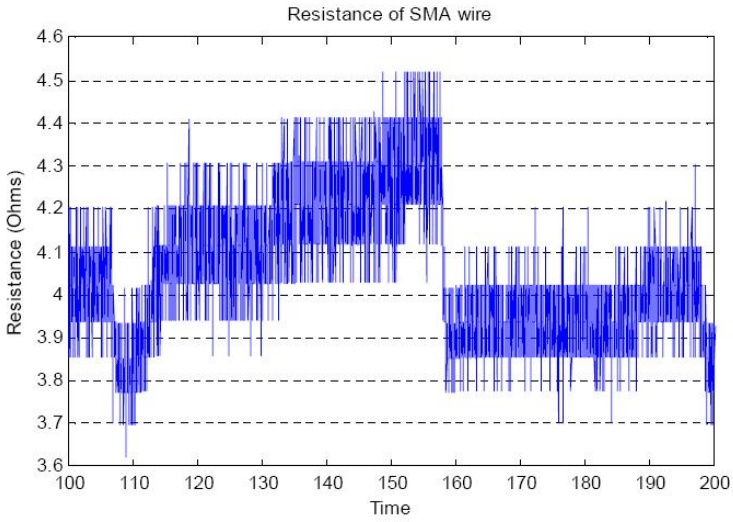

Figure 4.8: Resistance values after employing Technique 1

Despite implementing the first filtering technique, there were a lot of spikes on the computed resistance as evident in Figure 4.8. Thus, the second filtering

technique was integrated into the code to investigate its effectiveness in reducing noise on the computed resistance values. A graph of the computed resistance after combining the two noise filtering techniques can be seen in Figure 4.9. Indeed, the computed resistance was far less noisy and the resistance now varied between only 3.8 Ω and 4.7 Ω. Moreover, given that Figure 4.9 clearly shows the resistance of the SMA wire increasing to the cusp prior to actuation, and then decreasing to its lower austenite value during actuation (at t = 159 s), implementing the second filtering technique enables the detection of changes in the resistance of the SMA wire as it undergoes several cycles of of actuation, priming and cooling in the actual control experiments that will be discussed later in this thesis.

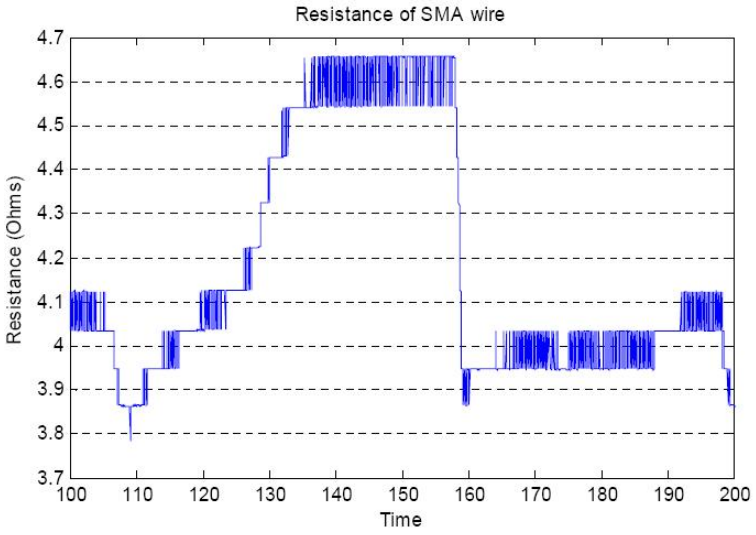

Figure 4.9: Combining the two noise filtering techniques

Another measure taken to reduce the noise on the collected data was to increase the number of analog-to-digital (ATD) clock periods that the microcontroller spends to complete an ATD conversion. This is possible given the fact that ATD conversion on the AD9S12DP512M2 microcontroller is divided into two phases. The first phase is made of up of 2 ATD clock periods, whereas the second phase is programmable and can be set to 2, 4, 8 or 16 clock periods. The 9S12D provides this configuration in order to allow designers to trade off conversion speed for accuracy. In the application note AN2428 from Freescale, it is stated that increased conversion accuracy can be achieved by using a higher number of clock periods for the second phase of the ATD conversion. Hence, a couple of experiments were conducted with the second phase of the ATD conversion increased to 8 and 16 ATD clock cycles.

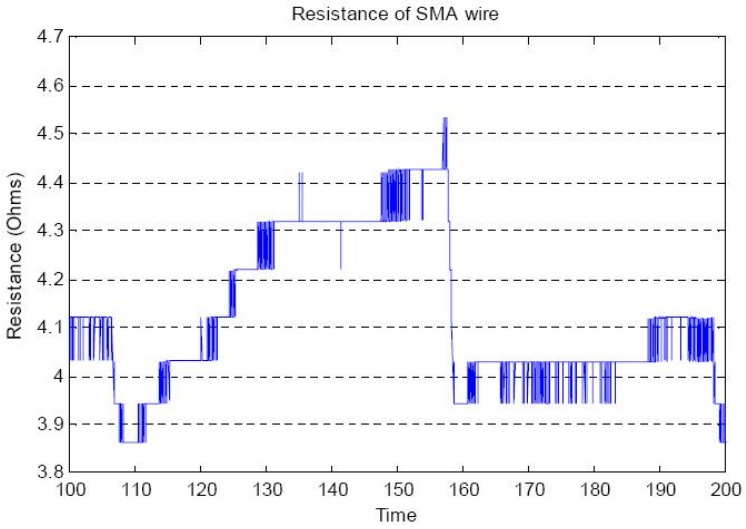

Figure 4.10: Increased 2nd phase of ATD conversion to 8 ATD clock cycles

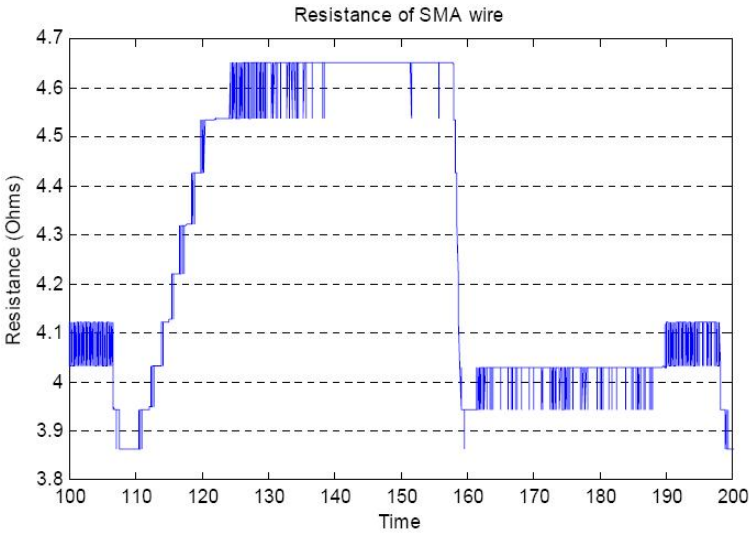

Figure 4.11: Increased 2nd phase of ATD conversion to 16 ATD clock cycles

Since Figures 4.10 and 4.11 show similar performance in terms of noise rejection, the second phase of the ATD conversion was set to 16 ATD clock cycles.

As can be seen in Figures 4.10 and 4.11, the computed resistance values were far "cleaner" than the original set of computed resistance values that were obtained without implementing any filtering techniques. Given that the length of the SMA wire under stress is about 22 cm and that the resistance per unit length for the SMA wire used is $0.197\,\Omega$/cm [12], the expected resistance for the SMA wire used is approximately $4.33\,\Omega$. Since the filtered resistance values (blue curve in Figure 4.12) varied between approximately 4 - $4.5\,\Omega$, this indicates that the noise filtering techniques implemented were in fact successful in removing considerable noise.

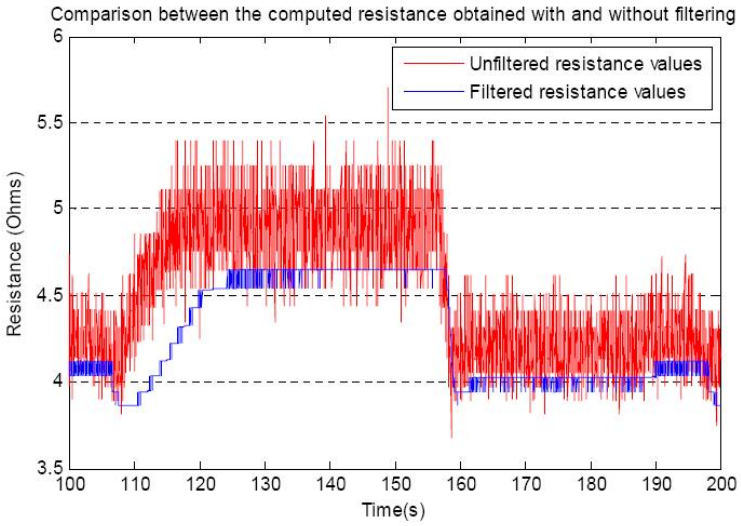

Figure 4.12: Filtered and Unfiltered resistance values

One should note, however, that since in the filtered case, 32 samples are collected during the on-cycle of the PWM signal and then averaged, and given the fact that it takes 42 μs to complete a conversion sequence of 3 channels (2 representing the differential voltage and 1 for the current), a delay is expected of at least 1.344 ms between the filtered and unfiltered data. However, this delay should not present a problem in the real-time control of the actuation of the SMA wire since it usually takes place in the order of tens of milliseconds.

However, despite implementing the noise filtering techniques described earlier in this section, noise can still be observed on the calculated resistance. It was important to determine whether this noise was an artifact of the current sensor or whether it was due to the high frequency components of the PWM signal. Therefore, in order to investigate the root cause of this noise, two sets of experiments were conducted to collect Hall effect sensor output voltage data: one set of experiments at 0 A and the other set of experiments at a duty cycle of 10% which is the minimum duty cycle that can be used to allow for the averaging of samples inplemented in Technique 2. Note that in the following experimental runs, the software-implemented noise filtering techniques varied from one experiment to the other. This was done simply to understand which technique contributed more to noise removal. Another thing to note is that the following plots depict the output voltage from the current sensor and not the computed resistance values. This is because for some of these experiments, the current was reduced down to zero. During these periods i.e. when the current is zero, the voltage measured across the SMA wire will also be 0 V and thus, it will not be possible to compute resistance.

Experiments were first conducted at 0 A, collecting data for 10 s. Figure 4.13 depicts the voltage output from the current sensor.

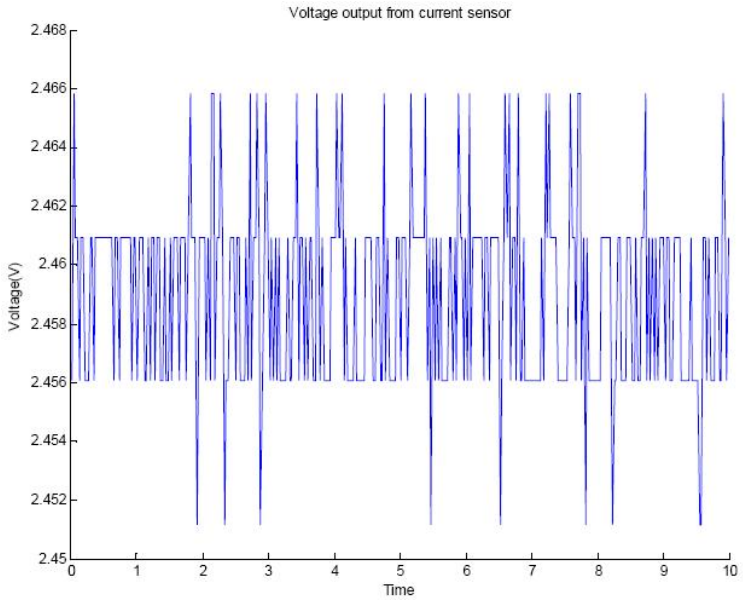

Figure 4.13: Output voltage of current sensor at 0 A

As can be seen from Figure 4.13, the maximum difference between any two consecutive samples is three ATD quantization levels (i.e. 14.4 mV). Since the current is 0 A, this indicates that the noise component is independent of the high frequency components of the PWM signal. Possible sources of this noise could be the noise on the V_{CC} and V_{DD} pins of the sensor, noise coming from the power supply itself or EMI from using unshielded measurement cables.

The exact same experiment was run again but this time with each data point representing the average of 32 samples taken during each on-cycle of the PWM signal. As can be seen from Figure 4.14, the averaging technique employed was effective in completely removing the noise.

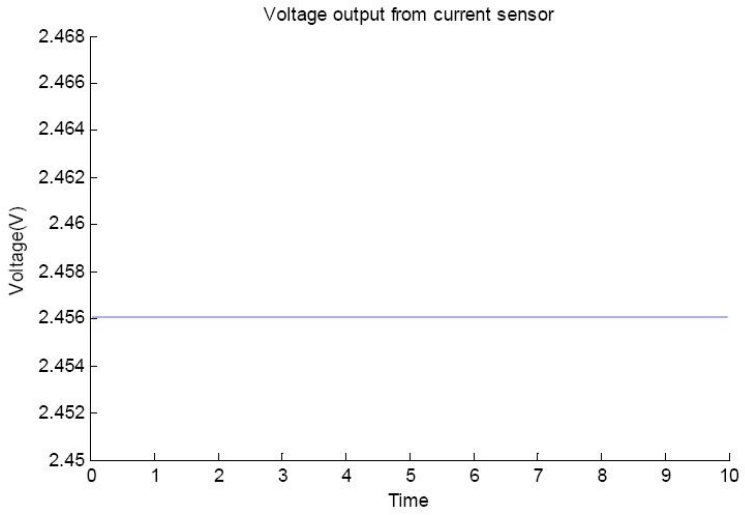

Figure 4.14: Output voltage from current sensor using noise filtering at 0 A

To make sure that there was no other noise component affecting the resistance computations, a new set of experiments were run but this time using a PWM current with a duty cycle of 10%. In the first experiment, no noise filtering was used. The results are depicted in Figure 4.15.

Again, the maximum difference between any two consecutive samples was three quantization levels. Given that this figure is similar to Figure 4.13, one can infer that there is no noise component due to the high frequency components of the PWM signal.

To test whether the averaging technique will aid in removing this noise, the experiment was run again this time implementing Technique 1. The results are shown in Figure 4.16.

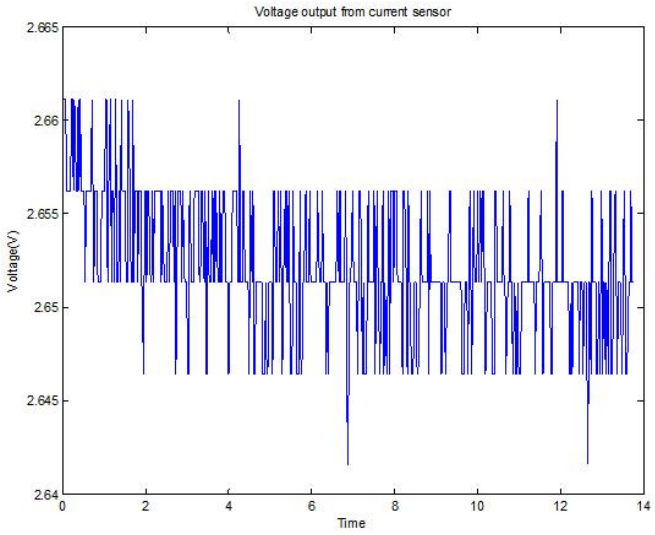

Figure 4.15: Output voltage of sensor without noise filtering at duty cycle = 10%

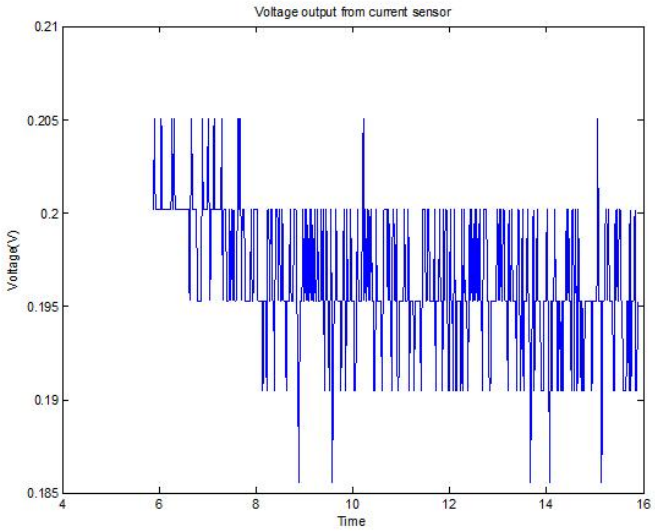

Figure 4.16: Output voltage of sensor employing Technique 1 (duty cycle = 10%)

Again, the maximum difference between any two consecutive samples was three quantization levels. The experiment was run one more time implementing Technique 2 with the results shown in Figure 4.17.

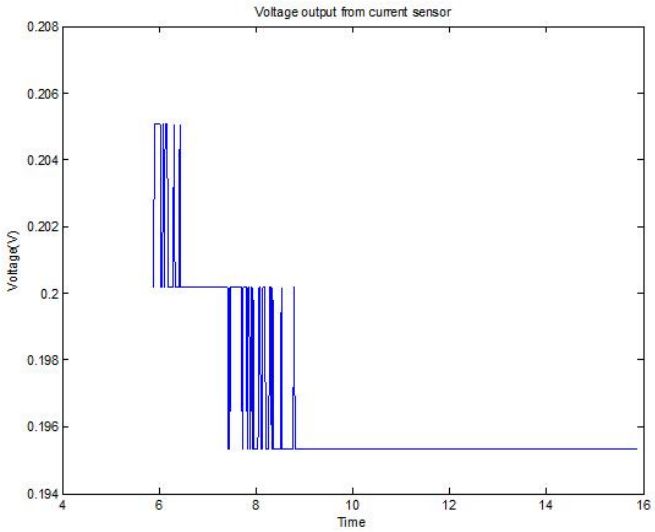

Figure 4.17: Output voltage of sensor using Technique 2 (duty cycle = 10%)

As can be seen from Figure 4.17, the maximum voltage difference between two consecutive samples is only one quantization level. Moreover, this is only the case for the first 3 seconds of the actual experiment; between 5.87 s and 8.87 s (the first 5.87 s represent the time taken to collect the 64 samples at 0 A). Starting at t = 9 s, the voltage output of the current sensor is noise-free. This makes sense as the current control signal used was a PWM signal with 10% duty cycle. The spikes seen at the beginning can be attributed to the resistance of the SMA wire changing as it is being heated. As the temperature of the SMA stabilizes, the rate of change in the length of the wire decreased considerably as seen in Figure 4.18 and thus the rate of change in resistance also diminishes. This is further proof that the noise observed in previous runs is independent of the high frequency components of the PWM signal.

4.3.2 Using Butterworth filters

Despite the fact that the software-implemented filtering techniques presented in the previous section helped reduce the noise on the resistance calculations considerably, the computed resistance values in Figure 4.11 are still considered, for the purpose of

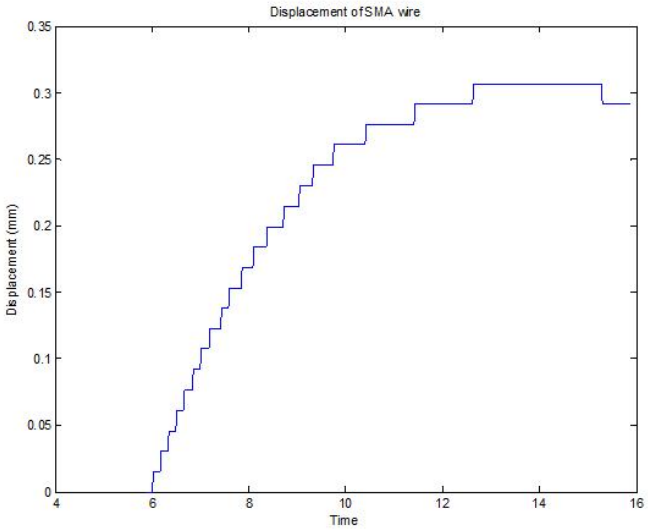

Figure 4.18: Displacement of SMA wire when driven with a 10% duty cycle

the controller design in this thesis, unsatisfactory. This is due to the noise evident at the top parts of the resistance curve (i.e. at the higher resistance values). This poses a problem since it is vital to have a smooth resistance curve in these areas as the priming controller developed in this research depends on detecting this "cusp" in the SMA resistance to determine the PWM duty cycle at which the wire starts actuating.

Consequently, another measure considered for smoothing out the resistance curve was the use of a filter such as a 2nd-order Butterworth filter. However, care should be taken in the design of this filter as it could introduce a significant delay that would consequently hinder the ability of the controller to actuate the wire in a timely and predictable manner. Since an SMA wire typically actuates in the order of tens of milliseconds, and since the smallest width of the PWM ON-pulse will be 2 ms, the delay introduced by the filter should be in the order of microseconds. If a 2nd-order or even a 1st-order Butterworth filter is used, this will correspond to a cutoff frequency in the order of kHz or MHz. Since the sampling frequency used in all experiments is 50 Hz, the noise observed on the computed resistance measurements will not be filtered out by the Butterworth filter. Consequently, using a filter is worthless in terms of noise rejection.

4.3.3 Using a high precision current sense resistor

Since using a filter would introduce a significant delay that will hinder the controller's ability to actuate the wire in a timely and predictable manner, other measures had to be investigated in an attempt to further reduce the noise visible at the peaks of the resistance curves.

One measure that was investigated was the use of a different current sensor with a current range that better matches the current flowing through the SMA wire. This makes sense considering the fact that the range of the Allegro current sensor used is between -5 A and 5 A. With collected current samples ranging from 0 A to about 1.3 A, less than 13% of the full range is effectively being used. Thus, a 0.03 Ω, 1% tolerance Type SR precision current sense resistor from Caddock Electronics with a power rating of 2.0 W was used to measure the SMA current. This had the further advantage of decreasing system size and cost, making it a better choice for automotive applications.

A new experimental trial was conducted with the new current sense resistor and implementing the noise filtering techniques. The voltage, current and resistance values are depicted in Figures 4.19 to 4.21 respectively .

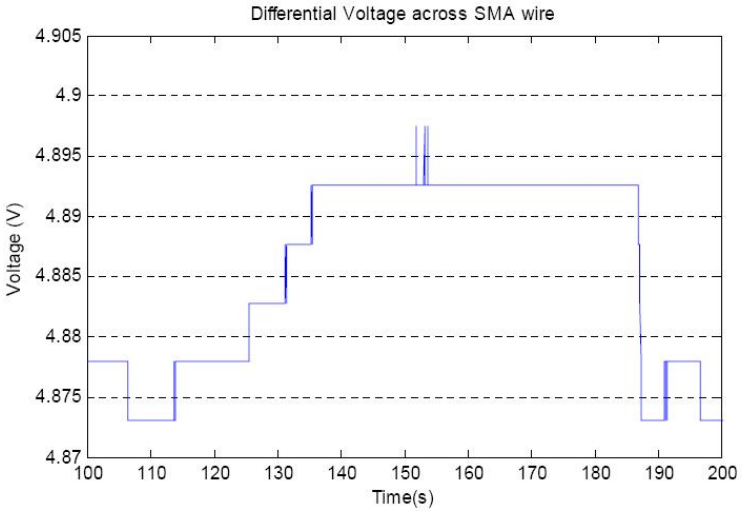

Figure 4.19: Voltage across the SMA wire (with 32-sample averaging)

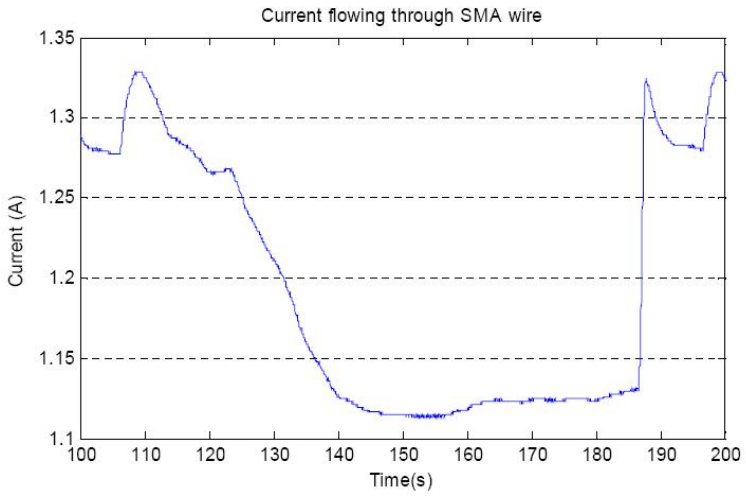

Figure 4.20: Current flowing through the SMA wire (with 32-sample averaging)

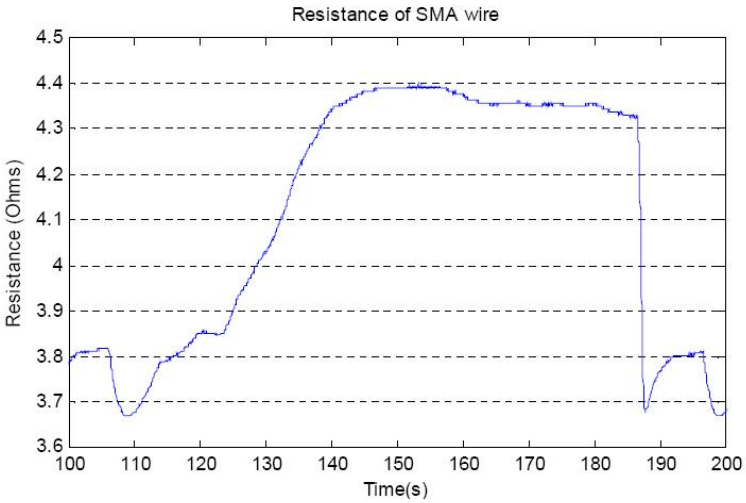

Figure 4.21: Computed resistance of the SMA wire (with 32-sample averaging)

As evident in Figures 4.19 to 4.21, using the current sense resistor resulted in far less noisy resistance computations, increasing the likelihood of the priming controller detecting the cusp in the resistance of the SMA wire upon actuation. To investigate whether implementing the software filtering techniques will continue to have any significant impact on the collected data after using the current sense resistor, a further experiment was run without implementing them. The yielded results are depicted in Figures 4.22 to 4.24.

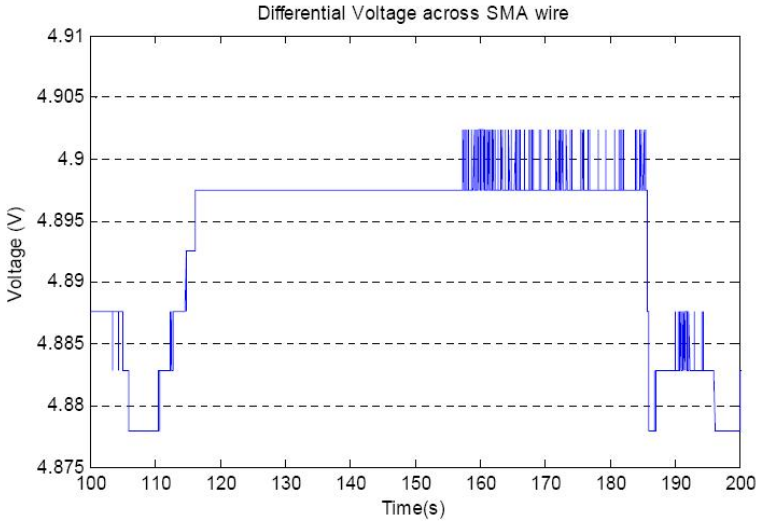

Figure 4.22: Voltage samples collected from new hardware setup (no noise filtering)

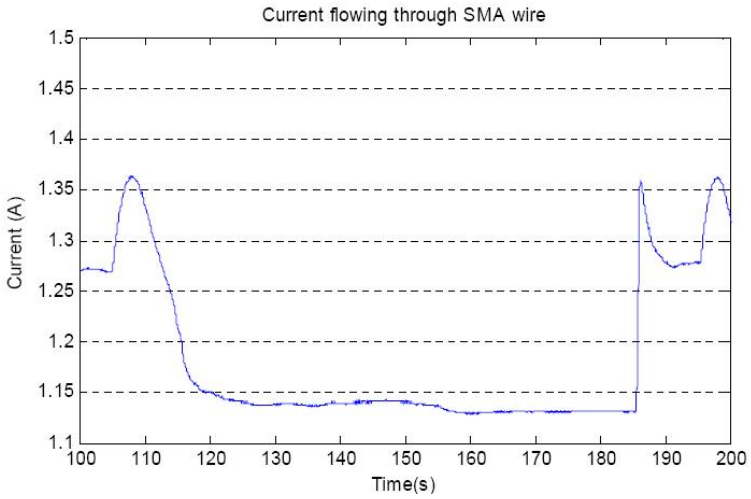

Figure 4.23: Current corresponding to output of current sense resistor (no noise filtering)

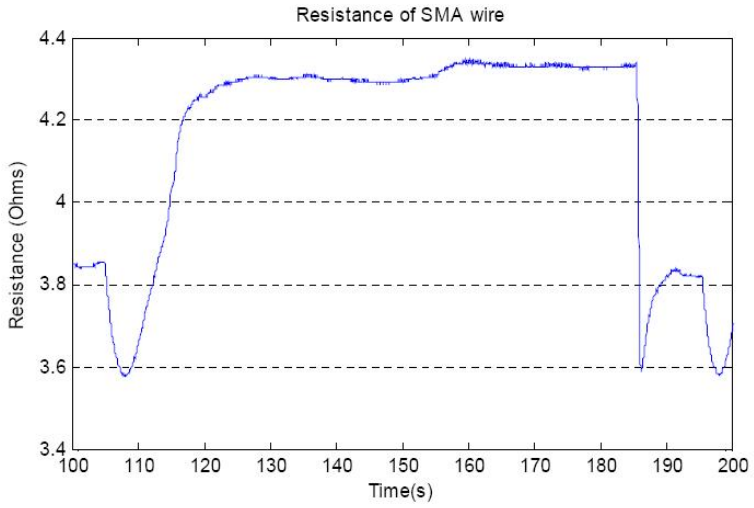

Figure 4.24: Computed resistance from new hardware setup (no noise filtering)

Comparing Figures 4.19 to 4.24, the results obtained using the current sense resistor were very comparable in terms of noise rejection whether the noise filtering techniques were employed or not. In deciding whether or not to include them in the code, not implementing the software techniques has 3 advantages:

1. The software will become less complex.

2. Given the fact that in Technique 2, 32 samples are collected during the on-cycle of the PWM signal and then averaged, and given the fact that it takes 42 μs to complete a conversion sequence of 3 channels (two representing the differential voltage and one for the current), a delay of at least 1.344 ms will exist between the instant the data is sampled and the instant it gets stored in the external memory. If the implementation of Technique 2 is dropped, this delay will no longer exist.

3. Also, implementing Technique 2 would require that the signal remain low for at least 1.364 ms after the falling edge (look at Figure 4.7) for data to be sampled and averaged to be ready for storage on external memory. This was found to constrain the minimum duty cycle that can be applied to the SMA wire to 10% which yields an off-pulse duration of 2 ms. However, if this noise-filtering technique is removed, lower duty cycles can be applied.

Thus, the noise filtering techniques were removed from the embedded code.

However, it should be noted that a number of additional changes were made to the hardware at this stage. First of all, in an attempt to simulate the car

environment, the 12 V-power supply was now used to power the SMA wire. This was to simulate the fact that the car battery (nominally 12 V) will be used to power the SMA actuator. The microcontroller and the rest of the circuit were powered by the 5V-power supply.

Since the voltage applied across the SMA wire was now 12 V, and given that the maximum voltage that can be input into one of the ATD channels is only 5 V, a voltage divider had to be used to ensure that the voltage input into the ATD channel is less than the maximum voltage rating. The voltage across the SMA wire was applied across a voltage divider consisting of 5 kΩ and 11 kΩ resistors, as shown in Figure 4.25. The voltage across the former was then passed through two buffers before being connected to 2 ATD channels.

The third change made to the hardware was the addition of an amplification stage between the current sense resistor and the ATD channel. Due to the small resistance of the current sense resistor (0.03 Ω), the voltage it outputs will also be too small. This would result in a very small SNR that would consequently deteriorate current measurements. Thus, the voltage it outputs was passed through a differential amplifier of a gain = 50 before being input to an ATD channel. The conversion of the voltage output from the current sense resistor to the corresponding current value as well as the computation of the resistance of the SMA wire were again done in software.

The final change made to the hardware was the use of a 26 cm-length SMA wire. This explains the increase in the computed resistance values that will appear in the figures to follow.

Having obtained satisfactory resistance computations, the hardware setup was finalized (schematic diagram shown in Appendix A) including the modifications that were described earlier in this section. Figure 4.25 presents the finalized experimental setup.

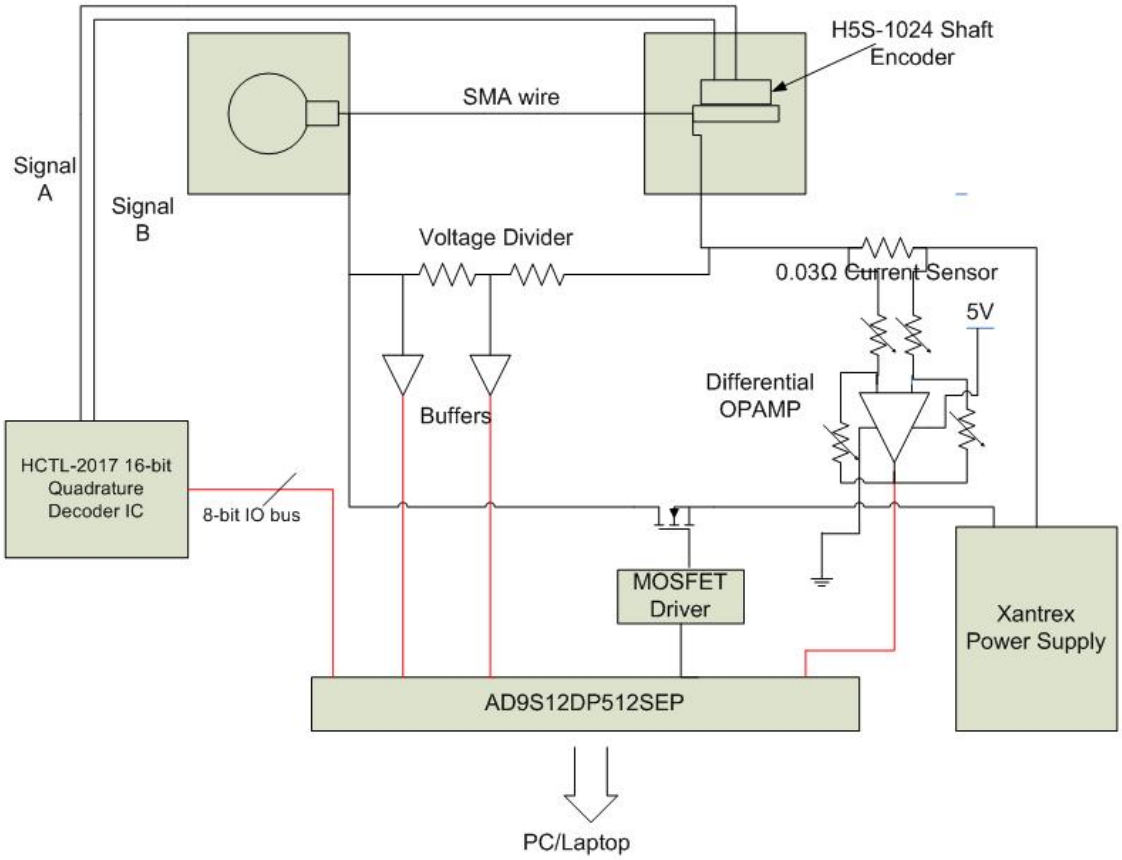

Figure 4.25: New hardware setup

Chapter 5

Priming the SMA wire

As defined in Section 2.3, priming is the process of bringing an SMA element close to a transition point in preparation for actuation and then maintaining it at that point. The work presented in this chapter focuses on the phase transformation associated with heating the SMA wire from M_f to A_s. Consequently, the goal of priming in this work is to pre-heat the SMA wire so that its resistance is close to the cusp resistance that occurs at the onset of actuation. If this goal is achieved, then there is reason to believe that the wire can be actuated in a more consistent period of time regardless of ambient temperature.

However, the important question to answer here is how to determine the current that will prime the SMA, especially since this value will change according to the ambient temperature. For example, at sub-zero temperatures, one would expect that a larger current will be needed to heat the wire, compared to when the wire is at room temperature. This is where the concept of probing the SMA wire comes into effect. *Probing* as defined in this work, is a process of experimentally determining a current level which will bring the wire to the onset of transformation.

5.1 The probing current

The probing current is a slow ramping current that is used to determine the current that causes wire actuation in the present environmental conditions. Since a PWM current driver is used to heat the wire, this current is translated into a duty cycle that is referred to as the maintenance duty cycle (*Mtn_duty*). The important thing to note here is that the probing current does cause some decrease in strain but does not cause the wire to fully actuate, which occurs during the actuation period.

Several methods of detecting the onset of actuation have been proposed in the literature, some of which use a force sensor, a position sensor, a temperature sensor or the resistance of the SMA wire itself. However, in using the resistance, the SMA wire itself is the sensor. Consequently, no external sensor will be required which in turn will reduce cost.

5.2 Modelling SMA wire during actuation

Two of the priming strategies discussed in the next section entail the use of closed-loop feedback controllers. To reduce the time needed in investigating different closed-loop priming strategies and different controller gains, a model of the SMA wire is developed. This model is used to simulate these strategies to tune the controller parameters and predict closed-loop behaviour.

In the literature, several models have been developed by researchers to emulate the behaviour of SMA wires. Examples of these models include the Preisach model [14] and the HEM model [27]. However, implementing these models here will be far too complicated for the purpose of this research for two reasons. First, the model implemented here will only be looking at a one-time, complete actuation. Thus, it will be modelling the major loop of the hysteresis curve upon heating, and not the minor loops nor the effects of partial temperature reversals as in the Preisach and HEM models respectively. Second, the only SMA behaviour that is of interest for the purpose of this research is its behaviour just prior to actuation and as it undergoes actuation, that is, as its resistance increases to the cusp and then as it falls towards its lowest austenite resistance value (see Figure 6.1). Consequently, the model implemented here will depict the resistance-temperature relationship through a single actuation from wire temperature $T < M_f$.

Nevertheless, the model does have a number of deficiencies that need to be acknowledged. Probably the biggest of these deficiencies is the fact that the model does not take into account cooling of the SMA wire. However, since the resistance cusp is taken as a proxy for the A_s temperature at which the wire starts transforming (shown in Figure 2.1), and if it can be assumed that temperature variations around A_s are small enough that the behaviour is considered linear, then for small changes back and forth around the cusp the resistance behaviour can also be considered as linear. Consequently, this deficiency will not affect the model's performance.

5.2.1 Simulation of the SMA wire during actuation

Simulating the SMA wire was divided into two steps:

1. Use a 1st-order convection heat transfer model relating the temperature of the SMA wire to the power supplied to it.
2. Use data collected from experiment to create a lookup table that relates the temperature of the SMA wire (obtained from Step 1) to its resistance during actuation.

The 1st-order convection heat transfer model of an SMA wire is given by Equation 5.1[28]:

$$CV\rho\frac{dT}{dt} = P(t) - hA(T(t) - T_{amb}) \tag{5.1}$$

The variables in Equation 5.1 are defined as follows:

ρ := material density = 6.45x10^3 kg/m^3 [12]
C := specific heat = 465.2 J/(kg°C) [12]
A := wire surface area = 2.07471x10^{-4} m^2
V := wire volume = 1.31744x10^{-8} m^3
h := convection heat transfer coefficient = 95.6 W/(m^2°C) [29]
t := time [s]
T := wire temperature [°C]
P := power consumed by SMA wire (watts)
T_{amb} := ambient temperature [°C]

Defining $\theta(t) = T(t) - T_{amb}$ and taking the Laplace transform of Equation 5.1 yields Equation 5.2.

$$\frac{\theta(s)}{P(s)} = \frac{\frac{1}{CV\rho}}{s + \frac{hA}{CV\rho}} \tag{5.2}$$

Since $\theta(t)$ is the difference between the wire temperature and the ambient temperature, adding T_{amb} to it will yield the wire temperature, T.

As for the lookup table, it was created using resistance values computed during one of the actuation periods from an experimental run. The wire's temperature during that exact same period was computed using the 1st-order heating model in Equation 5.1. A graph of the computed temperature vs resistance values used in creating the lookup table is shown in Figure 5.1.

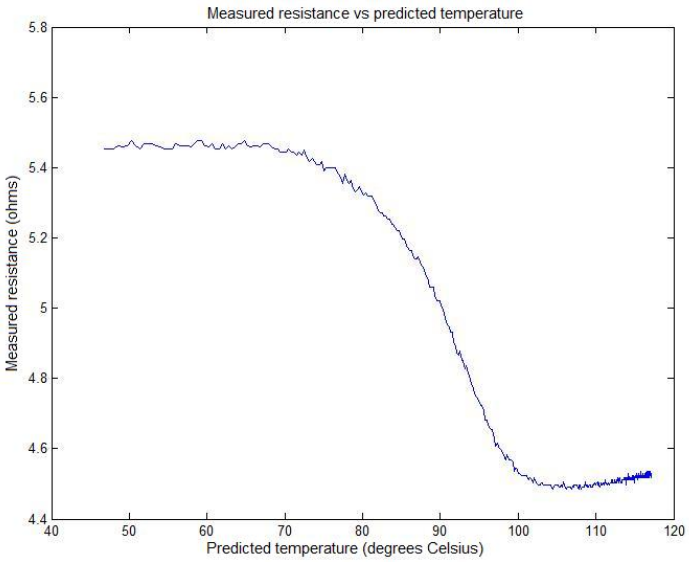

Figure 5.1: Lookup table created using experimental data and heating model

Looking at Figure 5.1, one notices that the resistance of the SMA wire does not seem to increase to a cusp before it actuates. As a matter of fact, the resistance of the SMA wire seems to be somewhat uniform prior to actuation. This can be attributed to the already noisy resistance values obtained from the experiments. Thus, in an attempt to create a lookup table that more accurately resembles the resistance of the SMA wire at different temperatures, a new simulation was conducted where the duty cycle of the PWM current signal used to heat the wire was ramped up from 0% to 10% and then back down to 0%. The highest duty cycle was set to 10% because it was found, from previous experiments, to be large enough to actuate the SMA wire at room temperature without overheating it. The power supplied to the SMA wire during this experiment was computed using the collected voltage and current samples and then fed to the 1st-order heating model in Simulink to compute the wire's temperature. The computed resistance values and their corresponding temperatures were then used to generate the new lookup table.

In determining the rate at which the PWM duty cycle should be ramped, it was important to calculate the time constant of the SMA wire from the 1st-order

heating model. This served to maintain the PWM duty cycle at a fixed value for a sufficient period of time to ensure that the wire has reached a steady-state temperature at which the resistance can be recorded. For any transfer function, the time constant can be computed if arranged in the form of Equation 5.3.

$$F(s) = \frac{K}{1 + s\tau} \tag{5.3}$$

Arranging Equation 5.1 in the form of Equation 5.3 yields Equation 5.4.

$$\frac{\theta(s)}{P(s)} = \frac{\frac{1}{hA}}{\frac{CV\rho}{hA}s + 1} \tag{5.4}$$

As a result, the time constant of the SMA wire is $\tau = \frac{CV\rho}{hA} \approx 1.993\,\text{s}$. Thus, setting the time duration for which a duty cycle is maintained constant to $4\tau \approx 8\,\text{s}$ (the time needed for the temperature to reach 98% of its steady-state value), the duty cycle was ramped at a rate of 0.5% for every 8 s.

The duty cycle profile used in the experiment is shown in Figure 5.2 while the computed resistance values are shown in Figure 5.3.

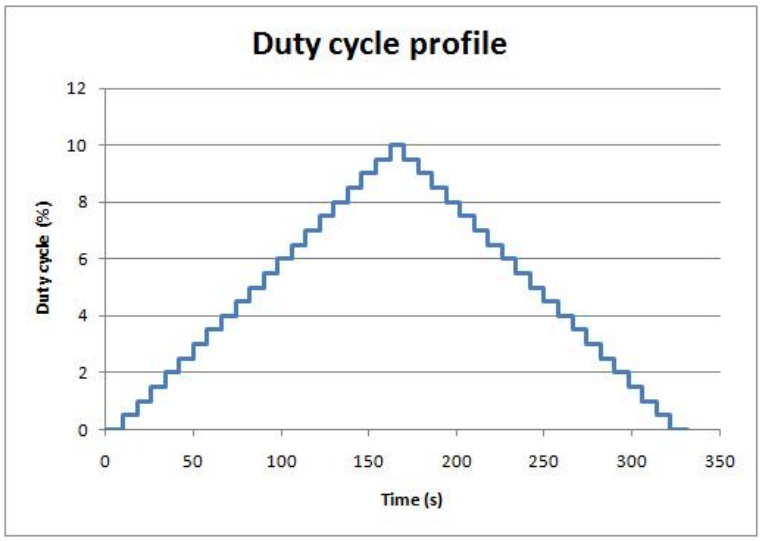

Figure 5.2: Duty cycle profile during experiment

Although it is not possible to compute the resistance of the SMA wire at 0% duty cycle because the current flowing through the SMA wire will also be 0, the analysis

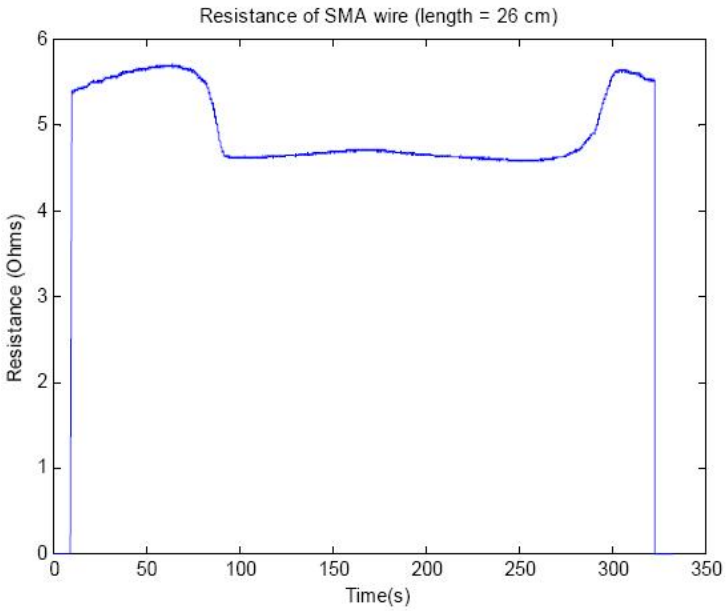

Figure 5.3: Computed resistance of SMA wire as duty cycle is ramped up and down

code was modified to set the resistance of the SMA wire to 0 when the current is 0 A.

As can be seen from Figure 5.3, the resistance of the SMA wire increases to a cusp at about 65 s and then drops to a lower austenite resistance value as the duty cycle is ramped up. As the duty cycle is decreased, the SMA wire starts cooling down. At around t = 280 s, the resistance of the SMA wire increases to its martensite resistance value ($\approx 5.6\,\Omega$) The resistance computations between 30 & 110 s were taken to construct the new lookup table. The power supplied during that same interval (computed by multiplying the corresponding voltage and current samples) was fed to the 1st-order heating model to yield the corresponding temperatures of the wire. The experimentally computed resistance values and their corresponding temperatures output from the heating model are depicted by the green curve in Figure 5.4.

Since the green curve is a little noisy, a polynomial was fitted through the experimental resistance computations to obtain a smoother curve using the **polyfit** and **polyval** functions in MATLAB. The blue curve in Figure 5.4 represents a 5th-order polynomial that was fitted through these resistance values. However, simulations with the polynomial fit produced non-physical behaviour due to the initial negative slope of the curve at low temperatures. Therefore, the next option was to filter the computed resistance values using a **zero-lag low-pass filter**. A zero-lag filter filters the input data in both the forward and backward directions.

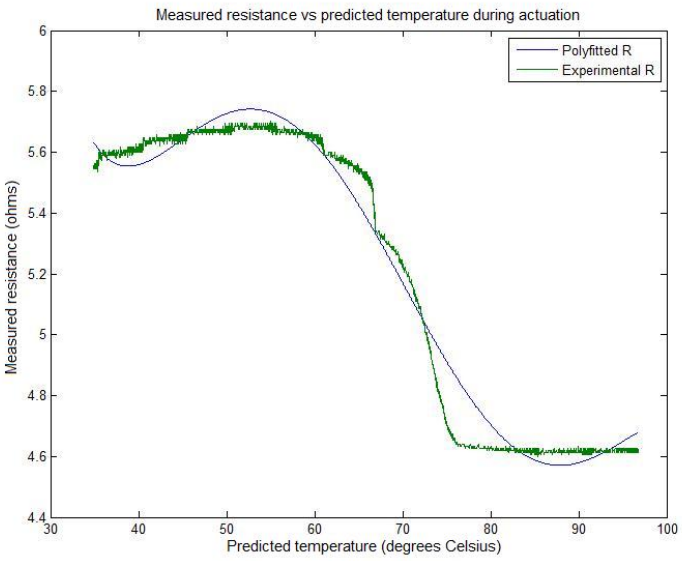

Figure 5.4: Temperature vs polynomial-fitted and actual resistance values

This means that after filtering in the forward direction, the filtered data is reversed and fed back through the filter yielding a data sequence with exactly zero phase distortion. This is ideal for use with offline data which is exactly the case with the lookup table.

The computed resistance values used to create the lookup table were filtered using the **filtfilt** command in MATLAB. The filtered resistance values are depicted in Figure 5.5.

Looking at Figure 5.6, one observes that the zero-lag filtered data better matches the experimental data compared to the polynomial-fitted curve shown in Figure 5.4. It was this filtered resistance data and its associated temperature that was ultimately used to construct the lookup table.

5.2.2 Priming controller design

The priming controller design implemented in the *Peak Detector 1* strategy consists of two modules:

1. A peak detector module that attempts to detect the cusp in the resistance during actuation and,

2. A Bang-Bang controller that is activated once the peak has been detected and drives the SMA wire with either a large current (for heating) or a low current

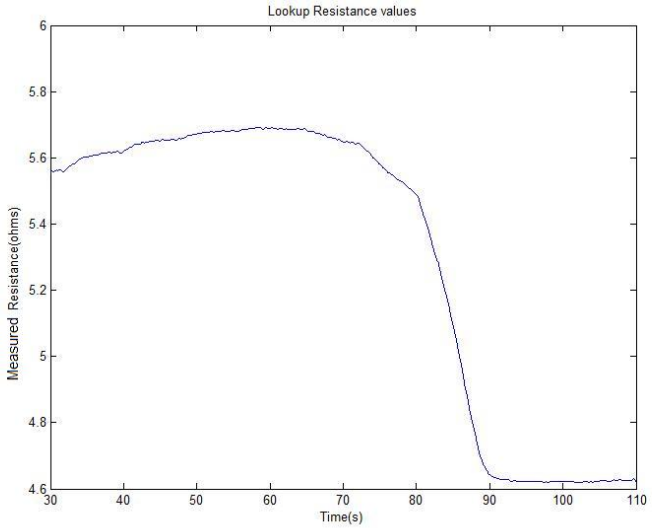

Figure 5.5: Experimental R values filtered using a zero-lag low-pass filter

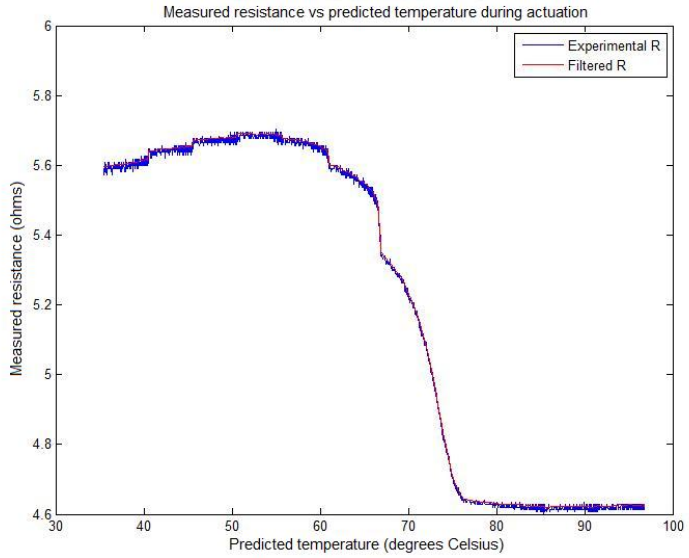

Figure 5.6: Filtered R and Experimental R vs temperature

(for cooling). The reason behind using a small current value as opposed to 0 A is to enable voltage and current measurements to be taken periodically so that the feedback resistance can be calculated for the controller.

The purpose of the peak detector is to detect the cusp in the resistance of the SMA wire that exists prior to actuation. It does so by comparing the present resistance value with the previous two values. If the present resistance value and the one computed in the previous sample are both less than that computed two samples ago, then a peak has been detected. Another way to explain the cusp detection methodology is using the expressions in Equation5.5:

Cusp is detected if:

$$r[k] - r[k-2] < 0 \; AND \; r[k-1] - r[k-2] < 0 \tag{5.5}$$

where r is the computed resistance and k represents the current sample (voltage and current) used to compute this resistance.

The peak detector also specifies whether the present resistance value is on the negative slope of the cusp or on the positive slope. For example, in Figure 5.7, *R1* is on the positive slope of the resistance curve as it increases towards the cusp. In this case, we say that a peak has been detected in the *positive direction*. On the other hand, *R2* is on the negative slope of the resistance curve and we say that a peak has been detected in the *negative direction*.

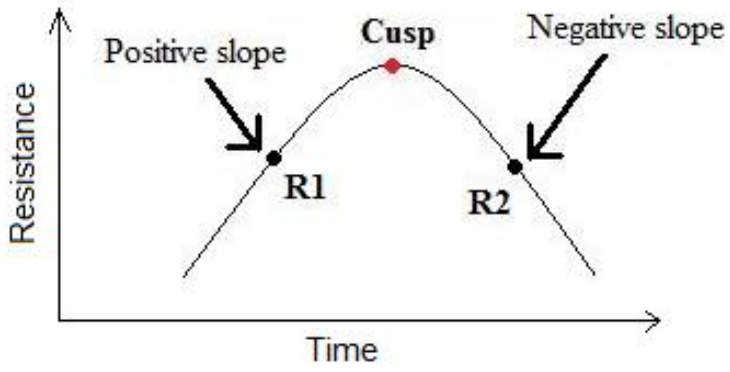

Figure 5.7: Peak detector determines which slope of the cusp current resistance value is on

However, the part of the peak detector logic concerned with comparing resistance values in contiguous samples to detect the existence of a peak is employed

only once. This comparison is carried out until the first occurrence of the cusp is detected, after which the peak detector only specifies which slope of the cusp the present resistance value is on and the Bang-Bang controller is activated. This approach makes sense given the fact that, when the wire is first heated at the very beginning of the experiment, its resistance is well to the left of the peak. As it gets heated, its resistance increases until the peak is passed.

As for the Bang-Bang controller, the current value it outputs depends on 3 factors:

1. The sign of the error between the current resistance measurement and the previous resistance value.

2. The slope on which the current and previous computed resistance values lie i.e. whether both resistance values are on the positive slope towards the cusp, on the negative slope away from the cusp or on opposite sides of the cusp (see Figure 5.8).

3. The last action taken (heating or cooling).

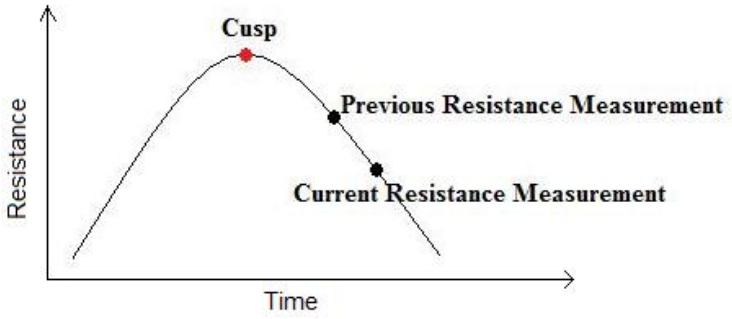

Figure 5.8: The slope on which the current and previous resistance values lie is one of the factors that determine the output of the Bang-Bang controller

Given the initial conditions that resistance measurements (current and previous) are to the right of the peak, that the wire has previously been heated and that both the current and previous computed resistance values are less than the resistance value computed two samples ago, the decision to either heat or cool in any given sample is subject to the following conditions:

- **IF** (Current R < Previous R) *AND* (Right of Peak Detected) *AND* (Previously Cooling) **THEN** (HEAT) *AND* (Left of Peak Detected)

- **ELSE IF** (Current R < Previous R) *AND* (Left of Peak Detected) *AND* (Previously Heating) **THEN** (COOL) *AND* (Right of Peak Detected)
- **ELSE IF** (Right of Peak Detected) **THEN** (COOL)
- **ELSE IF** (Left of Peak Detected) **THEN** (HEAT)

Since the only behaviour of the SMA wire that is of interest is its behaviour during the priming period, and since the *Peak Detector* strategies entail ramping up the duty cycle at the beginning of priming, a constant current of 2 A, a constant voltage of 12 V and a ramp signal representing the ramping of the PWM duty cycle were used as input signals to the model. They are multiplied together to yield power, which is simulated in the first-order heating model to estimate wire temperature. For the simulation, the duty cycle is ramped at a rate of 0.5%/s, starting at 0 A for 80 s. Note that, since this is simulation, there is no knowledge of the *Mtn_duty* which is determined in the probing segment of the actual experiment. Thus, the peak detector comes into effect as soon as ramping of the current begins to detect the cusp. Once this peak has been detected, the Bang-Bang controller is activated and attempts to maintain the resistance at the peak value.

5.3 Priming strategies

Several experiments were conducted using 4 different priming strategies, which were labelled *50%*Mtn_duty*, *Minus 4.5%*, *Peak Detector 1*, and *Peak Detector 2*. The goal of priming is to get the wire into a consistent state prior to actuation under different temperatures. This consistent state is the resistance cusp that naturally occurs at the onset of actuation. Since the cusp is essentially identified with the value of the current that results from setting the PWM duty cycle to *Mtn_duty*, the priming strategies are based on this duty cycle. The duty cycle during the priming period is called *Priming_duty*. The first two strategies, *50%*Mtn_duty* and *Minus 4.5%*, are open-loop strategies. They are also purely heuristic, based on observations from running experiments under different temperatures. The third and fourth strategies, *Peak Detector 1* and *Peak Detector 2*, are closed-loop and build upon the first two by including a peak detector to detect the cusp on the resistance. However, they differ in that the former uses a Bang-Bang controller in conjunction with the peak detector while the latter employs a proportional controller.

5.3.1 50%*Mtn_duty

In the *50%*Mtn_duty* strategy, the SMA wire is primed by applying a duty cycle equal to 50% of the maintenance duty cycle, *Mtn_duty* determined during probing. It follows from a similar priming strategy that was used in [7]. In [7], where continuous rather than PWM currents were used, it was found that, at low air flow conditions, applying a priming current that was equal to 50% of the maintenance current helped prime the wire without the risk of spurious actuation.

5.3.2 Minus 4.5%

Since the purpose of probing is to find the duty cycle (*Mtn_duty*) at which the SMA wire starts to actuate but does not undergo full actuation, using a priming duty cycle, *Priming_duty*, that is very close to but still less than *Mtn_duty* during priming seemed like a plausible priming strategy as surely, the wire will not undergo spurious actuation at this lower duty cycle. Moreover, it is hoped that this lower duty cycle will drive the resistance of the SMA wire close to the resistance cusp that exists at the onset of actuation. In fact, if the wire is probed not so long before priming takes place, and if it can be assumed that the ambient temperature does not change considerably throughout the duration of the experiment, one could expect this priming strategy to be very effective across a whole range of temperatures. This is because the applied duty cycle would vary according to the *Mtn_duty* determined at each temperature. Consequently, it would maintain the resistance close to the cusp and not drive the wire into spurious actuation.

An experiment was first conducted with *Priming_duty* = *Mtn_duty* - 1%. Note that this 1% is an absolute value and not a relative value with regard to *Mtn_duty*. For example, if *Mtn_duty* = 10%, then *Priming_duty* = 9% and **not** *Priming_duty* = 10% - 0.01 $\times$ 10%. However, it was found that the SMA wire underwent spurious actuation during priming. Therefore, several experiments were conducted at room temperature with different duty cycles until it was found that by setting *Priming_duty* = *Mtn_duty* - 4.5%, the wire did not undergo spurious actuation and also the resistance of the SMA wire during priming was very close to the cusp.

5.3.3 Peak Detector 1

The *Peak Detector 1* priming strategy was devised in case the assumption taken in the *Minus 4.5%* strategy that the ambient temperature remains more or less

constant for the time between probing and priming does not hold. The main idea behind *Peak Detector 1* is to servo around the cusp where the theoretical value of dR/dt is 0. However, $dR/dt = 0$ at any value of R provided that the current is constant and not high enough to cause actuation. Therefore, to overcome this problem, the duty cycle of the PWM signal was first ramped to raise the temperature of this wire to the point where its resistance reaches the cusp, and *then* the servo controller was turned on.

In this priming strategy, the duty cycle of the PWM signal is first ramped at the beginning of the priming period to a maximum duty cycle equal to $0.8*Mtn\_duty$. This condition was introduced to avoid detection of zero gradients in the resistance curve which may exist at low duty cycles due to the noise on the collected samples and also, to start peak detection at a point that is close enough to where the cusp will exist. A peak detector is then used to detect the cusp in the resistance. As mentioned earlier, this cusp is considered to have been detected when the computed resistance values continue to decrease over three consecutive samples. When this point is reached, a Bang-Bang controller is initialized that attempts to maintain the resistance at the cusp by outputting either a small duty cycle (cooling) or a large duty cycle (heating). Note that the small duty cycle cannot be 0% since in this case the voltage across the wire and the current flowing through it will also be 0 and computing the resistance would be impractical.

5.3.4 Peak Detector 2

The *Peak Detector 2* strategy is exactly the same as the *Peak Detector 1* strategy except that a proportional controller is used rather than a Bang-Bang controller to maintain the resistance at the cusp. However, this strategy was only tested in simulation and not on the actual hardware as the results it yielded were similar those of the *Peak Detector 1* strategy.

After several trials, the value of K_p that gave the best performance in terms of maintaining the resistance near the cusp was found to be 10.

5.3.5 Test cases

In determining the two duty cycle values ($Duty_{high}$ and $Duty_{low}$) between which the output of the Bang-Bang controller (in *Peak Detector 1* priming strategy) will alternate, care had to be taken to ensure that the higher duty cycle, $Duty_{high}$, was

neither too low to maintain the resistance of the SMA wire close to the cusp, nor was it too high which may result in spurious actuation. Thus, 4 different test cases were conducted in simulation with different duty cycle outputs for the Bang-Bang controller to investigate which values yield the best results. There are several things to note in these simulations. First, in the actual experiments, the instantaneous current flowing through the SMA wire was on average approximately equal to 2 A. Thus, a constant current equal to 2 A is used in the simulation to calculate the power input to the first-order heating model. Second, these simulations run for 80 s, 50 s longer than the priming segment in the actual experimental run. This is to show that, under the *Peak Detector* strategies, the SMA wire will not undergo spurious actuation. Finally, the ambient temperature, T_{amb}, in these simulations is set to 20 °C to simulate room temperature.

Moreover, several simulations were run simulating different ambient temperatures to investigate the two duty cycle values of the Bang-Bang controller that will yield the best performance. Indeed, different controller limits performed better at different temperatures. However, since the the controller limits of the Bang-Bang priming controller will not vary in the actual experimental runs, and since all the priming strategies (including the heuristic ones) were developed according to observations made at room temperature, the simulation at an ambient temperature of 20 °C was used to determine the controller limits for the actual control experiments.

Test Case 1 ($Duty_{low} = 2\%, Duty_{high} = 5\%$)

When running the actual experiment under room temperature, the *Mtn_duty* was found to be around 5%. Thus, $Duty_{high}$ was set to 5%. As for $Duty_{low}$, the minimum duty cycle the microcontroller was programmed to generate was initially set to 2%.Therefore, for this test case, $Duty_{low}$ was set to 2%. The simulated temperature and resistance of the SMA wire model for Test Case 1 are depicted in Figures 5.9 and 5.10 respectively.

Test Case 2 ($Duty_{low} = 2\%, Duty_{high} = 10\%$)

By definition, *Mtn_duty* refers to the duty cycle that will cause the SMA wire to begin contracting under the present environmental conditions. Thus, one would expect that if a larger duty cycle is used to heat the SMA wire, the wire will undergo full actuation. Therefore, in this test case, $Duty_{high}$ was set to 10% to investigate the effect of applying a duty cycle larger than *Mtn_duty* on the simulated resistance

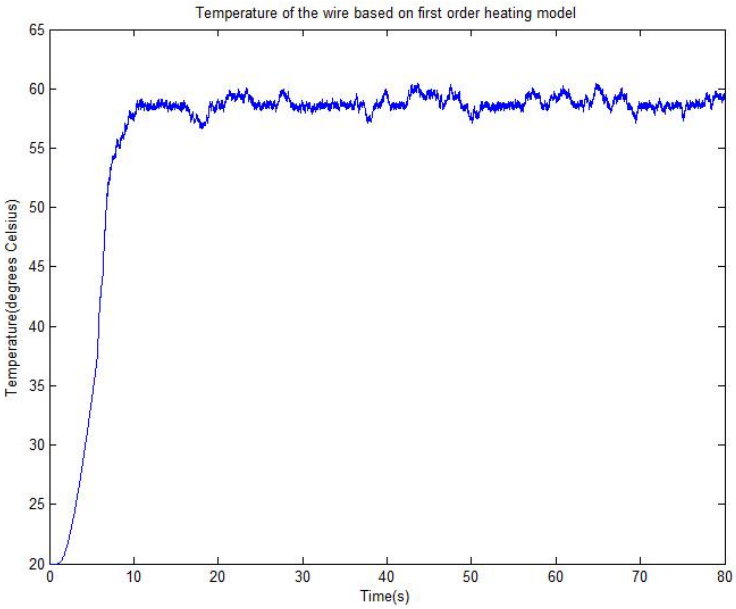

Figure 5.9: Temperature of SMA wire in Test Case 1

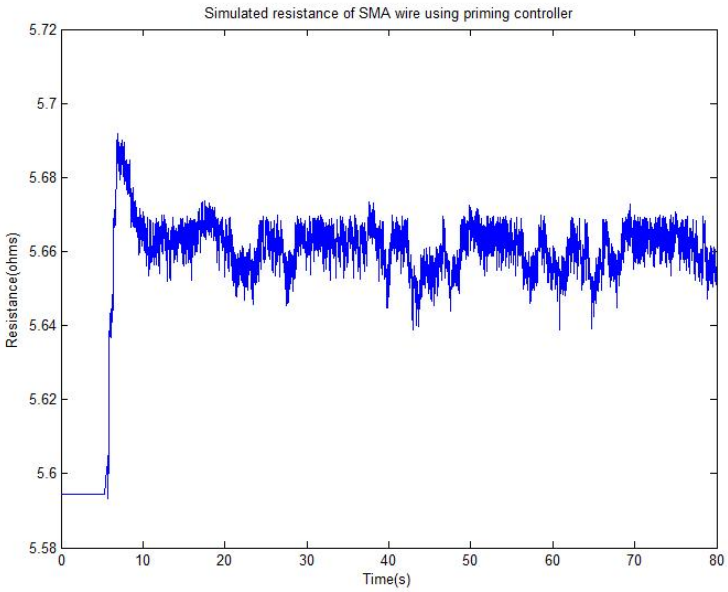

Figure 5.10: Resistance of SMA wire in Test Case 1

of the SMA wire. The simulated temperature and resistance of the SMA wire model for Test Case 2 are shown in Figures 5.11 and 5.12 respectively.

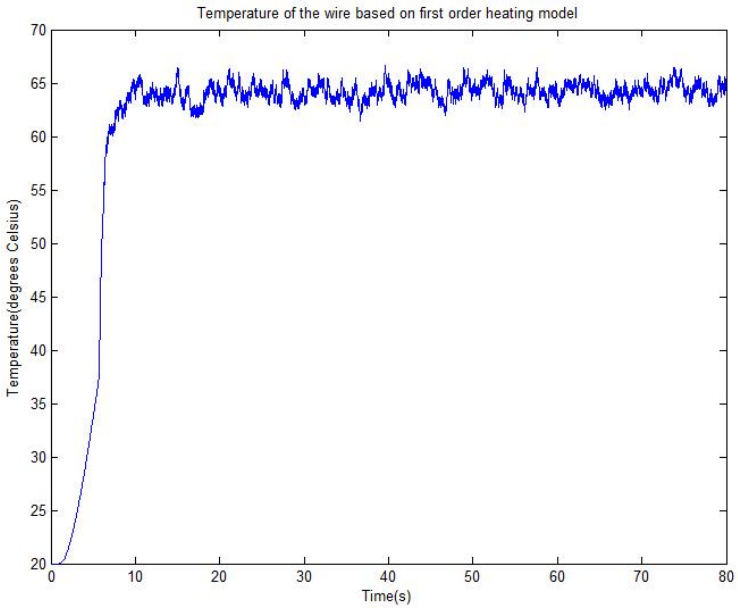

Figure 5.11: Temperature of SMA wire in Test Case 2

Test Case 3 ($Duty_{low} = 0\%, Duty_{high} = 5\%$)

Since an SMA wire cannot be actively cooled, the fastest way to cool it would be to pass 0 A through it. Hence, in this test case, $Duty_{low}$ was set to 0% and $Duty_{high}$ to 5%. The simulated temperature and resistance of the SMA wire model for Test Case 3 are shown in Figures 5.13 and 5.14 respectively.

Test Case 4 ($Duty_{low} = 0.5\%, Duty_{high} = 5\%$)

With the hardware setup, it will be impractical to set the duty cycle to 0% (i.e. current = 0 A) as it will no longer be possible to compute the resistance. On the other hand, after replacing the Hall effect sensor with the current sense resistor and dropping the implementation of the noise filtering techniques, it was found that the minimum duty cycle could be further reduced from 2% to 0.5% (which is also the minimum duty cycle that can be set using the PWM module on the microcontroller). This will not conflict with the sampling strategy of taking a sample 20 μs after the falling edge of the PWM signal as the 0.5% duty cycle will yield an off-pulse duration of 100 μs. Consequently, for this test case, $Duty_{low} =$

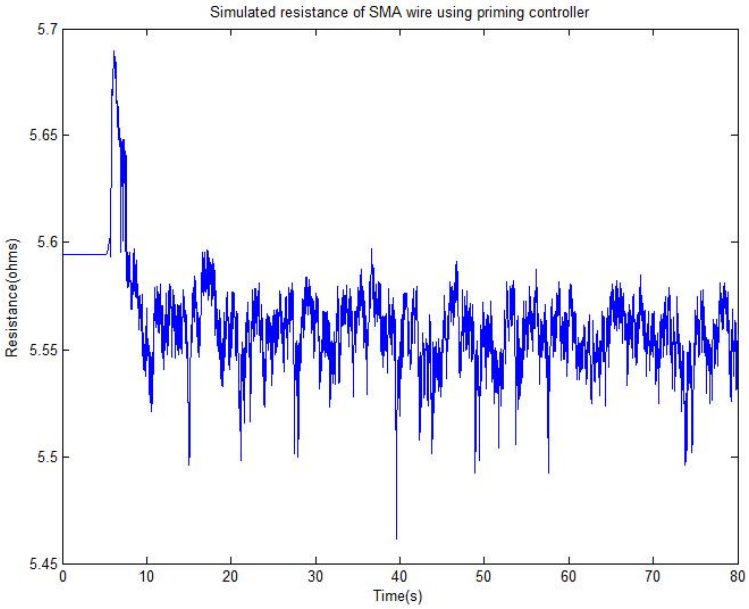

Figure 5.12: Resistance of SMA wire in Test Case 2

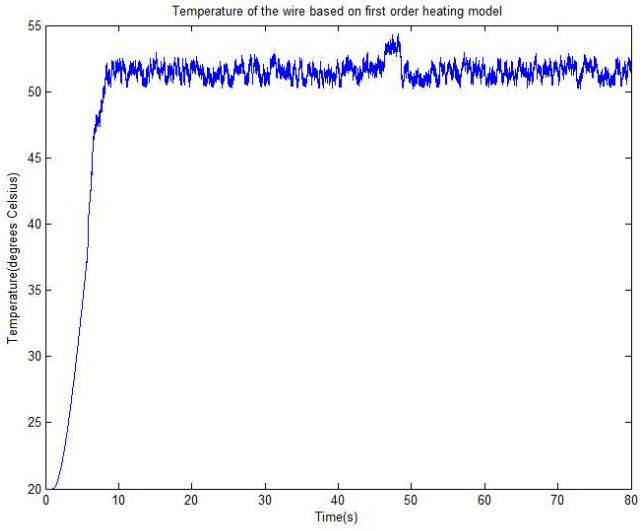

Figure 5.13: Temperature of SMA wire in Test Case 3

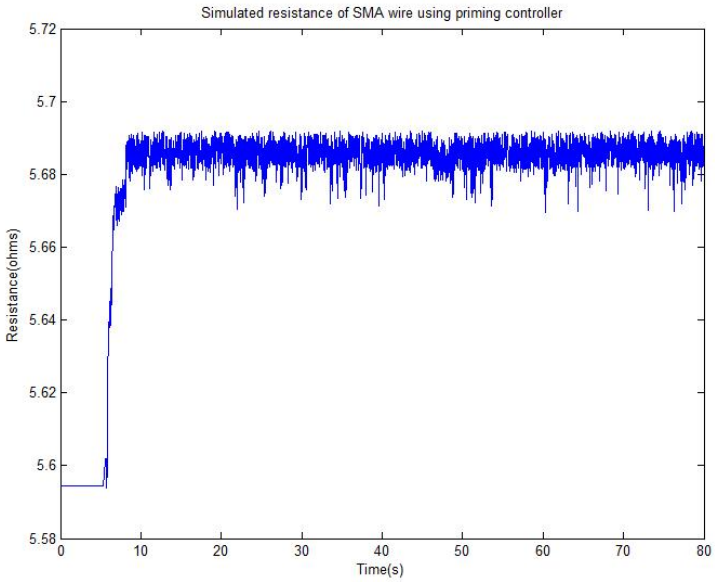

Figure 5.14: Resistance of SMA wire in Test Case 3

0.5% and $Duty_{high} = 5\%$. The simulated temperature and resistance graphs are shown in Figures 5.15 and 5.16 respectively.

Looking at Figure 5.15, the simulated temperature of the SMA wire between 15-25 s, 45-50 s, and 58-65 s, is 3-4 °C higher than the wire temperature elsewhere. This should not be the case as the purpose of the priming period is to maintain the wire temperature at approximately a constant value. However, looking at the MATLAB .mat files, one will find that the average simulated power supplied to the wire during those periods is larger than the average power supplied during any other period. Hence, the wire temperature is higher. However, this temperature difference is not significant enough to cause a drop in the wire resistance as the graph in Figure 5.10 is fairly uniform.

Comparing results

In Test Case 1, the simulated resistance of the SMA wire (shown in Figure 5.10) was maintained at around 5.66 Ω for the duration of the simulation. When $Duty_{high}$ was increased to 10% in Test Case 2, the resistance was maintained at a lower resistance value of 5.55 Ω (Figure 5.12). This lower resistance value is actually an indication that the wire has actuated especially that $Duty_{high}$ was set to a value larger than the *Mtn_duty*. In Test Case 3, the resistance was maintained at ≈ 5.68 Ω, very close to the cusp value of about 5.69 Ω (Figure 5.14). The same applies to Test Case 4 (Figure 5.16).

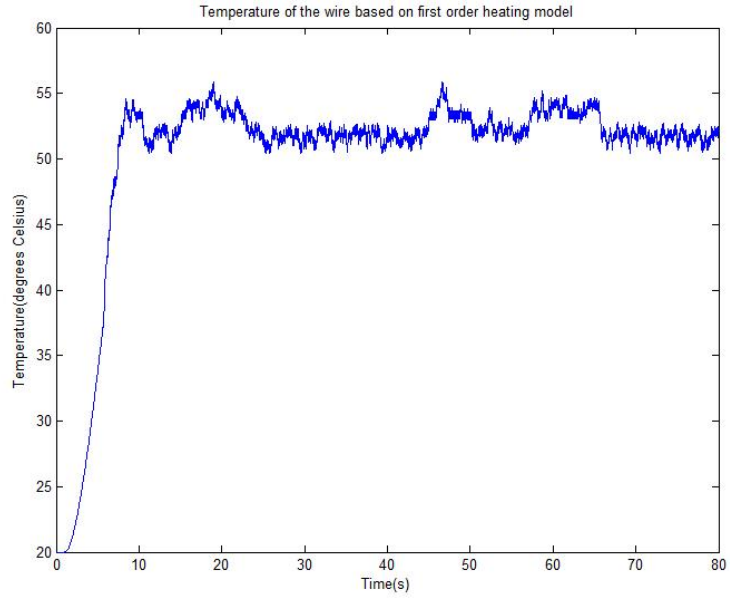

Figure 5.15: Temperature of SMA wire in Test Case 4

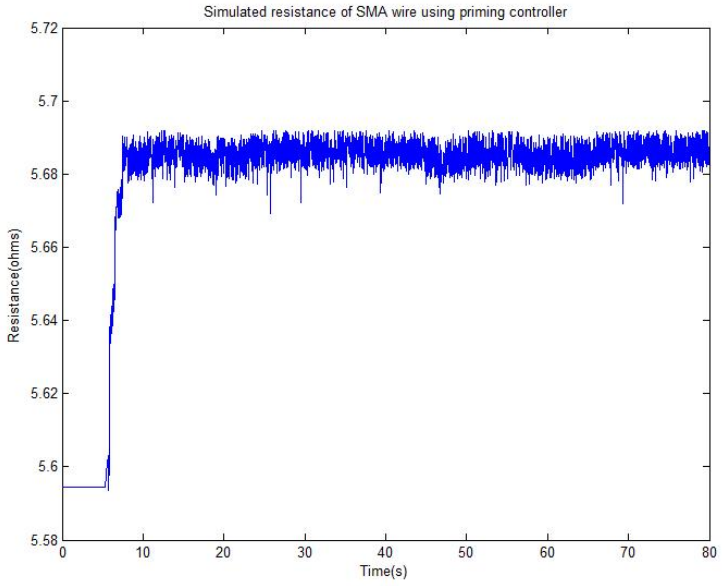

Figure 5.16: Resistance of SMA wire in Test Case 4

Comparing the results from the four different test cases, one observes that the best performance, in terms of maintaining the resistance of the SMA wire closest to the cusp value, was obtained in Test Cases 3 and 4. However, the minimum duty cycle of 0% (i.e. current = 0 A) cannot be implemented in the actual experimental setup as it will prevent resistance computation. Thus, one finds that setting the Bang-Bang controller such that its output alternates between 0.5% and 5% to be more practical. Thus, for the actual experiment, the high and low duty cycles between which the output of the Bang-Bang controller alternates in the *Peak Detector 1* strategy were fixed to *Mtn_duty* and 0.5% respectively.

5.3.6 Peak Detector 2 simulation results

As mentioned earlier, the *Peak Detector 2* strategy used a proportional controller to maintain the resistance close to the cusp. To be able to compare the performance of *Peak Detector 2* with that of *Peak Detector 1*, the duty cycle that can be generated by the proportional controller is limited to values between 0.5% and 5%. In other words, if the proportional controller generates a duty cycle that is less than 0.5%, then a duty cycle of 0.5% is used to compute power. On the other hand, if it generates a duty cycle larger than 5%, then output is saturated at 5%. These limits were chosen based on the fact that 0.5% is the minimum duty cycle that can be generated by the actual microcontroller whereas 5% was the maintenance duty cycle, *Mtn_duty*, determined in the experimental run whose data was used to construct the wire model.

Several simulations were run with different K_p values to determine which will yield the best performance in terms of maintaining the resistance of the SMA wire close to its cusp. Setting $K_p = 10$ gave the best results. The simulated temperature and resistance of the SMA wire are shown in Figures 5.17 and 5.18 respectively.

As can be seen in Figures 5.17 and 5.18, the *Peak Detector 2* maintained the simulated temperature of the SMA wire at $\approx 52\,^{\circ}\mathrm{C}$. It was also successful at maintaining the simulated resistance of the SMA wire at $\approx 5.68\,\Omega$ which is very close to the cusp. Moreover, these results are very similar to those obtained in Test Cases 3 and 4 above.

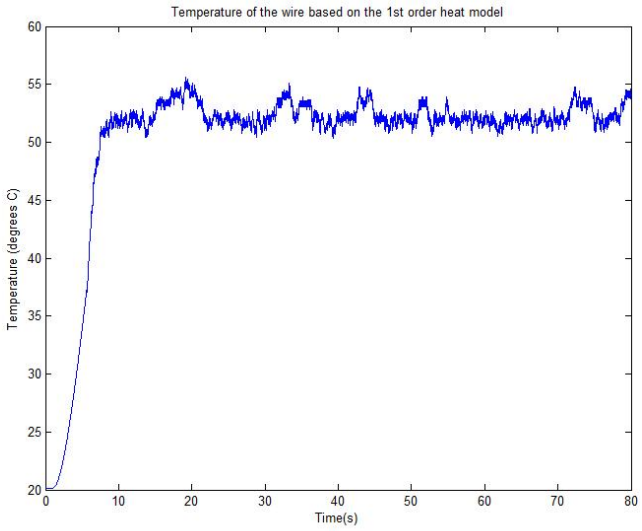

Figure 5.17: Simulated temperature of SMA wire using *Peak Detector 2* strategy

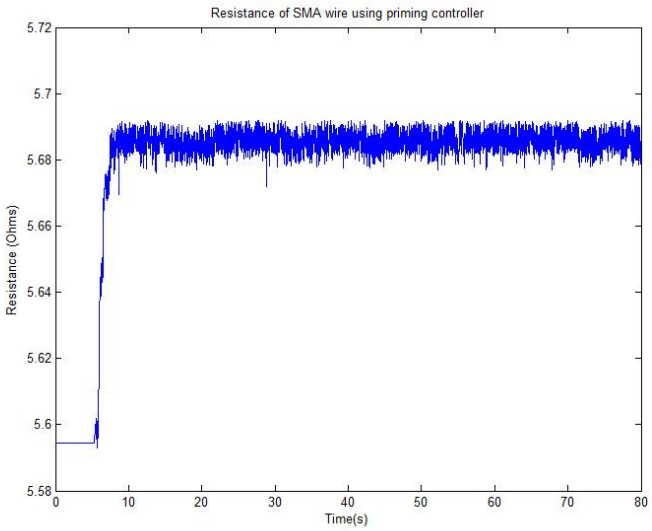

Figure 5.18: Simulated resistance of SMA wire using *Peak Detector 2* strategy

Chapter 6

Experimental results and discussion

This chapter presents the results of experimental testing which compares the effectiveness of priming using the different priming strategies described in Chapter 5. The experimental protocol carried out is discussed first, followed by the comparison strategies and metrics that were used to evaluate the performance of the four priming strategies. The single actuation strategy that was implemented in all experiments is also be explained. Finally, the test results obtained from experimenting with the different priming strategies are presented. At each ambient temperature, a set of five experiments, each employing one of the priming strategies, was conducted. This set of experiments was carried out at five different ambient temperatures: $-30\,^{\circ}\mathrm{C}$, $-15\,^{\circ}\mathrm{C}$, $0\,^{\circ}\mathrm{C}$, $20\,^{\circ}\mathrm{C}$ (room temperature) and $40\,^{\circ}\mathrm{C}$.

6.1 Test procedure

Since the current required to actuate an SMA wire is dependent on ambient conditions, applying a fixed current may cause overheating and damage in high ambient temperatures, or could fail to actuate the wire entirely in low ambient temperatures. As such, a method is required to determine an appropriate current profile which will actuate the wire without danger of overheating. Given that the only feedback variable is R, the behaviour of R during actuation was examined. As shown in Figure 6.1, R increases until it reaches a cusp and starts decreasing as the wire actuates.

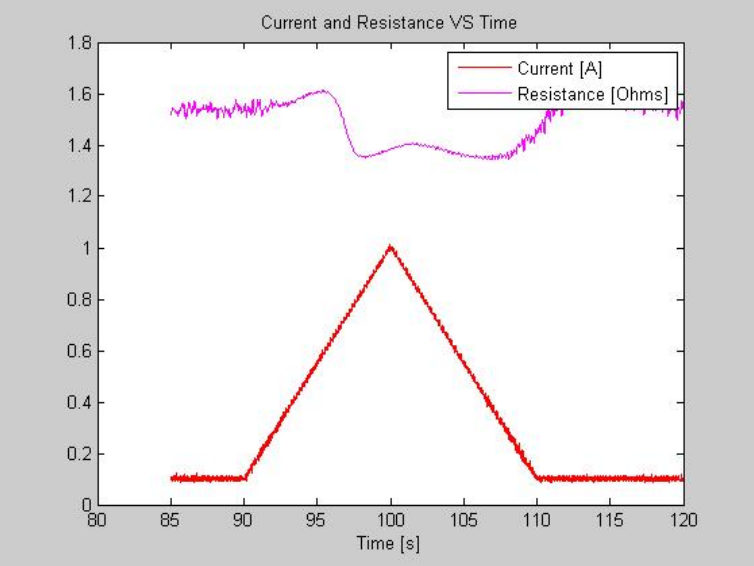

Figure 6.1: Current and resistance vs time for SMA wire

6.1.1 Experimental segments

All the experiments used the same timing sequence, initialization procedure, actuation controller and ending procedure. They only differed in either the priming strategy implemented or the ambient temperature at which the experiment was conducted. An example of an experimental trial is shown in Figure 6.2. The labelled sections of Figure 6.2 from 1 to 6 are the initialization, probing, cooling, priming, actuation, and ending periods respectively. The cooling, priming, and actuation periods are repeated two more times to give three full actuation cycles per trial run in order to judge consistency of the response. Note that the red plot in Figure 6.2 represents the effective current flowing through the SMA wire during the experiment and not the instantaneous current samples. This effective current is obtained by multiplying the instantaneous current values by the square root of the PWM duty cycle applied at that sample.

In the initialization period (labelled 1 in Figure 6.2), the wire is first heated to contract it to its austenite length (for the given fixed stress of 178 MPa). Then, the PWM duty cycle is set to 0.5% allowing the wire to cool. The wire is then actuated once more and left to cool to ensure that the wire expands to its maximum strain (again, for the given fixed stress of 178 MPa). The initialization period lasts 50 s. Note that the encoder is zeroed as soon as it is initialized once the experiment begins.

In the probing period (labelled 2 in Figure 6.2), the wire is allowed to cool for

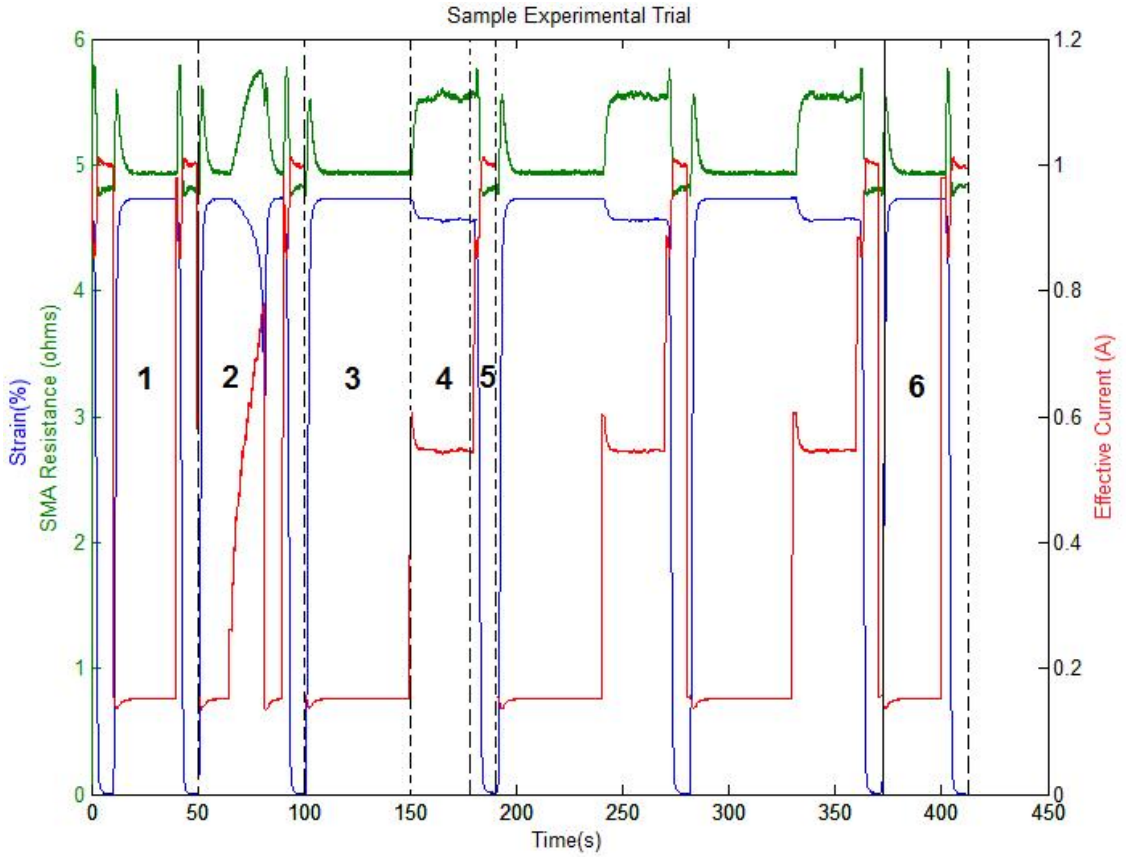

Figure 6.2: Segments of experiment

10 s before the probing current is used to find *Mtn_duty*. The duty cycle is ramped at a rate of 1 %/s. Ramping stops when 70% of the resistance values computed from the voltage and current samples collected duting a 1 s interval are decreasing, indicating that the SMA wire is beginning to actuate. The duty cycle at which this happens is *Mtn_duty*. Since the probing current causes the wire to contract, the wire is actuated again at the end of the probing period to return the wire to a consistent state. The probing period also lasts 50 s.

In the cooling period (labelled 3 in Figure 6.2), the duty cycle is reduced to 0.5% and the wire is allowed to cool for 50 s, during which it stretches again and reaches a constant maximum length.

In the priming period (labelled 4 in Figure 6.2), the various priming techniques are implemented. The priming periods last 30 s to confirm that spurious actuation does not occur during priming.

In the actuation period (labelled 5 in Figure 6.2), the actuation strategy is implemented. All the tests used the same actuation strategy where the duty cycle used to actuate the wire was set to 150% * *Mtn_duty*. The actuation period lasts 10 s to show that the actuation can be held. Note that between 190 s-370 s, segments 3-5 are repeated so that the average of the comparison metrics (defined later) can be taken.

In the ending period (labelled 6 in Figure 6.2), the wire is actuated one last time to bring it back to its austenite length giving it a consistent start state for the next experiment.

6.2 Experimental protocol

Before running experiments at a certain temperature, the temperature controller on the temperature-controlled chamber is first set to this temperature. The controller is then left to operate until the thermocouple measuring the temperature of the experimental jig holding the SMA wire reads the desired temperature. This is to ensure that the environment inside the refrigerator (air and hardware) has reached a steady state temperature.

The first experiment conducted at any temperature is that implementing the *Safe Duty* priming strategy. As a matter of fact, this experiment is run several times to determine the minimum duty cycle that will cause the SMA wire to achieve maximum contraction at this specific temperature. This minimum duty cycle is

determined as the duty cycle at which one observes a "plateau" or constant value for the displacement of the SMA wire that lasts for a few seconds during the actuation period of an experiment. An example of this plateau is shown in Figure 6.3. Note that applying a duty cycle larger than this minimum will not result in a larger displacement but will only increase the temperature of the SMA and consequently increase the risk of damaging it.

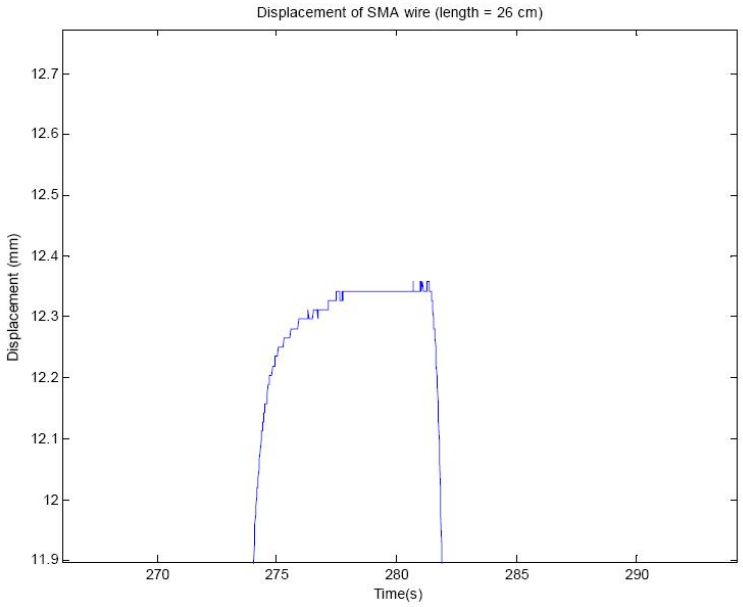

Figure 6.3: "Plateau" observed in displacement curve during actuation

Once the minimum duty cycle needed to actuate an SMA wire at a certain temperature has been determined, the other experiments with the different priming strategies are carried out. An experiment runs for approximately 7 minutes. Once the experiment is over, a small piece of code is run to dump the contents of the external EEPROM memory onto the MiniIDE software on the PC. This data is then copied into MATLAB for analysis e.g. to compute the resistance of the SMA wire from the collected voltage and current samples. Another piece of code is then run to delete the contents of the EEPROM for the next experimental run.

6.3 Comparison strategies

To study whether priming does in fact help with achieving robust actuation of the SMA wire and to evaluate the performance of the priming strategies introduced earlier, two strategies were used as benchmarks against which all results were compared. These strategies are called *Safe Duty* and *No Priming*.

These two comparison strategies are similar in that neither implement any priming strategy during the priming segments of the experiments. During the priming segments of both strategies, the PWM current duty cycle is set to 0.5%, the lowest duty cycle that the PWM module on the microcontroller can generate, in order to allow continued monitoring of the wire resistance. This is done so that a resistance can be measured since power needs to flow to measure a voltage drop across the SMA wire and a current flowing through it. On the other hand, they only differ in the actuation strategy they implement as will be described in the following sections.

6.3.1 Safe Duty

The manufacturer-recommended safe current for the 250 μm diameter SMA wire used in these experiments is 1A [12]. However, this current is specified at room temperature in still air. In [6], Featherstone and Yee explain that the maximum power that can be applied to an SMA wire without the danger of damaging it is computed by Equation 6.1:

$$P_{max} = {I_{safe}}^2 \times R_{SMA} = 1^2 \times R_{SMA} \tag{6.1}$$

where P_{max} is the maximum power that can be supplied to the SMA wire without damaging it, I_{safe} is the manufacturer-recommended safe current for the SMA wire, equal to 1 A, and R_{SMA} is the martensite value of the resistance of a given length of an SMA wire. Given that the length of the SMA wire under stress is about 10.23 inches and that the resistance per unit length for the SMA wire used is 0.5 Ω/inch, the expected resistance for the SMA wire used is approximately 5.12 Ω. Using Equation 6.1, P_{max} in this case would equal 5.12 W.

However, given the voltage across the SMA wire is 12 V, the maximum current that can be used to heat the SMA wire without damaging it would be $I_{max} = P/V = 5.12/12 = 0.427$ A. Given that the maximum current value recorded in all experimental runs (i.e., for the lowest value of SMA resistance in the austenite phase) was 2.45 A, this corresponds to a duty cycle of approximately 17%. This is very close to the minimum duty cycle needed to actuate the SMA wire experimentally at 20 °C (room temperature), which was found to be 16%. However, when this duty cycle was used to actuate the wire at −30 °C, the wire did not fully contract. This can be seen in Figure 6.4 where no plateau in the displacement can be observed. Consequently, as explained in Section 6.2, this experiment was run

several times at each temperature to determine the minimum duty cycle that will cause the SMA wire to achieve maximum contraction at that specific temperature.

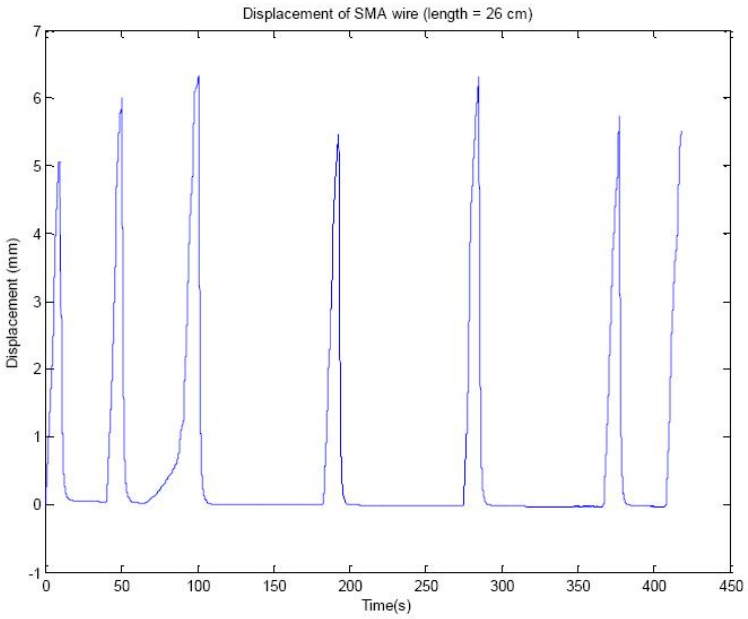

Figure 6.4: Displacement of SMA wire at $-30\,^{\circ}$C when heated with PWM signal of duty cycle = 16%

6.3.2 No Priming

As the name suggests, the *No Priming* experiments employed no priming prior to the actuation periods. In these experiments, *Priming_duty* during the priming period was again set to 0.5% in order to enable resistance monitoring. However, *Act_duty* was set to 1.5 * *Mtn_duty*. These were run to serve as a benchmark to illustrate the effects of priming. Since the primary goal of the different priming strategies discussed in Section 5.3 is to get the SMA resistance close to the cusp that exists at the onset of actuation, one would expect the results for the priming strategies to be consistently better than those for *No Priming*.

6.4 Actuation strategy

The goal of the actuation strategy was to achieve maximum contraction of the SMA wire in a consistent period of time regardless of the ambient conditions. Apart from

the experiments implementing the *Safe Duty* strategy, all the experiments implemented the same actuation strategy. Through experimentation, it was determined that applying a duty cycle = 1.5 * *Mtn_duty* during the actuation period was sufficient in getting the wire to actuate consistently under all temperatures.

6.5 Comparison metrics

To compare the performance of the different priming strategies under the various ambient temperature conditions, two measures were defined: Time-to-Cusp (TTC) and Absolute Strain Time (AST). TTC is defined as the time from the start of the actuation period to the cusp. The smaller the TTC the more effective the priming strategy is. AST is defined as the time needed to contract the SMA wire to 1% strain from the start of the actuation period. The goal is to obtain a consistent AST under all temperature conditions. One should note that this measure favours the priming strategy that causes more pre-actuation contraction.

The TTC and the AST are both functions of the average priming current and actuation current (based on the priming duty cycle, *Priming_duty* and the actuation duty cycle, *Act_duty*, respectively). With TTC, a higher priming current generally means that the SMA resistance will be closer to the resistance value at the cusp prior to actuation. Moreover, a higher actuation current means that resistance will rise faster to the cusp from the onset of the actuation signal. Since AST includes TTC, it will also depend on both the priming current and the actuation current. Furthermore, a higher actuation current would cause the SMA wire to contract faster reducing AST.

In theory, *Mtn_duty*, on which *Priming_duty* and *Act_duty* are based, should be the same for a given ambient temperature. However, in practice, due to noise and other real-world limitations, they are not. Thus, in order to make comparisons between the different priming strategies, the following two postulates have been formulated:

- Postulate 1: If priming strategy A obtains a smaller TTC compared to priming strategy B, then priming strategy A is a better priming strategy. If both priming strategies have similar TTCs, then the priming strategy that uses less energy is the better priming strategy.
- Postulate 2: If priming strategy A needs less energy to obtain a smaller or equal AST compared to priming strategy B, then priming strategy A is a

better priming strategy. This is due to the fact that all the experiments use the same actuation strategy. Thus, the smaller AST must be the result of better priming.

Figures 6.5 and 6.6 demonstrate how the TTC and AST are determined respectively. For example, in these figures, the actuation segment begins at 180 s. Thus, these measures are determined from this point. Note that there are three actuation segments per experimental run. Therefore, the averages of these metrics for the three segments are used in later graphs to compare the TTC and AST of the different priming strategies. Moreover, the average priming current (denoted by *I_prime* on the graphs) and the average actuation current (denoted by *I_act* on the graphs) are plotted with the TTC and AST respectively. The priming strategies are compared across the five different ambient temperatures.

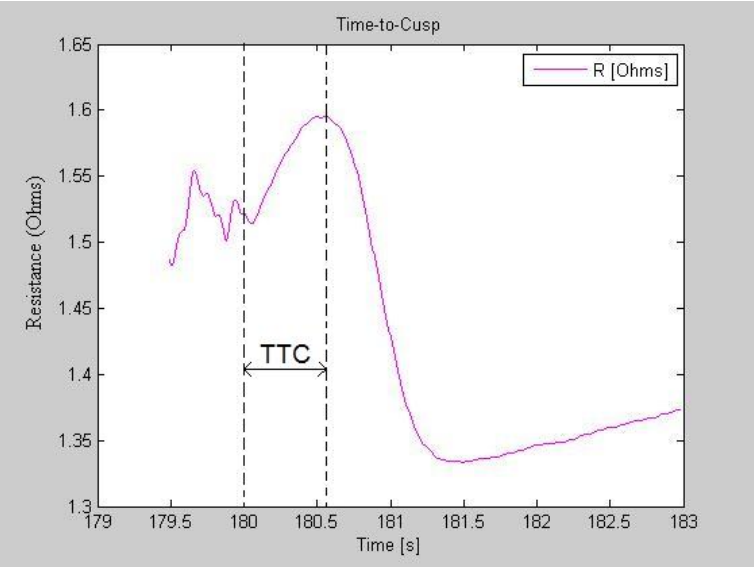

Figure 6.5: Time-to-Cusp (TTC) [7]

6.6 Experimental results

This section is divided into two parts. In the first part, the performance of each priming strategy at the different ambient temperatures is discussed. In the second part, a comparison between the different priming strategies at each ambient temperature will be given in terms of Time-to-Cusp (TTC), Absolute Strain Time (AST), the priming current (*I_prime*) and the actuation current (*I_act*).

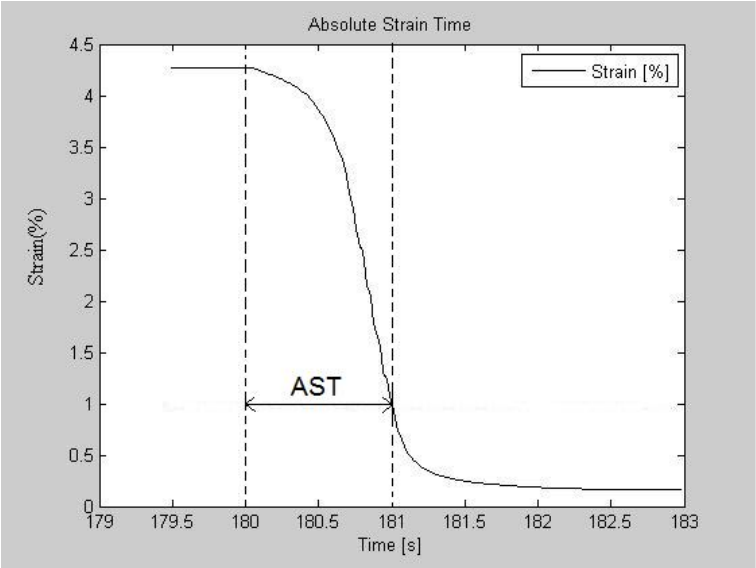

Figure 6.6: Absolute Strain Time (AST) [7]

A sample of the experimental results, obtained from running the *50%*Mtn_duty* priming strategy at $-30\,^{\circ}\mathrm{C}$ is shown in Figure 6.7. Subplots (a) - (d) in Figure 6.7 depict the voltage taken across the SMA wire, the current flowing through it, its computed resistance and its strain respectively. Note that none of these signals are continuous; they are samples taken during the on-cycle of the PWM signal at 20 ms intervals but are connected when plotted in MATLAB.

Although, the power supply used to power the SMA wire is set to 12 V, Figure 6.7(a) only records a maximum voltage of 10.7 V across the wire. This voltage drop is probably due to the voltage dropped across the connecting wires (which are quite lengthy). Looking at Figure 6.7(b), one notices that the instantaneous current between t = 150 - 180 s (corresponds to one of the priming segments of the experiment) is less than when the wire is being cooled between t = 100 - 150 s. This is because, given that the voltage is approximately constant and as the duty cycle is increased between t = 150 - 180 s, the wire primes increasing the resistance of the SMA wire. Consequently, the instantaneous current drops even though the average energy in the wire is greater. As for resistance and strain, since they are continuous physical values, Figures 6.7c and 6.7d give a reasonably accurate depiction of these signals.

Figure 6.8 is a zoomed in view of one of the three priming/actuation cycles that an SMA wire goes through during an experiment. The red curve represents the *effective* current through the SMA wire obtained by multiplying the sampled current shown in Figure 6.7 (b) by the square root of the duty cycle corresponding

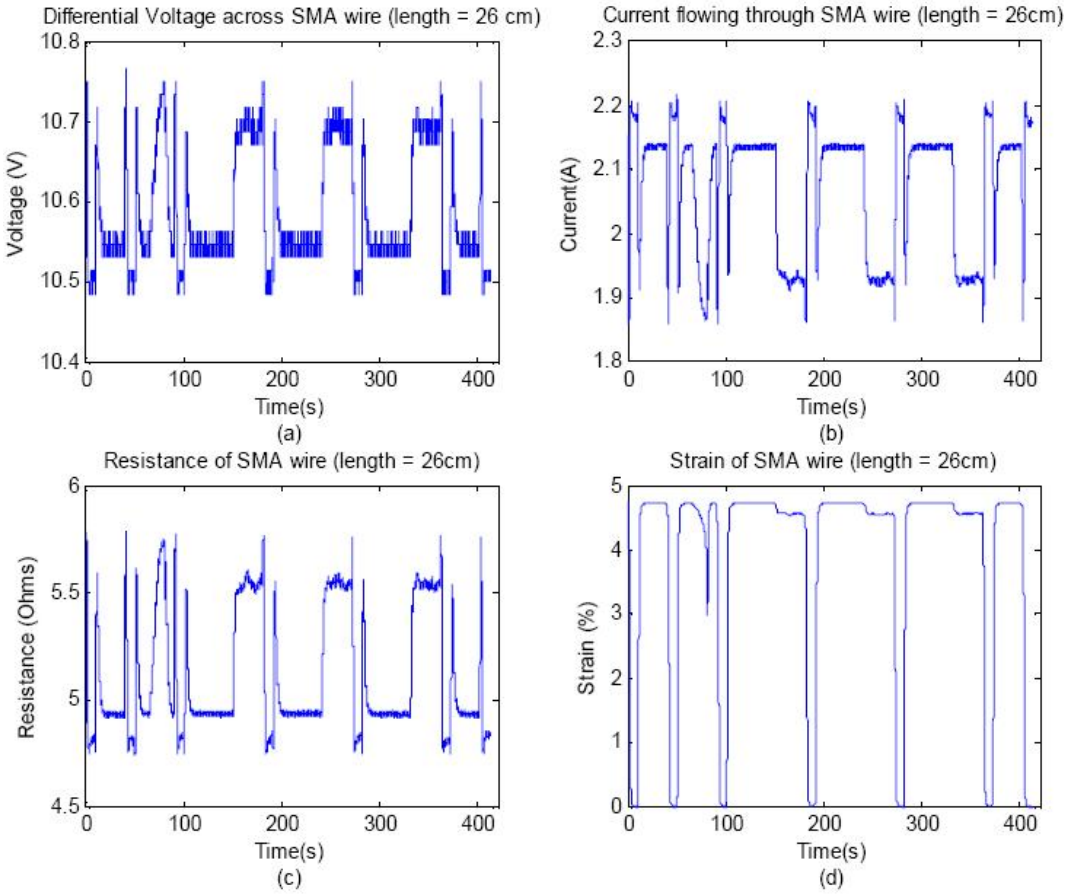

Figure 6.7: Sample of experimental results(a) Voltage samples (b) Current samples (c) Computed resistance (d) Strain

to the experimental segment (cooling, priming, actuating). As can be seen in Figure 6.8, between 180 s and 190 s (which is one of the actuation segments) the effective current is at its maximum value of approximately 0.9 A at an ambient temperature of −30 °C. During this same period of time, the resistance of the SMA wire increases to a cusp and then decreases to its lowest value (as the SMA transforms to austenite). Moreover, the strain of the SMA wire drops to almost 0% during the same period. For the priming segment that exists between 150-180 s, the effective current is at an intermediate value (determined by the priming strategy) between the minimum and maximum current. Strain also decreases slightly from the cool strain (between 100 s and 150 s). The same applies to resistance which is maintained at a value that is less than the cusp but larger than when the wire is being cooled (between 100-150 s).

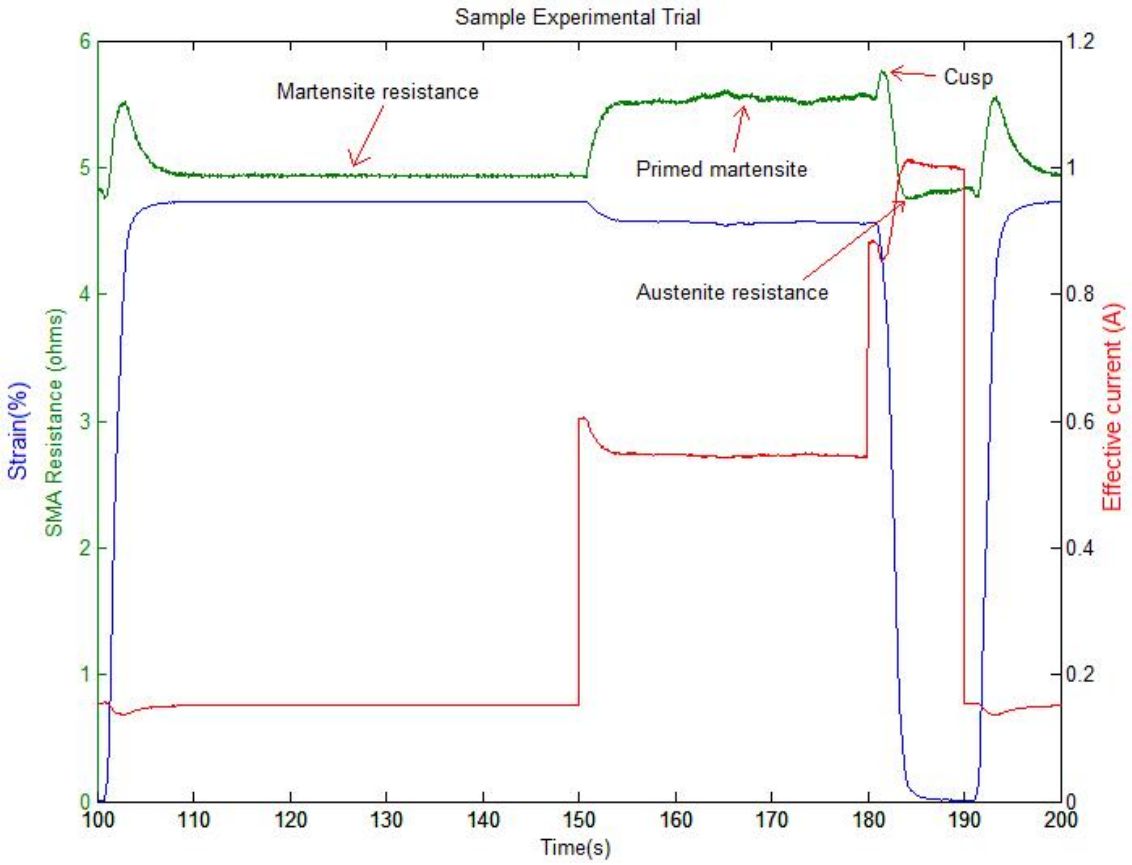

Figure 6.8: A priming/actuation cycle during an experimental run for the *50%*Mtn_duty* priming strategy at −30 °C

Figure 6.9 shows a zoomed in view of the probing period. The effective current increases in a staircase fashion because the duty cycle is increased at a rate of 1%/s until the wire begins to actuate. This takes place at approximately t = 81 s, at

which point the effective current is brought down to its lowest value. Also, at this instant in time, the resistance of the wire has been decreasing for 1 s (i.e. from 80-81 s). This is taken to indicate that the wire is on the verge of complete actuation. This is also seen in the strain (blue) curve where the strain reaches a local minimum and then goes up again when the effective current is reduced.

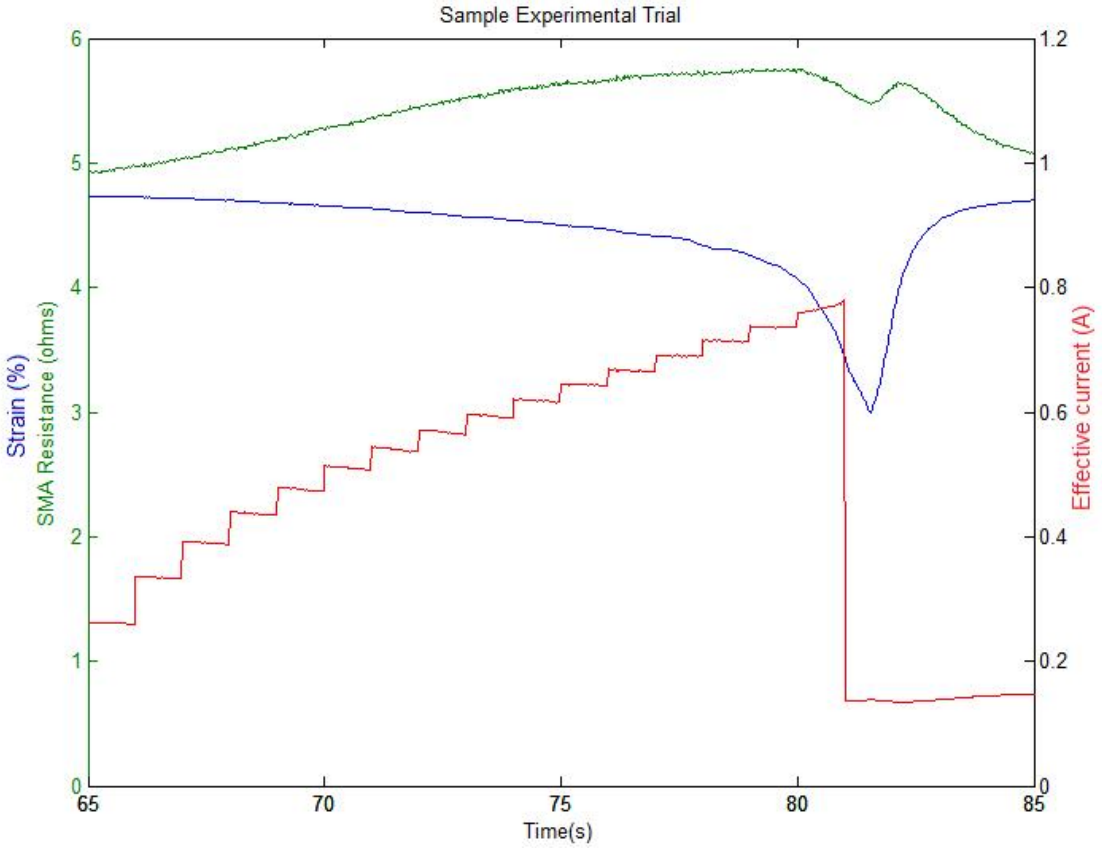

Figure 6.9: Probing period during an experimental run

6.6.1 Comparing performance of each priming strategy at different ambient temperatures

Safe Duty at different ambient temperatures

Recall that the *Safe Duty* priming strategy entailed using a certain duty cycle (determined experimentally) to actuate the wire during the actuation segments while no actual priming took place during the priming segments (the wire was left to cool by setting the duty cycle to 0.5%). The average TTC for the *Safe Duty* priming strategy is shown in Figure 6.10. Except at 0 °C, TTC decreases

with increasing ambient temperature. There is one thing to note about *I_prime*: it decreases with increasing temperature although *Priming_duty* was always set to 0.5%. This can only be explained by the higher ambient temperature: as the ambient temperature increases, the wire resistance also increases. Consequently, the effective current decreases.

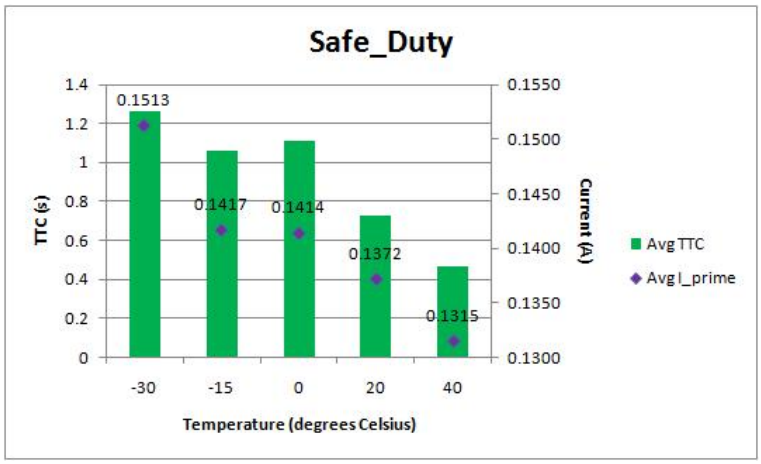

Figure 6.10: Comparison of Time-to-Cusp for *Safe Duty* at different temperatures

The average AST for the different temperatures is shown in Figure 6.11. The fact that the AST at 0 °C is larger than those at −30 °C, −15 °C and 20 °C makes sense since its *I_act* has the smaller value. However, the AST at 40 °C is smaller than that at 0 °C although its *I_act* is smaller. This discrepancy could possibly be attributed to the higher ambient temperature aiding in the quicker actuation of the SMA wire and also to its lower TTC which is included in the AST.

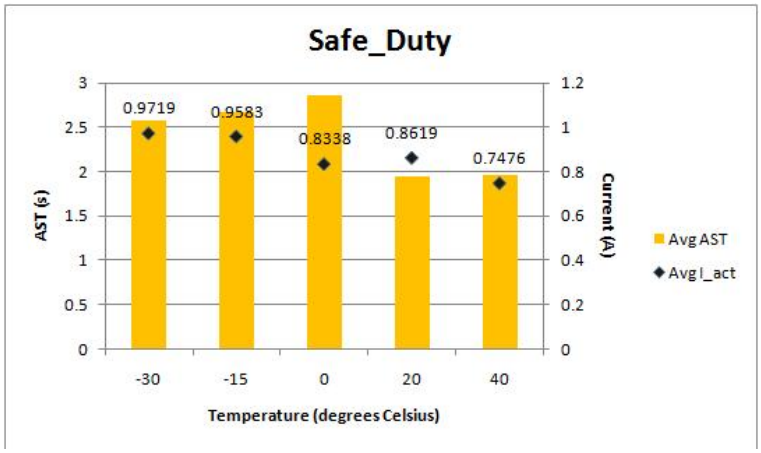

Figure 6.11: Comparison of Absolute Strain Time for *Safe Duty* at different temperatures

A very important conclusion can be drawn from Figure 6.11: the *fixed* "safe" current specified by the manufacturers' data sheets will not actuate the wire under all ambient conditions.

No Priming at different ambient temperatures

As mentioned earlier, the *No Priming* strategy involved setting *Act_duty* = 1.5 * *Mtn_duty* during the actuation segments of the experiment. As for the priming segments, the wire was again left to cool by setting the duty cycle to 0.5%. Figure 6.12 shows the average TTC for the *No Priming* strategy across the different temperatures. *I_prime* values at the different temperatures are identical to those in the *Safe Duty* strategy above. This makes sense as the duty cycle during the priming segment was also set to 0.5%. Moreover, similar to Figure 6.10, TTC decreases with increasing ambient temperature with the only exception being at 0°C. The fact that TTC at 0°C does not follow the trend could be attributed to experimental differences especially as these experiments were not conducted in a sequential manner i.e. from low to high temperatures or vice

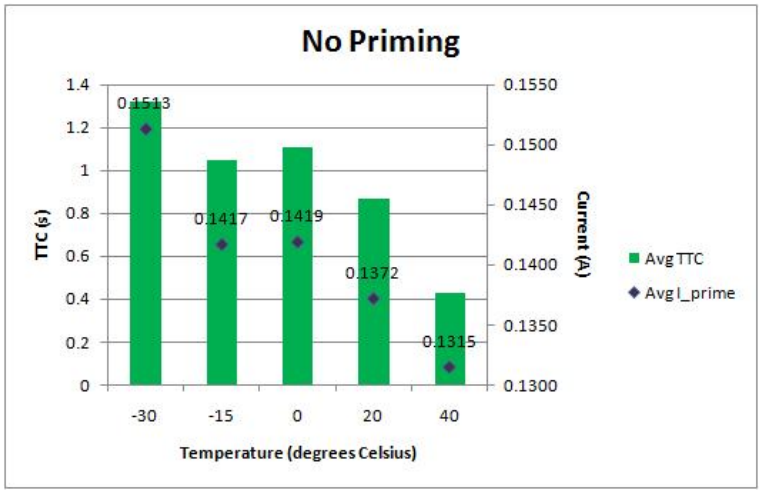

Figure 6.12: Comparison of Time-to-Cusp for *No Priming* at different temperatures

As for the average ASTs shown in Figure 6.13, the smallest AST is achieved at 40°C. Moreover, this smallest AST is achieved with the smallest *I_act*. This supports the hypothesis that the higher ambient temperature is aiding in the quicker actuation of the SMA wire. Note that this strategy was developed only as a benchmark to study whether priming in general will help with wire actuation.

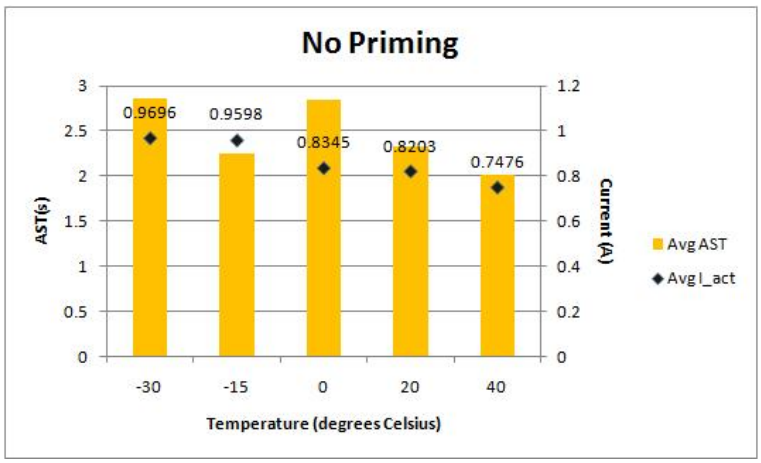

Figure 6.13: Comparison of Absolute Strain Time for *No Priming* at different temperatures

*50%*Mtn_duty* at different ambient temperatures

In the *50%*Mtn_duty* priming strategy, the wire is primed by applying 50% of the maintenance duty cycle, *Mtn_duty*, to it. The wire is then actuated by applying *Act_duty* = 1.5**Mtn_duty*. The average TTC for the *50%*Mtn_duty* priming strategy is shown in Figure 6.14. For this strategy, both TTC and *I_prime* decrease consistently with increased ambient temperature with the TTC at 40 °C being significantly lower than the TTCs at all the other temperatures. Notice that, in this strategy, *I_prime* is more than three times as large as its values in the *Safe Duty* and *No Priming* strategies as the duty cycle during the priming segment is much larger than 0.5%.

Although the trend of AST values shown in Figure 6.15 is similar to that in Figure 6.13, the smallest AST achieved under the *50%*Mtn_duty* strategy is at 20 °C rather than 40 °C. Moreover, Figure 6.15 indicates that the *50%*Mtn_duty* priming strategy together with the actuation strategy do not achieve the goal of obtaining consistent AST values across different ambient temperatures. Another thing to note is that, *I_act* should be approximately 1.7 × *I_prime* (based on *Act_duty* = 3.0 × *Priming_duty*). However, looking at the different ambient temperatures, one finds that the *I_act* values are in fact a little higher. This can be attributed to the fact that during the probing segment, the duty cycle was ramped at a rate of 1% /s. This means that the *Mtn_duty* determined could have a maximum error of 0.5%.

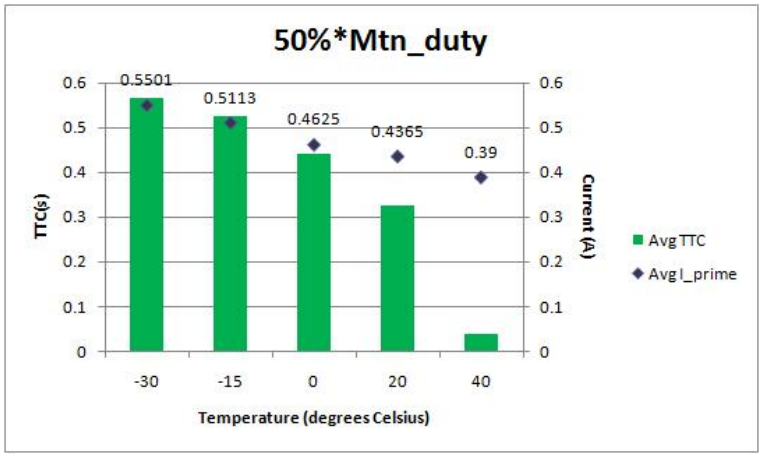

Figure 6.14: Comparison of Time-to-Cusp for *50%*Mtn_duty* at different temperatures

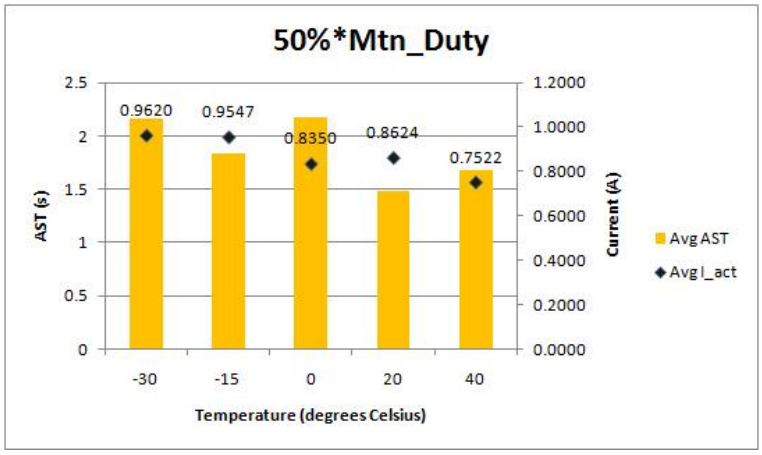

Figure 6.15: Comparison of Absolute Strain Time for *50%*Mtn_duty* at different temperatures

Peak Detector 1 at different ambient temperatures

The *Peak Detector 1* strategy servoes around the cusp where the theoretical value of dR/dt is 0. The cusp is detected using a peak detector and then a Bang-Bang controller is initialized that maintains the resistance at the cusp by outputting either a small duty cycle (cooling) or a large duty cycle (heating). Figure 6.16 shows the average TTC for the *Peak Detector 1* strategy across the different temperatures. Once again, TTC generally decreases with increasing ambient temperature with the only exception, this time, being at 20 °C. The only anomaly in Figure 6.16 is that the TTC at 20 °C is larger than that at 0 °C despite the fact that *I_prime* at the former temperature is larger than that at the latter. A possible explanation for this could be the fact that these experiments were not conducted in sequence i.e. experiments were not conducted at −30 °C then −15 °C and so on, in a sequential manner. This could have affected results due to a change in the environment or may be even due to wire fatigue.

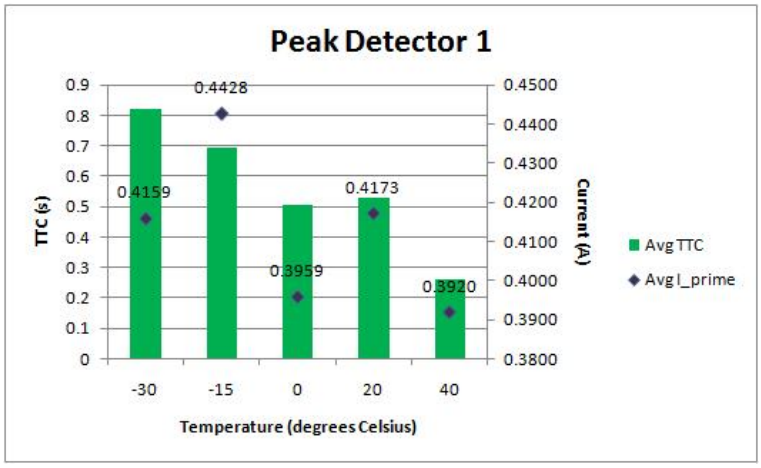

Figure 6.16: Comparison of Time-to-Cusp for *Peak Detector 1* at different temperatures

As for the average ASTs, Figure 6.17 indicates that the smallest AST is achieved at 40 °C. If the five different ambient temperatures are taken into consideration, then one can conclude that the *Peak Detector 1* priming and actuation strategies together do not achieve the goal of consistent ASTs. However, if the results at −30 °C are excluded, then one can notice that the *Peak Detector 1* strategy achieved more consistent ASTs between −15 °C and 40 °C compared to the previous strategies.

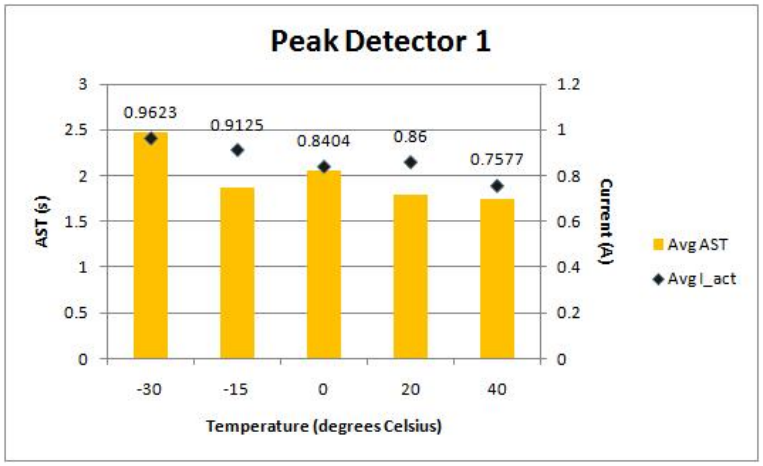

Figure 6.17: Comparison of Absolute Strain Time for *Peak Detector 1* at different temperatures

Minus 4.5% at different ambient temperatures

The *Minus 4.5%* strategy involves priming the wire with a duty cycle *Priming_duty* = *Mtn_duty* - 4.5%. Figure 6.18 shows the average TTC for this strategy across the different temperatures. Except at 20 °C, TTC decreases with increasing ambient temperature. Moreover, *I_prime* decreases as ambient temperature increases which makes sense given that *Mtn_duty* will also decrease with rising temperature. The only anomaly in this set of results is that at 20 °C, TTC is larger than that at 0 °C contrary to what one would expect. However, as mentioned ealier, this can be due to the fact that these experiments were not run sequentially from low to high temperatures.

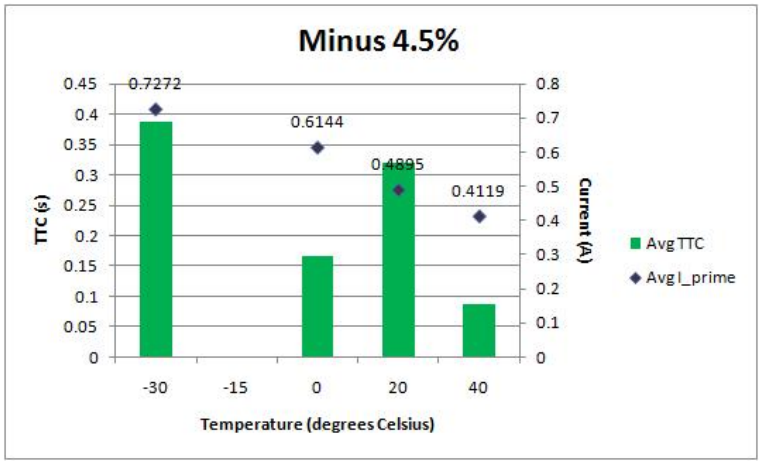

Figure 6.18: Comparison of Time-to-Cusp for *Minus 4.5%* at different temperatures

Figure 6.19 depicts the average AST values for the *Minus 4.5%* strategy at the different temperatures. An important observation here is that AST at 20 °C is significantly smaller than at 0 °C and 40 °C. One would have expected it to be the other way around given the facts that the TTC at 20 °C was larger than those at the other two temperatures and that AST includes TTC. However, one should also note that *I_act* at 20 °C was larger than at 0 °C and 40 °C which could explain why it ended up having the least AST. As for achieving consistent ASTs, if the AST values for *Minus 4.5%* between 0 °C and 40 °C are compared to those for *Peak Detector 1*, then clearly the latter still performed better.

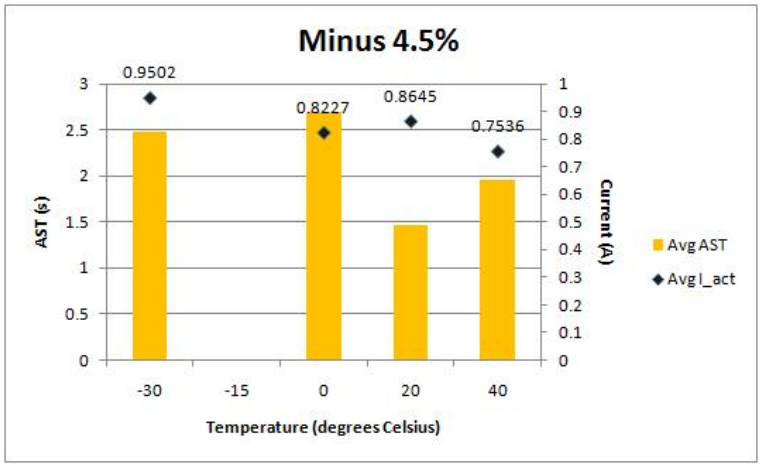

Figure 6.19: Comparison of Absolute Strain Time for *Minus 4.5%* at different temperatures

Note that the experimental results for the *Minus 4.5%* strategy at −15 °C were not shown because the experiments were not conducted due to a problem with the circuit. However, this issue is currently being investigated.

6.6.2 Comparing Performance of all Priming Strategies at each ambient temperature

$T_{amb} = -30\,^{\circ}\mathbf{C}$

The average TTC for each priming strategy is shown in Figure 6.20. The *Safe_Duty* and the *No Priming* strategies performed generally the same. This was expected as the average priming current in both strategies was equal to 0.1513 A when the duty cycle during the priming segment of the experiments was set to 0.5%. The *Minus 4.5%* strategy yielded the lowest average TTC among all the priming strategies.

This makes sense given that it had the largest *I_prime*. The bigger TTC obtained in *Peak Detector 1*, compared to *50%*Mtn_duty* and *Minus 4.5%*, is due to its lower *I_prime*. This can be attributed to the fact that the higher limit of the Bang-Bang controller was set to *Mtn_duty* as a tradeoff between heating the SMA wire quickly and at the same time preventing it from undergoing spurious actuation. If a larger value is used for this higher limit then one could expect the TTC to decrease.

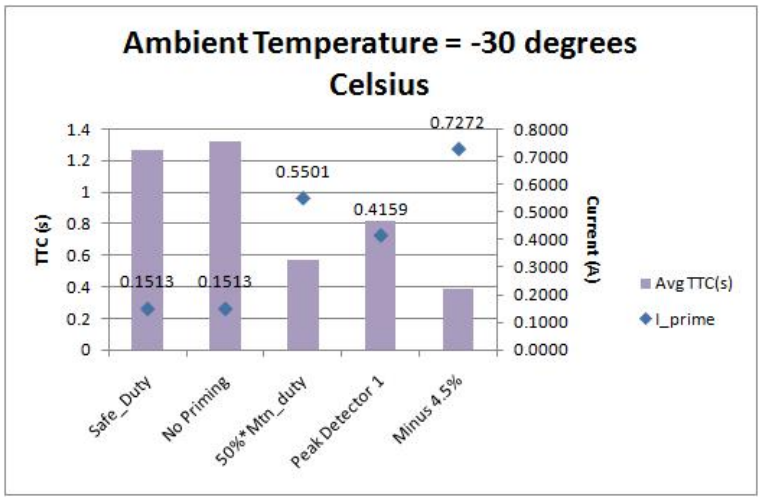

Figure 6.20: Comparison of Time-to-Cusp for $T_{amb} = -30\,^{\circ}\mathrm{C}$

The average ASTs for the different priming strategies are shown in Figure 6.21. Given that the average *I_act* across all strategies is approximately the same, the difference observed in the average ASTs can be attributed to the average *I_prime* values since AST is a function of the average priming current.

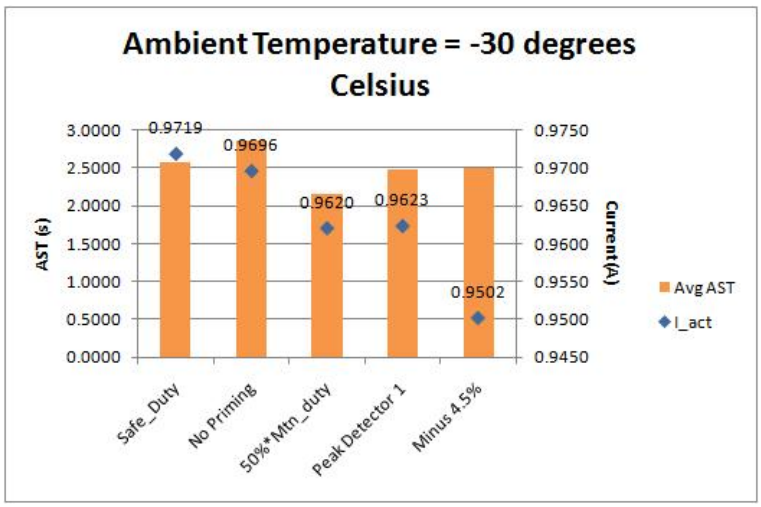

Figure 6.21: Comparison of Absolute Strain Time for $T_{amb} = -30\,^{\circ}\mathrm{C}$

$T_{amb} = -15\,^{\circ}\mathbf{C}$

The average TTCs for the experiments conducted at $-15\,^{\circ}$C are shown in Figure 6.22. Again, the *Safe_Duty* and the *No Priming* strategies had similar performance given their equivalent *I_prime*. Since the *50%*Mtn_duty* strategy had the largest average *I_prime*, its TTC had the smallest value.

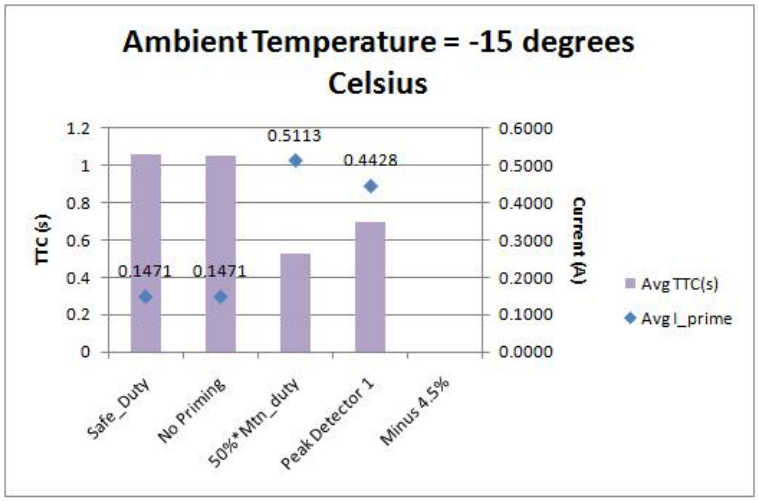

Figure 6.22: Comparison of Time-to-Cusp for $T_{amb} = -15\,^{\circ}$C (Note that the *Minus 4.5%* experiment was not conducted due to problems with the hardware)

The average ASTs are shown in Figure 6.23. Despite the fact that the *Peak Detector 1* strategy's *I_act* was lower than those of the *Safe_Duty* and the *No Priming* strategies, its smaller AST can be explained by its larger *I_prime* value. On the other hand, despite *Peak Detector 1* having a smaller *I_prime* and a smaller *I_act* compared to *50%*Mtn_duty*, its AST was not much larger.

Note that the experimental results for the *Minus 4.5%* strategy at $-15\,^{\circ}$C were not shown because the experiment was not conducted due to a problem with the hardware.

$T_{amb} = 0\,^{\circ}\mathbf{C}$

Figure 6.24 shows the same trend as in Figure 6.20. Given that their respective *I_prime* values were equal, the *Safe_Duty* and the *No Priming* strategies had approximately the same TTC. The *Minus 4.5%* strategy had the smallest TTC since it had the largest average *I_prime*.

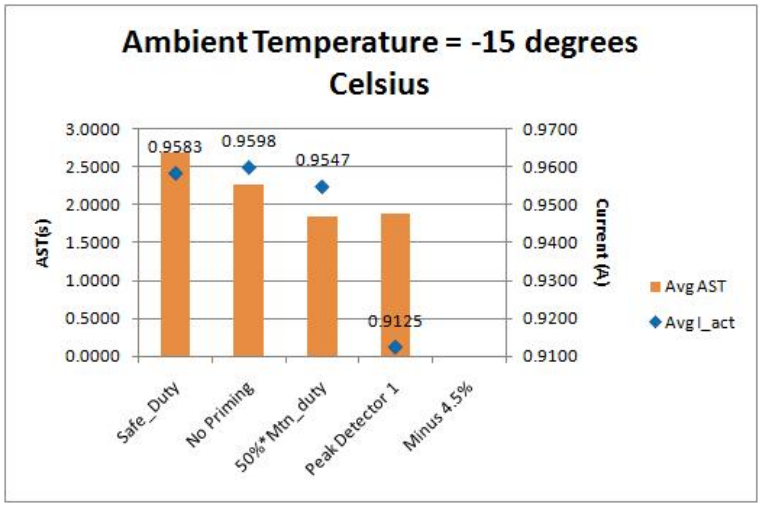

Figure 6.23: Comparison of Absolute Strain Time for $T_{amb} = -15\,^{\circ}\mathrm{C}$ (Note that the *Minus 4.5%* experiment was not conducted due to problems with the hardware)

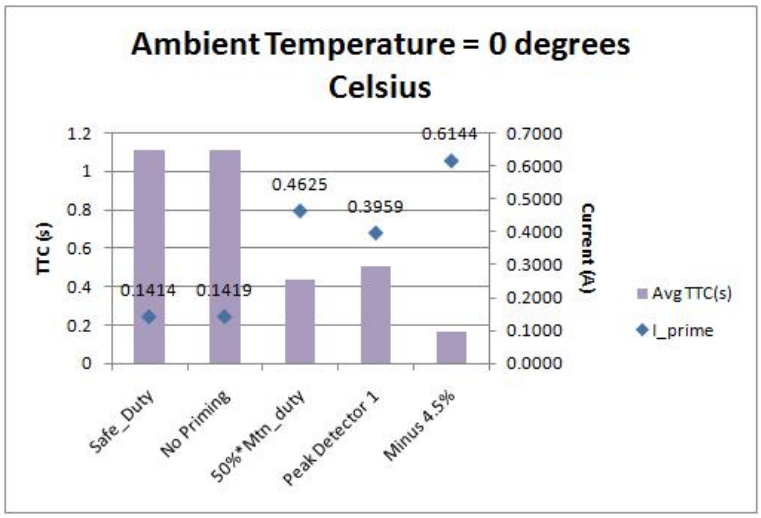

Figure 6.24: Comparison of Time-to-Cusp for $T_{amb} = 0\,^{\circ}\mathrm{C}$

As can be seen in Figure 6.25, *Peak Detector 1* and *50%*Mtn_duty* had comparable AST values. Given that fact that both strategies had almost equal *I_act* values, and since they both had similar TTC values, this probably makes sense. The anomaly here however is in the *Minus 4.5%* strategy. Its *I_act* is almost equal to those of *Peak Detector 1* and *50%*Mtn_duty* and its TTC is significantly smaller than those of the latter two strategies. Yet, when compared to *Peak Detector 1* and *50%*Mtn_duty*, its AST was considerably larger. A possible explanation to this anomaly is changes in the wire from one experiment to the other (e.g. fatigue).

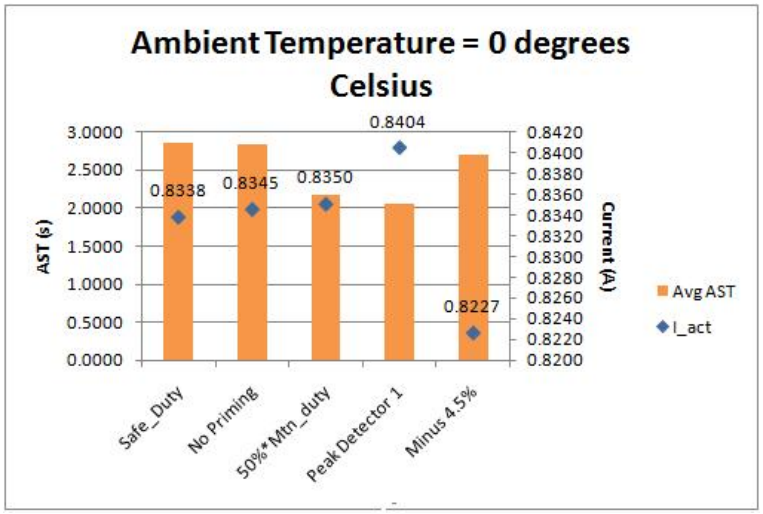

Figure 6.25: Comparison of Absolute Strain Time for $T_{amb} = 0\,^{\circ}\mathrm{C}$

$T_{amb} = 20\,^{\circ}\mathbf{C}$

Figure 6.26 depicts the average TTCs for the different priming strategies at 20 °C. The observation to note here is that, although the *Safe_Duty* and the *No Priming* strategies had equal *I_prime*, the latter had a significantly larger TTC. Since, both essentially used the same duty cycle (0.5%) during the priming segment, the discrepancy in the TTC between the two strategies could be due to experimental effects.

As for the average ASTs shown in Figure 6.27, the fact that *No Priming* had the largest AST makes sense since its *I_act* is the smallest among all the strategies. However, looking at the remaining priming strategies, one finds that the *I_act* values are essentially identical with the minimum and maximum values within 0.5% of each other. Thus, since the ambient temperature is held constant and the same actuation strategy is applied in all experiments, the differences in AST can be

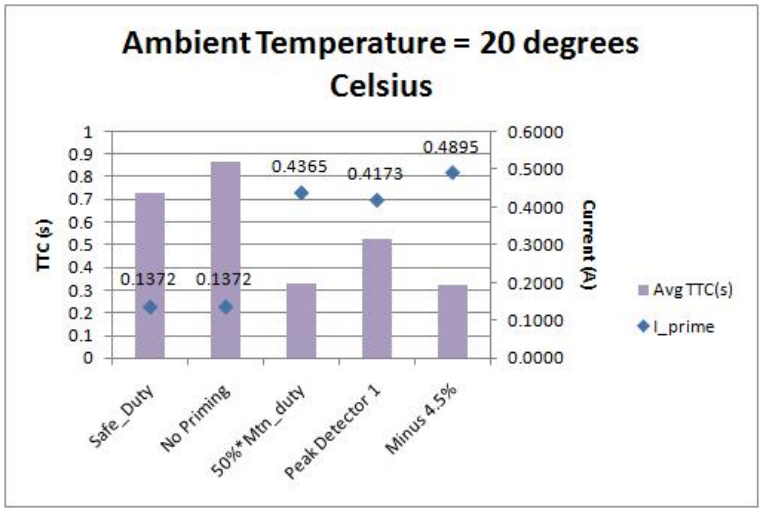

Figure 6.26: Comparison of Time-to-Cusp for $T_{amb} = 20°\text{C}$

entirely attributed to changes in priming strategy. This is indeed reflected in the TTCs: if TTC is subtracted from AST, the difference is roughly 1.2s for each strategy.

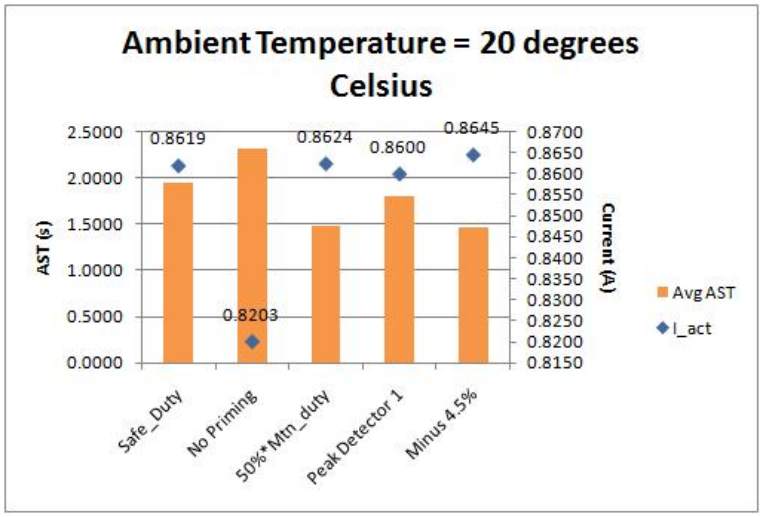

Figure 6.27: Comparison of Absolute Strain Time for $T_{amb} = 20°\text{C}$

$T_{amb} = 40°\text{C}$

In Figure 6.28, the *Safe_Duty* strategy had the largest TTC. The thing to note here is that despite *Minus 4.5%* having the largest *I_prime*, its TTC was larger than that of the *50%*Mtn_duty* with the smaller *I_prime*.

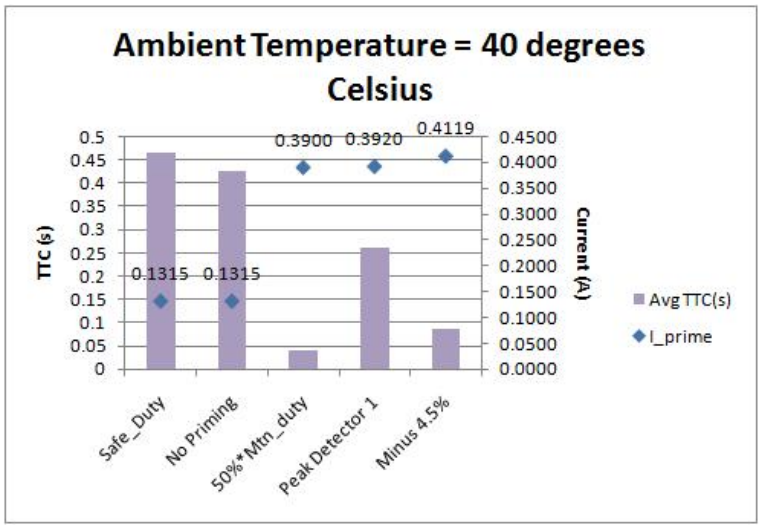

Figure 6.28: Comparison of Time-to-Cusp for $T_{amb} = 40°C$

In Figure 6.29, *Safe_Duty* and *No Priming* had equal *I_act* and hence, approximately the same AST. *50%*Mtn_duty* had the smallest AST, even smaller than the *Peak Detector 1* and the *Minus 4.5%* strategies that have larger *I_act* values. However, this can attributed to *50%*Mtn_duty*'s smaller TTC which is included within AST.

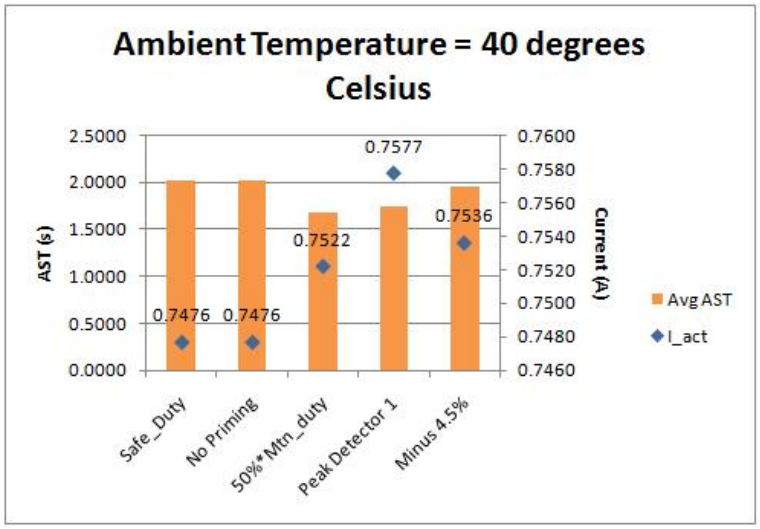

Figure 6.29: Comparison of Absolute Strain Time for $T_{amb} = 40°C$

Table 6.1: Difference between TTC of priming strategy and that of *No Priming*

Temperature (degrees Celsius)	Range by which priming reduces TTC (s)
-30	0.5000-0.9333
-15	0.3534-0.5200
0	0.6000-0.9400
20	0.3400-0.5467
40	0.1667-0.3867

6.7 Discussion of results

Comparing the TTC obtained by the various priming strategies at different ambient temperatures in Figure 6.30 shows that the *Safe Duty* and *No Priming* performed almost the same. This makes sense given that no priming technique was implemented in either. However, when comparing the remaining priming strategies against *No Priming*, it becomes clear that employing any form of priming helps reduce TTC. Table 6.1 quantifies the range, in seconds, by which the TTC of the different priming strategies were lower than that obtained by the *No Priming* strategy.

Table 6.2: Difference between AST of priming strategy and that of *No Priming*

Temperature (degrees Celsius)	Range by which priming reduces AST (s)
-30	0.3700-0.6967
-15	0.3800-0.4166
0	0.1467-0.7800
20	0.5233-0.8567
40	0.0533-0.34

Figure 6.30 also shows that the *Minus 4.5%* strategy had consistently the smallest TTC except at 40 °C where the *50%*Mtn_duty* strategy had the smallest TTC. The *Peak Detector 1* strategy, the only closed-loop control strategy implemented, performed better than *Safe_Duty* and *No Priming* but worse than *50%*Mtn_duty* and *Minus 4.5%* in terms of TTC. However, this can be attributed to the maximum duty cycle output by the Bang-Bang controller which was set to *Mtn_duty*. If the value of this upper limit is increased to say, 1.2 × *Mtn_duty*, then one could expect lower TTC values at the different ambient temperatures. Finally, apart from a few exceptions, the average TTC for any one priming strategy decreased with increased ambient temperature. This occurred despite the fact that the maximum duty cycle used in a certain priming strategy was reduced as the ambient temperature was increased to prevent the wire from overheating. Thus, this reduction in TTC can be attributed to the higher ambient temperature that will increase the resistance of the SMA wire even before heating it with a current.

Figure 6.31 shows the AST achieved with the various priming strategies at the different ambient temperatures. Despite the fact that the same actuation strategy was applied in all the experiments, the ASTs for the *50%*Mtn_duty*, *Peak Detector 1* and *Minus 4.5%* strategies at the different temperatures were less than those obtained for the *No Priming* strategy at those temperatures. These differences can only be attributed to the smaller TTC values since TTC is part of the AST. Table 6.2 quantifies the range, in seconds, by which the AST of the different priming strategies were lower than that obtained by the *No Priming* strategy.

Looking at Tables 6.1 and 6.2, one observes that the maximum reduction in AST due to priming is less than the maximum reduction in TTC. For example, at −30 °C, the maximum reduction in TTC due to priming was approximately 1 s, while for AST, the maximum reduction was only about 0.7 s. In the case of the *Minus 4.5%* strategy, its TTC at −30 °C, was approximately 1 s less than that of *No Priming* at the same temperature; however, its AST was only about 0.4 s less. This

suggests that there lies room for improvement in terms of reducing ASTs further which would require developing new actuation strategies.

Moreover, comparing the AST across the different ambient temperatures in Figure 6.31 indicates that, for the most part, implementing the *50%*Mtn_duty* strategy yielded the smallest AST among the different priming strategies. The *Peak Detector 1* strategy yielded the second best set of results in terms of AST with AST values smaller than those of *Minus 4.5%* at −30 °C, 0 °C and 40 °C. However, with regard to achieving consistent AST values across different ambient temperatures, the *Peak Detector 1* strategy performed better than the rest, particularly if compared between temperatures −15 °C to 40 °C only. Again, since TTC is included in AST, if the maximum duty cycle in the Bang-Bang controller is increased to a value larger than *Mtn_duty*, then this could reduce TTC and consequently AST. Also, generally speaking, when *I_act* increased, AST decreased. However, recall that the main goal of the actuation strategy was to actuate the SMA wire in approximately the same amount of time regardless of the ambient temperature. This is clearly not the case as can be seen in Figure 6.31. This may suggest that setting $I\_act = 150\%*I\_mtn$ was not an effective strategy in achieving consistent ASTs. Consequently, a completely different actuation strategy will have to be developed that will be capable of achieving consistent ASTs across the different ambient temperatures.

Another important observation from the experimental results is that the maximum contraction of the SMA wire decreased as the ambient temperature was increased. For example, the maximum contraction recorded for the different experiments conducted at 0 °C was 12.0660 mm while the maximum contraction recorded for 20 °C was 11.8977 mm. There are two hypothesis to explain this difference in maximum contractions: (1) thermal expansion of the experimental jig to which the SMA wire is connected causing erroneous strain readings and,(2) ambient temperature increase causes some premature contraction of the wire before the control experiment begins and the encoder is zeroed. To investigate these hypotheses, an experiment was conducted where only the ambient temperature in the fridge was increased from −30 °C to 40 °C. Note that **no** current was used to heat the SMA wire in this experiment. The ambient temperature and the displacement of the SMA wire were sampled every 5 minutes with the temperature increasing at an average rate of approximately 0.1 °C/min. By the time the ambient temperature reached 40 °C, the encoder recorded a contraction of 0.9353 mm. The displacement recorded by the encoder at −30 °C, −15 °C, 0 °C, 20 °C and 40 °C in this last experiment and the maximum displacements that were recorded in the experiments discussed in Chapter 6 are plotted on the same graph in Figure 6.32.

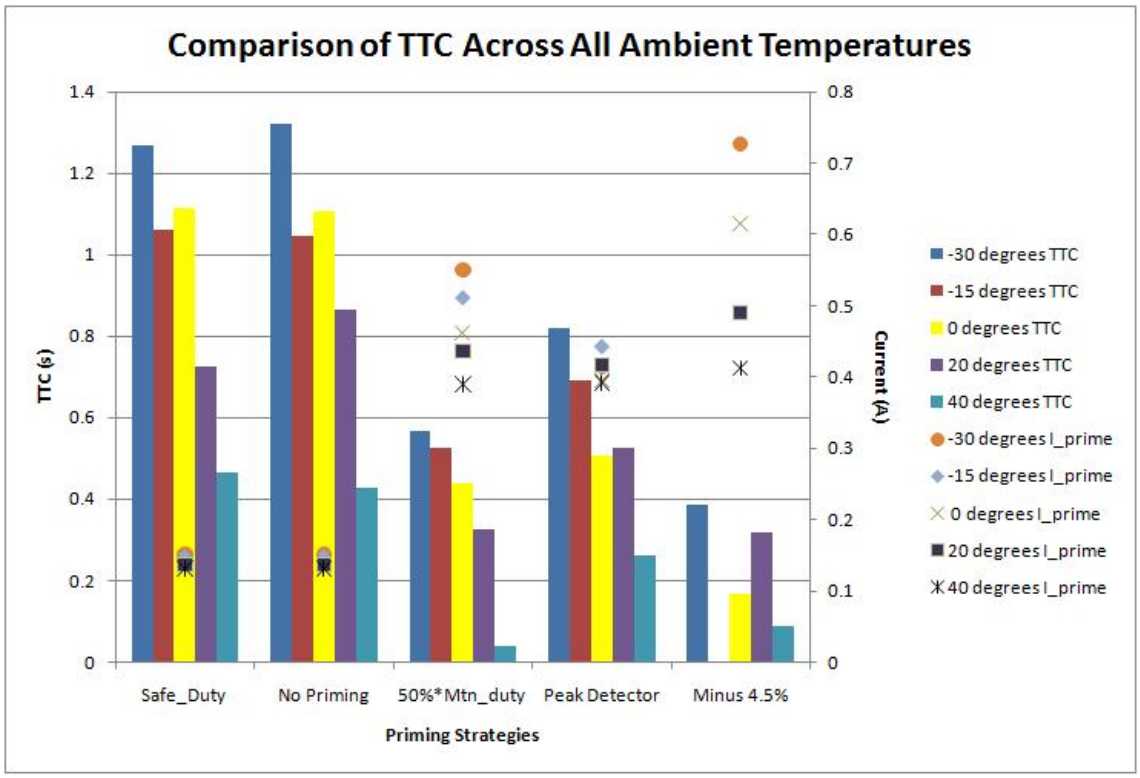

Figure 6.30: Comparison of Time-to-Cusp across the different ambient temperatures (Note that the *Minus 4.5%* experiment was not conducted due to problems with the hardware)

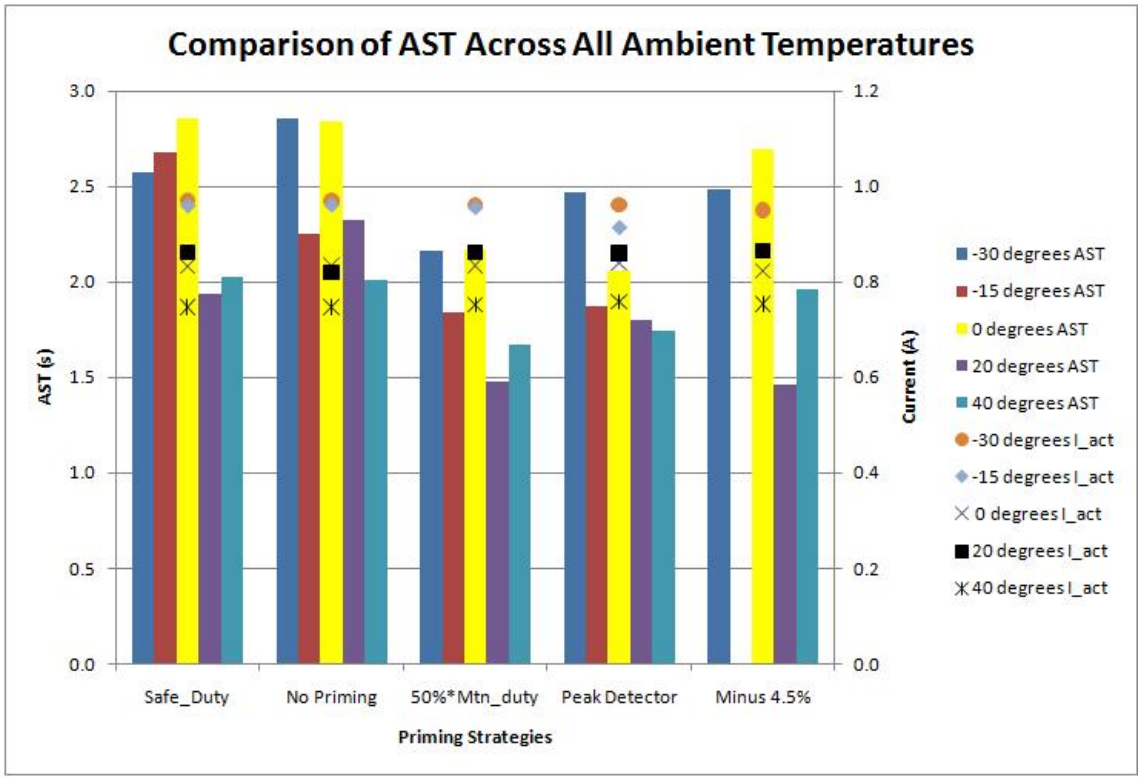

Figure 6.31: Comparison of AST across the different ambient temperatures (Note that the *Minus 4.5%* experiment was not conducted due to problems with the hardware)

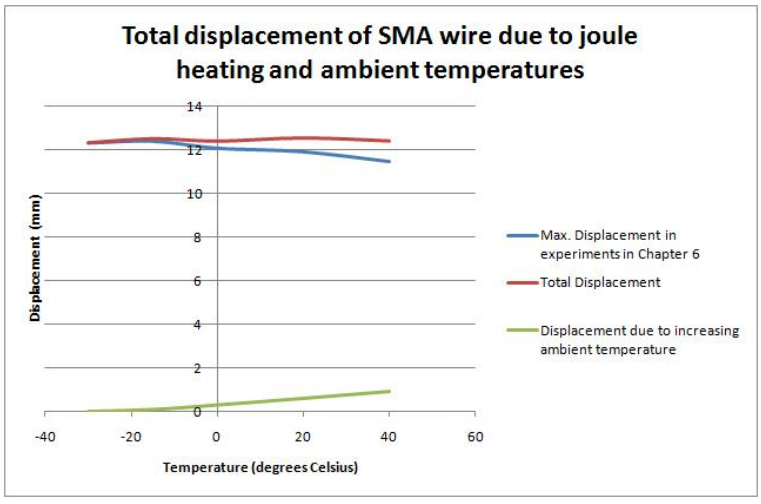

Figure 6.32: Displacement of SMA wire vs its ambient temperature

As can be seen in Figure 6.32, when these two sets of data were added together, the maximum displacement underwent by the SMA wire was approximately constant across all temperatures. This tends to support the hypothesis that the wire is starting out shorter at higher temperatures due to premature contraction. Looking at Figure 6.33 taken from the Flexinol data sheet [12], the SMA wire is still in martensite phase at 40 °C and thus no contraction should be observed. Moreover, for this graph, a constant stress of 20 ksi (approximately 138 MPa) was applied to the wire. However, for the experiments conducted in this research, the constant stress applied to the wire was equal to 178 MPa. Applying a larger stress to the SMA wire means that all the transformation temperatures should shift upwards. This means that A_s should shift to a temperature greater than 90 °C, resulting in even smaller transformation strain at 40 °C. Consequently, the displacement recorded by the encoder cannot be due to wire contraction.

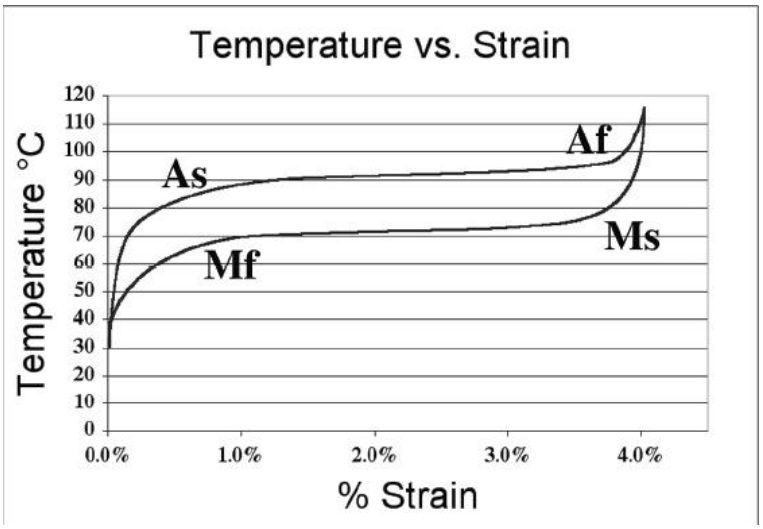

Figure 6.33: Temperature vs Strain hysteresis curve [12]

The other possible explanation to this observation could be the thermal expansion of the stage to which the SMA wire is attached. The expansion of this stage as the temperature increases from −30 °C to 40 °C will rotate the encoder in a way that implies that the actual SMA wire is contracting. The jig to which the SMA wire is attached is made completely of aluminum. Thus, the stage can be viewed as one rectangular plate of aluminum to which the SMA wire is connected as shown in Figure 6.34.

Taking point A in Figure 6.34 to be the origin, thermal expansion will move point B to a new position, B' as shown in Figure 6.35. Given that the horizontal distance between points A and B is 0.380 m, the thermal coefficient of expansion

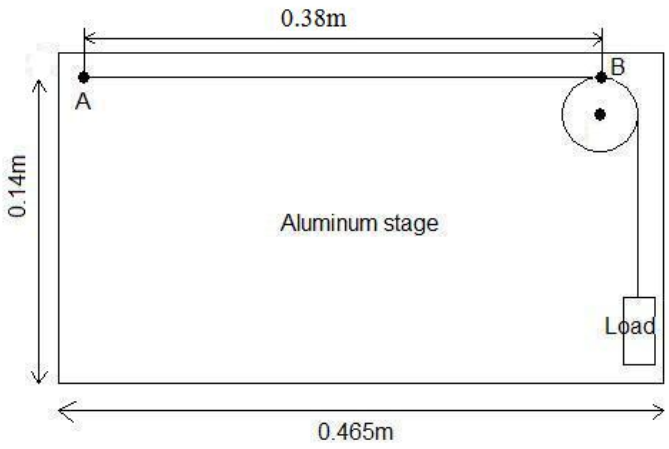

Figure 6.34: Experimental jig modelled as a single block of Al

for Al is 24×10^{-6} /°C, and that the temperature increases from $-30\,°\text{C}$ to $40\,°\text{C}$, then horizontal expansion, $x = 0.380 \times 24 \times 10^{-6} \times 70 = 6.38 \times 10^{-4}\,\text{m} = 0.638\,\text{mm}$. This horizontal expansion will cause the pulley, and hence the encoder, to rotate counter-clockwise which will cause the SMA to appear as if it were contracting.

Relative to point A, point B' will also move in the vertical direction due to thermal expansion of the pulley. Given that the pulley has a radius = 2.0 cm, the vertical expansion will be, $y = 2.0 \times 10^{-2} \times 24 \times 10^{-6} \times 70 = 0.34 \times 10^{-4}\,\text{m} = 0.03\,\text{mm}$. This will appear as "contraction" in the SMA wire. However, looking at Figure 6.36, and by using the Pythagorean Theorem, the new distance d between point A and the new point of contact with the pulley, B', will remain approximately 0.380 m. Consequently, the assumed "contraction" due to the vertical expansion of the pulley will be negligible and thus can be ignored.

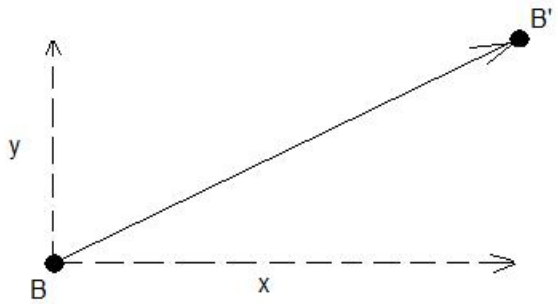

Figure 6.35: Point displaced due to thermal expansion

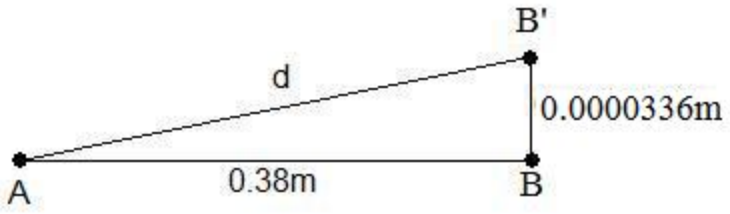

Figure 6.36: Assumed "contraction" of SMA wire due to thermal expansion of jig

Figure 6.33 [12] seems to suggest that a very small strain occurs at 40 °C. If this strain is taken to equal 0.01%, then this implies that the wire would have indeed contracted by 0.026 mm at 40 °C.

On the other hand, just like all other metals, the SMA does have a thermal coefficient of expansion. Since, according to Figure 6.33, the SMA is still in its martensite phase at 40 °C, the thermal coefficient of expansion for **martensite** should be used in computing the SMA thermal expansion. Given that this coefficient is equal to 6.6×10^{-6} /°C, the SMA will expand by 0.120 mm. However, this expansion will cause the encoder to rotate in the clockwise direction, indicating that it is indeed elongating. Another factor that will contribute to the elongation of the SMA wire will be the thermal expansion of the cord to which it is attached and which runs over the pulley. The cord has a stainless steel core with a nylon shield. Since the thermal coefficient of expansion for stainless steel is smaller than that of Nylon, i.e. it expands less with heat, it will be this value that will be used to compute the expansion in the cord. Given that the thermal coefficient of expansion for stainless steel is 17.3×10^{-6} /°C and that the length of cord used is 0.250 m, the cord will expand by 0.303 mm.

The net "contraction" of the SMA wire is obtained by subtracting the sum of the all the "elongation" terms from the sum of all the "contraction" terms. Hence, the SMA wire will appear to have "contracted" by $0.638 + 0.026 - 0.120 - 0.303 = 0.241$ mm. Although this value is a little less than a third of the value obtained experimentally for the "contraction" of the SMA wire when only the ambient temperature was increased from −30 °C to 40 °C, both values have the same order of magnitude. In any case, if thermal expansion is indeed the cause behind this apparent contraction of the SMA wire, then a method will have to be developed to compensate for it.

Chapter 7

Conclusions & future work

The main goal of this research was to design and implement a controller that will actuate an SMA wire in approximately the same amount of time regardless of the ambient temperatures with a fixed load applied to it. Comparing the results of the *No Priming* strategy with the other strategies clearly indicates that the concept of priming does indeed help with wire actuation. This is because priming helps maintain the resistance of the SMA wire close to the cusp thus reducing TTC and AST across the different ambient temperatures.

With regard to the postulates formulated in Section 6.1, the best priming strategy lies between the *50%*Mtn_duty* and the *Minus 4.5%* strategies, with the former have consistently the lowest ASTs across the different temperatures and the latter having the smallest TTCs.

As for the actuation strategy, setting $Act\_duty = 150\%*Mtn\_duty$ did not yield consistent ASTs across the different temperatures. The focus of this work was on implementing and comparing priming strategies, and more work should also be done on modelling and developing actuation controllers to improve consistency.

Although *Peak Detector 1* was not found to be the best priming strategy, there is space for improvement. One modification would be to use a higher value for the maximum duty cycle output by the Bang-Bang controller. For example, set the upper limit of the Bang-Bang controller to a factor (greater than 1) times the *Mtn_duty*. However, care should be taken that this upper limit is not set too high to drive the SMA wire into spurious actuation while probing it.

One improvement to the experimental setup used in this work would be to remove the two power supplies and connect the circuit to an in-car battery. A very important aspect of car batteries that must be taken into consideration is

the fact that its voltage can vary rapidly between 9 V and 16 V. Thus, several precautions have to be taken. First of all, the maximum voltage that can be used to power the microcontroller is 12 V. Secondly, the ATD module of the microcontroller board operates at a maximum voltage of 5 V. Finally, some sort of feedforward signal indicating the instantaneous voltage of the car battery will be necessary in determining the duty cycle of the PWM signal that will be driving the SMA wire so as not to damage it while still providing appropriate power for control.

Another very important aspect about the in-car environment is noise. In the early stages of this research, an experiment was conducted to compare between the noise in the lab environment and that in the car. The car environment was found to be typically 10 times noisier than the in-lab environment. Therefore, extra measures may need to be taken to ensure that the noise on the signals collected, i.e. voltage and current, is as low as practically possible.

A final recommendation for future work would be to explore the use fuzzy logic in the control of SMA actuators. Fuzzy logic control is generally useful in applications where "human reasoning" has been shown to work. An interesting paper on this topic is the one written by Tafazola *et al.* [30] where they investigated the applicability of using a Sugeno-type fuzzy model based on subtractive clustering to model hysteresis inherent in SMA.

Fuzzy logic has several advantages: it is easy to implement, suitable for complex dynamic systems, highly flexible and robust in nature [31]. A further advantage in the design of fuzzy controllers is that human knowledge and a set of heuristic rules are implemented without the need for mathematical models [31]. Since the goal of this research is to control SMA actuation under varying ambient temperatures *without* the use of a model for the wire, the use of fuzzy logic may be appropriate.

As a preliminary investigation into this option, a hybrid controller, shown in Figure 7.1, incorporating a PI controller and a fuzzy inference system was developed to study the effectiveness of using fuzzy logic to control SMA actuation under varying wind conditions. Details of this investigation along with experimental results and conclusions are found in Appendix B.

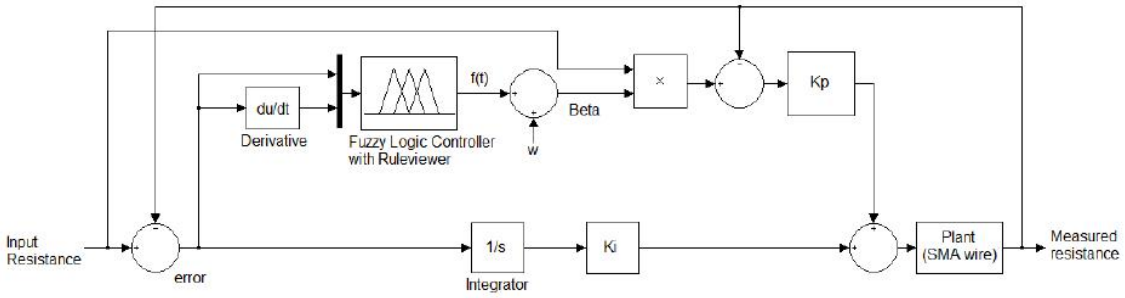

Figure 7.1: Proposed hybrid controller design

References

[1] J. M. Hollerbach, I. W. Hunter, and J. Ballantyne. A Comparative Analysis of Actuator Technologies for Robotics. pages 299–342, 1992. 1

[2] G. Song, B. Kelly, and B. N. Agrawal. Active Position Control of a Shape Memory Alloy Wire Actuated Composite Beam. *Smart Material Structures*, pages 711–716, August 2000. 1, 9, 10, 18, 19, 20, 24, 25

[3] J. W. Sohn, Y. M. Han, S. B. Choi, Y. S. Lee, and M. S. Han. Vibration and Position Tracking Control of a Flexible Beam Using SMA Wire Actuators. *Journal of Vibration and Control*, 15(2):263–281, 2009. 1, 9, 10

[4] J. L. Pons, D. Reynaerts, J. Peirs, R. Ceres, and H. VanBrussel. Comparison of Different Control Approaches to drive SMA Actuators. In *Proceedings of the 1997 8th International Conference on Advanced Robotics*, pages 819–824, July 1997. 1, 9, 10, 26

[5] K. Ikuta. Micro/miniature Shape Memory Alloy Actuator. In *Proceedings of the 1990 IEEE International Conference on Robotics and Automation*, volume 3, pages 2156–2161, May 1990. 2, 9, 10, 11

[6] H. T. Yee and R. Featherstone. An Architecture for Fast and Accurate Control of Shape Memory Alloy Actuators. *The International Journal of Robotics Research*, 27(5):595–611, 2008. 2, 27, 28, 29, 35, 96

[7] H. Goi and R. Gorbet. Report on Experiments Using Resistive Feedback to Control SMA Actuators. Technical Report TR-GM-0703, Department of Electrical and Computer Engineering, University of Waterloo, Waterloo, ON, September 2008. 4, 36, 37, 39, 47, 81, 99, 100

[8] C. DellaCorte, S. V. Pepper, R. Noebe, D. R. Hull, and G. Glennon. Intermetallic Nickel-Titanium Alloys for Oil-Lubricated Bearing Applications.

Technical Memorandum NASA/TM2009-215646, NASA Center for AeroSpace Information (CASI), Hanover, MD, March 2009. 7, 8

[9] C. Liang and C. A. Rogers. One-Dimensional Thermomechanical Constitutive Relations for Shape Memory Materials. *Journal of Intelligent Material Systems and Structures*, 1(2):207–234, 1990. 7

[10] SMA/MEMS Research Group. Shape Memory Alloys, 2001. http://www.cs.ualberta.ca/∼database/MEMS/sma_mems/sma.html [accessed on 14th November 2007]. 8, 9

[11] C. Mavroidis, C. Pfeiffer, and M. Mosley. Conventional Actuators, Shape Memory Alloys, and Electrorheological Fluids, 2001. http://www.resonancepub.com/actuator.htm [accessed on March 2nd, 2008]. 10, 11

[12] Dynalloy Inc. *Technical Characteristics of Flexinol Actuator Wires*. http://www.dynalloy.com/pdfs/TCF1140RevD.pdf [accessed on 3rd October 2009]. 10, 57, 72, 96, 122, 124

[13] M. A. Thrasher, A. R. Shahin, P. H. Meckl, and J. D. Jones. Efficiency Analysis of Shape Memory Alloy Actuators. *Smart Materials and Structures*, 3(2):226–234, 1994. 11

[14] R. B. Gorbet. *Control of Hysteretic Systems with Preisach Representations*. PhD thesis, University of Waterloo, 1997. 11, 22, 71

[15] N. Ma, G. Song, and H.J. Lee. Position Control of Shape Memory Alloy Actuators with Internal Electrical Resistance Feedback using Neural Networks. *Smart Materials and Structures*, 13(4):777–783, 2004. 11, 21, 22, 23, 24, 25

[16] C. A. Dickinson and J. T. Wen. Feedback Control Using Shape Memory Alloy Actuators. *Journal of Intelligent Material Systems and Structures*, 9(4):242–250, 1998. 11

[17] K. Kuribayashi. Improvement of the Response of an SMA Actuator Using a Temperature Sensor. *The International Journal of Robotics Research*, 10(1):13–20, 1991. 12, 13, 14, 15, 24, 25

[18] R. A. Russell and R. B. Gorbet. Improving the Response of SMA Actuators. In *Proceedings of 1995 IEEE International Conference on Robotics and Automation*, volume 3, pages 2299–2304 vol.3, May 1995. 13, 14, 15, 24, 26, 27

[19] K. Kuribayashi. A New Actuator of a Joint Mechanism Using TiNi Alloy Wire. *The International Journal of Robotics Research*, 4(4):47–58, 1986. 15, 25

[20] D. Grant and V. Hayward. Constrained Force Control of Shape Memory Alloy Actuators. In *Proceedings of the IEEE International Conference on Robotics and Automation*, pages 1314–1320, 2000. 15, 16, 24, 25

[21] S. B. Choi, Y. M. Han, J. H. Kim, and C. C. Cheong. Force Tracking Control of a Flexible Gripper Featuring Shape Memory Alloy Actuators. *Mechatronics*, 11(6):677 – 690, 2001. 16, 17, 18

[22] N. B. Kha and K. K. Ahn. Position Control of Shape Memory Alloy Actuators by Using Self Tuning Fuzzy PID Controller. In *Proceedings of the 2006 1st IEEE Conference on Industrial Electronics and Applications*, pages 1–5, May 2006. 20, 21

[23] B. K. Allston, A. M. Knebel, and M. R. Salemi. Method and Apparatus for Controlling a Shape Memory Alloy Fuel Injector, February 1 2000. U.S. Patent 6019113. 21, 23, 24, 29, 30, 32, 35

[24] B. Selden, K. Cho, and H. H. Asada. Segmented Shape Memory Alloy Actuators Using Hysteresis Loop Control. *Smart Materials and Structures*, 15(2):642–652, 2006. 26, 32, 33, 34, 35

[25] C. S. Loh, H. Yokoi, and T. Arai. Natural Heat-Sinking Control Method for High-Speed Actuation of the SMA. *International Journal of Advanced Robotic Systems*, 4(3):303–312, 2006. 30, 31, 32

[26] N. Ma and G. Song. Control of Shape Memory Alloy Actuators Using Pulse-Width Modulation. *Smart Materials and Structures*, 12:712–719, 2003. 37, 38

[27] J. E. Massad and R. C. Smith. A Homogenized Free Energy Model for Hysteresis in Thin-film Shape Memory Alloys. *Thin Solid Films*, 489(1-2):266 – 290, 2005. 71

[28] D. Madill and D. Wang. Modelling and L2-stability of a Shape Memory Alloy Position Control System. *IEEE Trans. Control Systems Technology*, 6(5):473–481, 1998. 72

[29] W. Ma, R. Gorbet, and J. Culham. Heat Transfer Modelling of SMA Wire in Air. Technical Report TR-GM-0902, Department of Electrical and Computer Engineering, University of Waterloo, Waterloo, ON, October 2009. 72

[30] S. Tafazoli, M. Leduc, and X. Sun. Hysteresis Modeling using Fuzzy Subtractive Clustering. *International Journal of Computational Cognition*, 4:15–27, September 2006. 126

[31] G. Mester. Neuro-fuzzy-genetic Controller Design for Robot Manipulators. In *Proceedings of the 1995 IEEE IECON 21st International Conference on Industrial Electronics, Control, and Instrumentation*, volume 1, pages 87–92 vol.1, Nov 1995. 126

APPENDIX A

A schematic digram of the circuit used in collecting data is shown in Figure A.1. Figure A.2 is a schematic of the same circuit with the addition of a protection circuit. This circuit prevents excessive voltage from being applied to the input pins of the OP484. When the circuit is powered up, but the actual experiment is not running, no current will be flowing through resistors R13 and R14. Consequently, 12 V will be applied to the OP484 input pins, which exceeds the chip's maximum input voltage. Thus, 1N752 (5.6 V) zener diodes are used to reduce the voltage applied to these pins to values below its maximum rating.

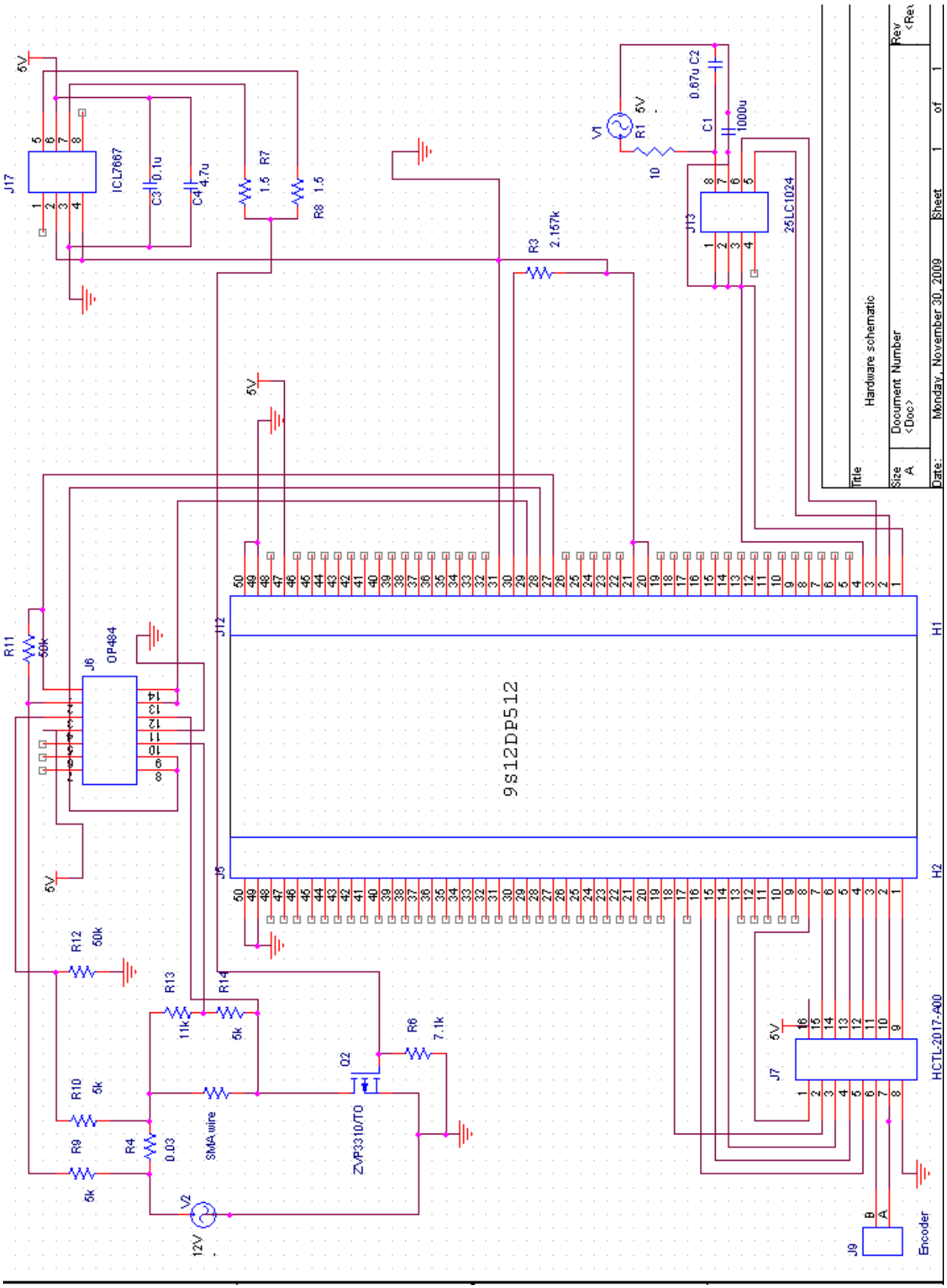

Figure A.1 Schematic diagram of circuit used to collect data

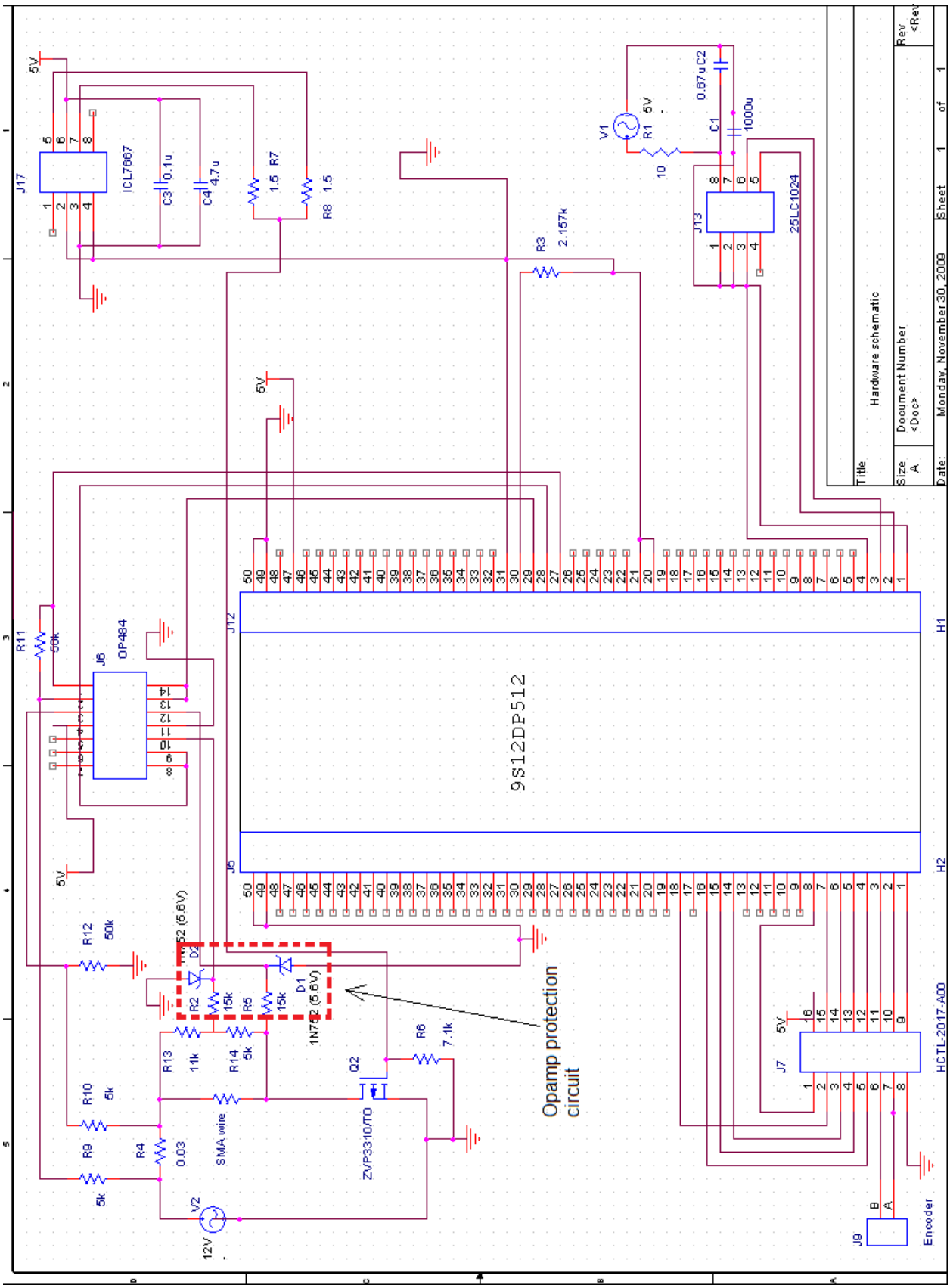

Figure A.2 Schematic diagram opamp protection circuitry

APPENDIX B

Controlling SMA actuators using a hybrid PI controller with a fuzzy inference system

Mohamed El Dib

Department of Electrical and Computer Engineering/Systems and Control
University of Waterloo
meldib@engmail.uwaterloo.ca

***Abstract*-Shape Memory Alloys (SMAs) have been implemented as actuators in a wide range of applications spanning several fields such as robotics, aeronautics, automotive and even in medicine. However, controlling these actuators is no simple task as they are considered to be highly nonlinear systems due to the hysteresis inherent in them. Several controllers, linear and nonlinear, have been designed and developed to control these SMA actuators. In this paper, a PI controller with a fuzzy logic system is introduced with the purpose of actuating the SMA wire in a consistent time period regardless of ambient air flow conditions. The results obtained are compared to a previous design that simply implemented a PI controller. Although the results obtained from the proposed controller were not better, they do indicate the plausibility of using fuzzy logic control in the control of SMA actuators as both sets of results are quite comparable. In fact, since the design of the fuzzy membership functions and fuzzy rule base were obtained by trial and error, the proposed design does show potential for even better results if the optimal solution can be found.**

Keywords: **Shape memory alloys, PI control, Priming, Fuzzy logic, Hysteresis**

I. INTRODUCTION

SHAPE memory alloys or SMAs are a group of metallic materials that demonstrate the ability of returning back to a previously defined shape or size if subjected to the appropriate thermal procedure. They exhibit two unique properties: shape memory effect and pseudo-elasticity. These properties are best described in terms of a solid state phase transformation that occurs in shape memory alloys due to a change in temperature. The two phases that make up the transformation are known as martensite and austenite.

The martensite phase exists at lower temperatures. In that phase, the molecules are arranged in a twinned structure. Thus, the SMA is relatively soft and can be easily deformed by applying a stress on it. If a stress is applied, the crystals become detwinned and the strain remains even after removal of the stress. On the other hand, the austenite phase exists at higher temperatures. The molecules in this phase tend to be arranged in a cubic structure. The molecular structure of the SMA at different phases is depicted in Figure 1.

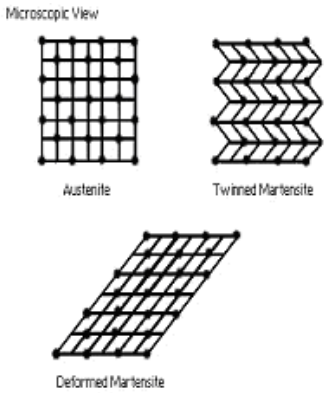

Figure 1 Crystalline structure of SMA when in austenite, twinned martensite and detwinned martensite (http://www.cs.ualberta.ca/~database/MEMS/sma_mems/sma.html)

The transformation of one phase into another is represented in terms of four temperatures: the martensite start temperature (M_s), the martensite finish temperature (M_f), the austenite start temperature (A_s) and the austenite finish temperature (A_f). As can be seen in Figure 2, the temperatures at which an SMA transforms from one phase to another depends on whether it is being cooled or heated. Consequently, this leads to the hysteresis inherent in SMA. Two factors determine the values of these four variables. The first factor is the amount of load placed on a shape memory alloy: as the load increases, the values of these four temperatures also increase. The second factor is the composition of the wire i.e. the percentages of the different elements making up the alloy.

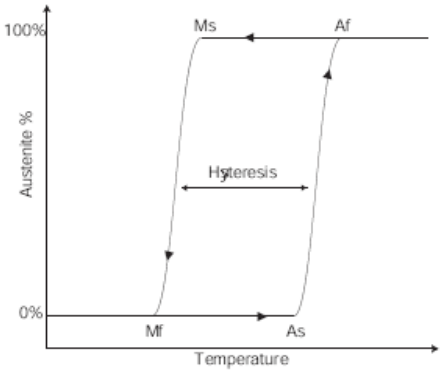

Figure 2 Hysteresis loop of an SMA [1]

The shape memory effect can be observed when the temperature of the SMA is below M_f. At this temperature, the alloy is composed entirely of martensite and therefore can be easily deformed by applying a load to it. By simply heating the alloy, it starts to transform from the distorted martensitic phase to the cubic austenitic phase. At temperatures above A_f the alloy is entirely austenite and the alloy has returned to its original shape. Figure 3 depicts the transformation from one phase to another based on the heating and loading that the SMA is subjected to.

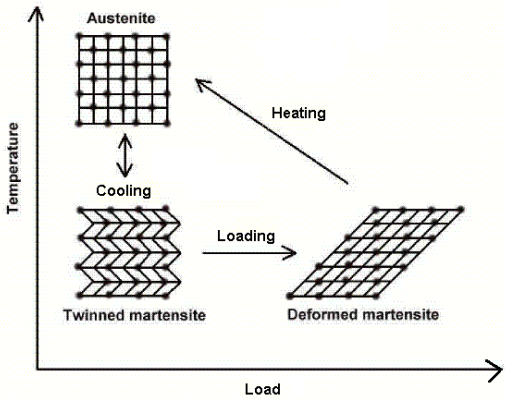

Figure 3 Shape Memory Effect of SMA [2]

The shape memory alloy is pseudo-elastic only when it is completely composed of austenite. Unlike the shape memory effect and as can be seen in Figure 4, pseudo-elasticity does not involve a change in temperature. If the load on the alloy is increased, a transformation from the austenite phase to the martensite phase takes place. The loading is absorbed by the softer martensite, but as soon as the loading starts to decrease, the alloy transforms back into austenite since the temperature of the wire is still above A_f.

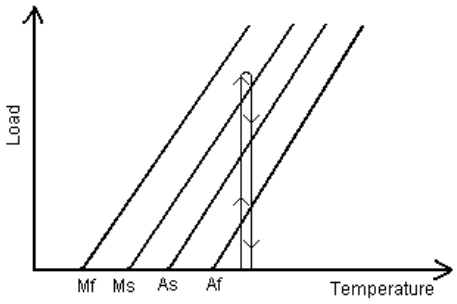

Figure 4 Pseudo-elasticity of SMA [2]

Shape memory alloys have several advantageous characteristics that have made it particularly attractive in the design of mini- or micro-actuators. Mavroidis et al. [3], Ikuta [4], Choi et al. [5], Pons et al. [6] and Song et al. [7] mention a number of these advantages:

- Simplicity of the control mechanism: the principle behind SMA actuation lies in the phase transformation of the alloy due to heating or cooling. This results in an extremely simple actuator system that can be easily miniaturized. This further reduces production costs and enhances reliability [3], [4], [5].
- Cleanliness: there is no safety hazard due to leakage of gases or fluids as in conventional hydraulic and pneumatic actuators. This makes it feasible to use in such fields as microelectronics, biotechnology and medical treatment [4].
- Silent actuation: no noise is produced during the phase transformation of SMAs [3], [4], [6].
- Self-sensing capabilities: the change in several material properties of SMA is related to the shape memory effect [4], [6].
- Low driving voltage: actuation of SMA wires requires low voltages. This enables the use of regular power supplies of 5V and 12V [4].
- High recovery stress (>500MPa) [7]: this enables SMA actuators to produce large forces [5].
- High strength-to-weight ratio making it suitable for miniature actuators [3], [6].

However, shape memory alloys have a number of drawbacks that continue to hamper the usefulness of SMA actuators in a wide range of applications. The first being the hysteresis in the phase transformation of SMA which makes it difficult to control SMA actuators [3], [6]. During phase transformation, energy is

dissipated due to internal friction and the creation of structural defects [3]. This results in hysteresis in the strain-temperature relationship. The second major disadvantage of SMA is its slow cooling response [6]. The time it takes an SMA element to go through an entire actuation cycle (heating and then cooling or vice versa) depends to a large extent on the heat transfer characteristics of the cooling system employed [3]. The bandwidth of SMA actuators is affected by a number of parameters: the temperature and type of the surrounding medium, the convection of the surrounding medium and the surface to volume ratio of the SMA elements [3]. Therefore, depending on the surrounding environment, heat dissipation might pose a problem. If, for example, the surrounding environment has low convection, then the rate of heat transfer to this medium is small resulting in a lower bandwidth. On the other hand, a high convection environment improves heat transfer increasing bandwidth. However, this occurs at the expense of more power needed to achieve the required actuation temperature [3]. Another disadvantage of SMA is their low energy effieciency. Given the temperature ranges where typical SMA actuators operate, the efficiency of a Carnot cycle does not exceed 10% meaning even lower energy efficiency for SMA actuators [3]. An additional disadvantage is the small absolute strains achieved by SMA [3]. With 8% strain being the typical maximum strain for most shape memory alloys, the design of applications creating large motions tend to be more challenging [3]. Another disadvantage is the short fatigue life which simply means that under high stress and heating rates, SMAs tend to experience a change in its properties [4].

In light of what was mentioned earlier regarding the fact that the duration of the SMA's actuation cycle is dependent on the heat transfer characteristics of the employed cooling system, this paper presents the design of a hybrid controller combining a PI-controller with a fuzzy inference system aimed at controlling SMA actuators and actuating them in a consistent time period regardless of the ambient air flow conditions.

II. CONTROL OF SMA ACTUATORS

Looking into the literature, we find that the task of controlling SMA actuators has attracted numerous researchers. Indeed, several techniques and designs have been proposed and tested in an attempt to overcome the nonlinearity inherent in SMAs. In [8], Dickinson et al. classify control techniques used for SMA actuation into two main categories: (1) open-loop control and (2) closed-loop feedback.

A. Open-loop Control

Open-loop control involves finding a model of the hysteresis loop in SMA, identifying its parameters and then inverting the model to remove or at least minimize the nonlinearity. Two techniques that have been widely used in open-loop control of SMA actuators include Neural Networks and the Preisach model of SMA.

Neural Networks

Neural networks have been used to model the hysteresis inherent in SMA. In their paper, Ma et al. [9] implemented a neural network which upon training, was used to model the relationship between electrical resistance and displacement of SMA actuators.

To enable them to use a neural network capable of accurately predicting the displacement as a function of the electrical resistance, Ma et al. [9] first conducted a number of experiments to investigate the electrical resistance-displacement relationship using a NiTi wire. They cited two very important reasons for carrying out such experiments: first of all, all previous research on the variation of electrical resistance of SMA actuators was conducted with the assumption that the temperature or stress was constant. However, in their experiment, Ma et al. [9] subjected the SMA wire to varying stress which they indicated to be normally the case in the majority of applications that use SMA actuators. The second reason was to provide a reference starting point for closed-loop control systems with electrical resistance feedback. This is particularly important as several factors affect the variation in electrical resistance. These factors include the heat treatment of the SMA wire, the percentage composition of each element in the alloy and the temperature and strain history of the wire.

The NiTi wire was actuated using a sine-wave, low frequency voltage signal to ensure full transformation of the SMA wire actuator. The tests were conducted to study the variation in electrical resistance in relation to varying activation conditions such as different pre-tensions, different stresses and different magnitudes of the input voltage.

To model the hysteresis between electrical resistance and displacement, Ma et al. [9] chose

one of the major loops, shown in Figure 5, that were produced by the open-loop experiments they carried out.

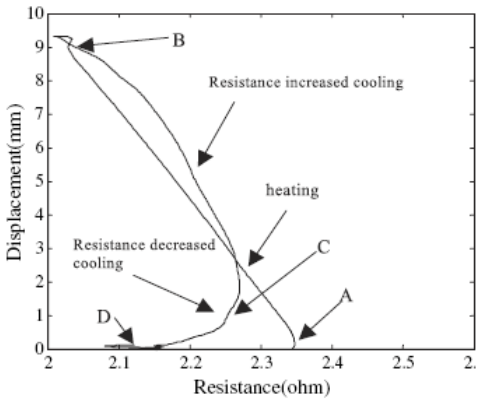

Figure 5 Major loop representing the electrical resistance hysteresis [9]

The relationship between the electrical resistance and the displacement for the above representative loop was modelled by a three-layer neural network with one hidden layer having eight neurons as shown in Figure 6.

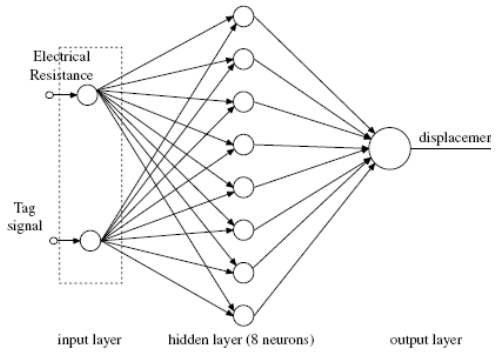

Figure 6 Structure of neural network [9]

Their control system takes two inputs: the electrical resistance of the SMA actuator and a 'tag' signal. Due to the hysteresis inherent in SMA wires, the electrical resistance value can correspond to more than one displacement value. Therefore, the representative loop is divided into 3 segments (AB, BC and CD) as shown in Figure 5. Segment AB has a negative slope that corresponds to the heating process. The BC segment has a negative slope that represents the resistance increase in cooling. In the same cooling process, CD has a positive slope. The 'tag' signal indicates a specific segment of the representative loop and thus, a corresponding single value for the displacement.

The training of the neural network is shown in the Figure 7.

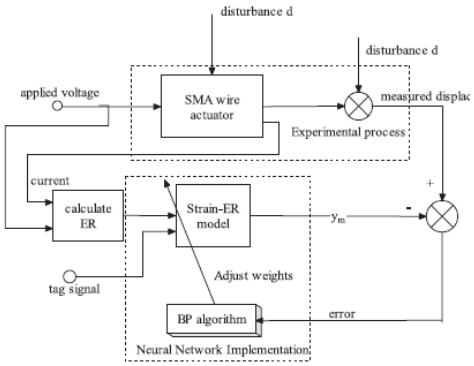

Figure 7 Training of the neural network [9]

Data from the representative loop, obtained from the open-loop experiments, was used in training the neural network. The electrical resistance of the SMA actuator is obtained by dividing the value of the applied voltage by the current flowing through the SMA actuator. The model of the electrical resistance-strain relationship outputs a certain displacement. The error between this value and the measured displacement is then fed into the Belief Propagation algorithm which 'infers' the strain of the SMA wire by adjusting the weights of the model. This is done iteratively until the produced output closely resembles the actual output. The closed-loop position control system designed by Ma et al. [9] can be seen in Figure 8.

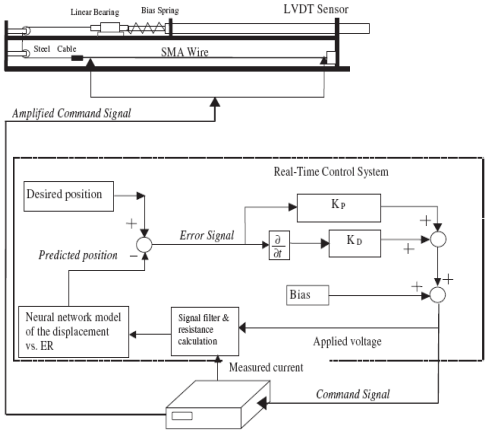

Figure 8 Closed-loop control system [9]

The error in the prediction made by the neural network is then fed into a PD controller which in turn, produces a control signal that gets amplified by a programmable power amplifier

before being applied to the SMA wire. The LVDT sensor that appears in the figure above was merely used Ma et al. [9] to verify the outputs from the neural network model.

After running several closed-loop experiments, Ma et al. [9] concluded that their proposed control scheme achieved accurate and stable position control thus eliminating the need for a position sensor.

Preisach Modeling

One of the most widely used open-loop controls of SMA actuators has been Preisach Modeling. Its hysteresis types despite its simple structure, the relative ease to invert and implement the model both in simulation and in experiment, its well-defined identification algorithm and its convenient numerical solution form [10].

However, for a given model to be categorized as being Preisach, it has to satisfy two very important characteristics: minor loop congruence and wiping-out property [10]. These two characteristics will be explained in more detail later in this section. I will be mainly discussing a version of the Preisach model called the "Classical" Preisach model. This model has its limitations and several extensions have been proposed to overcome them; however, they will not be discussed here.

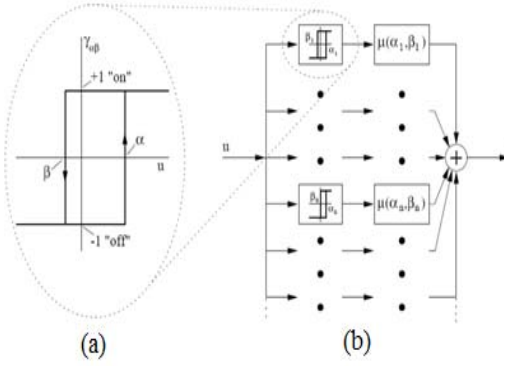

Figure 9 Preisach model [11]

The weighting of each relay is represented by μ(α,β). The α and β represent switching values that switch the relay between the horizontal segments of the relay with the condition that α ≥ β. These vertical segments are irreversible meaning that they can be only be traversed in one direction [11]. The horizontal segments however, are reversible and in the case that α = β, the relays are fully reversible and are called degenerate relays [11].

A very important aspect of the Preisach model is that it is only defined for continuous inputs u. As input varies with time, the output of each relay is adjusted according to the current input value. The weighted sum of all the relay outputs provides the overall system output, y, given by the following equation [11]:

$$y(t) = \iint_{\mathcal{P}} \mu(\alpha,\beta)[\gamma_{\alpha\beta}u](t)d\alpha d\beta.$$

Each relay is represented by a point in the α – β plane, also called the Preisach plane *P*.

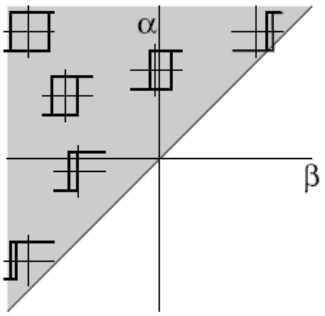

Figure 10 Preisach Plane [11]

Outside the hysteresis loop, the slope of the curve is 0. Therefore, if the domain of hysteretic behaviour is bounded by two input values u_- (negative saturation) and u_+ (positive saturation), then any input outside that domain has no effect on the output [11]. Since α must be greater than or equal to β as defined in the Preisach model, the lines $\alpha = u_+$, $\beta = u_-$ and $\alpha = \beta$ define the shaded triangle depicted in Figure 10.

The Preisach plane serves a very important purpose: it keeps track of the state of each individual relay [11]. This is done by first dividing *P* into two time-varying regions P_- and P_+ representing those relays that are in negative saturation and those relays that are in positive saturation respectively.

$P_-(t) \cup P_+(t) = P$ at all times t ('U' meaning union). In negative saturation, all relays are in the "-1" state and $P_- = P$ and $P_+ = 0$. If a monotonically increasing input is now applied, a relay will switch to the "+1" state as u increases beyond α (the right vertical segment in Figure 9(a)). The relay will now lie in P_+. The boundary between the two regions is represented by a horizontal line that moves upwards with increasing input. If the input starts decreasing monotonically, a vertical boundary is generated, moving from right to left switching relays from P_+ to P_- as the input passes the u = β (the left

vertical segment in Figure 9(a)) [11]. Continuing to reverse the input will result in more horizontal and vertical boundary segments. Given the boundary configuration that defines P_+ at time t and the weighting function μ, the output y(t) can be obtained using the following equation [10]:

$$y(t) = \iint_{\mathcal{P}_+} \mu(\alpha,\beta)\,d\alpha d\beta - \iint_{\mathcal{P}_-} \mu(\alpha,\beta)\,d\alpha d\beta$$

$$= 2\iint_{\mathcal{P}_+} \mu(\alpha,\beta)\,d\alpha d\beta - \iint_{\mathcal{P}} \mu(\alpha,\beta)\,d\alpha d\beta.$$

The Preisach model is generated by finding the weighting surface μ. This requires running experiments to collect data points through which "first order descending curves" are fitted. These curves are then differentiated to obtain an approximation of the weighting surface.

As mentioned earlier, a model is considered to be Preisach only if it satisfies the wiping-out and minor congruent loop characteristics [11]. The corners that may appear in the Preisach boundary are due to previous input extrema (whether increasing or decreasing). Thus, the Preisach boundary acts as the memory of the Preisach model [11]. The wiping-out property simply states that, by applying new input extrema, the effects of the previous input extrema can be removed or "wiped-out" from the memory of the model [11]. Suppose that the boundary at time t_0 is given in Figure 11(a) with the input equal to u_0. The corners in the boundary correspond to previous input extrema. If the input is now increased to a value u_1 that is greater than the previous input maximum, the corner in the boundary is "wiped out" as can be seen in Figure 11(b).

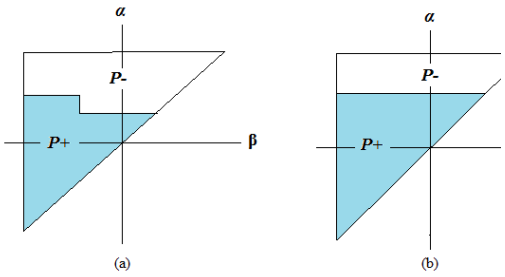

Figure 11 Wiping Property of Preisach Model

The congruent minor loop property, depicted in Figure 12, necessitates that all equivalent minor hysteresis loops be congruent [10]. Equivalence of minor loops means that they are generated by a certain input u varying monotonically between the same two extrema [10]. If after being shifted by an appropriate vertical translation one loop overlaps the other, then the two minor loops are congruent [10]. This vertical translation depends on the initial value of the input u.

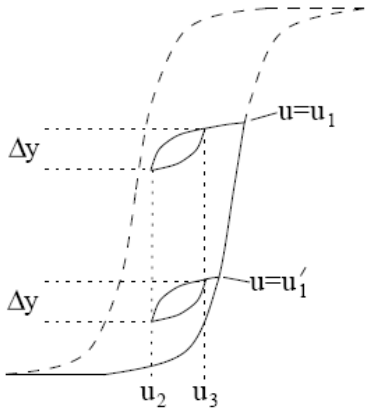

Figure 12 Congruent Minor loop property [11]

B. Closed-loop Control

Closed-loop control simply uses the difference between the output and the input, or error, to generate the corrective input. Elahinia et al. [12] divide the closed-loop control techniques that have been employed in the control of SMA actuators into three subcategories: (1) linear controls such as the traditional P, PI and PID, (2) PWM control and (3) nonlinear controls. In the following subsections, I will be discussing various examples of closed-loop control techniques spanning these three subcategories.

Linear Controls

The first closed-loop control techniques employed in the control of SMA actuators have been the traditional P, PI and PID controllers. In [13], the biped walking robot built by Hashimoto et al. used SMA actuators. They were able to control these actuators using PD controller. Ikuta et al. [14] used a PID controller to control the SMAs in an active endoscope. Madill et al. [15] used a P controller to control SMAs and demonstrated that it was L2-stable. However, it is known that with linear controllers, the gains have to be tuned on-line or through simulations by trial and error in order to achieve the required performance. Moreover, even if this is accomplished, slight disturbances to the system might dramatically deteriorate performance as the current set of control gains is no longer suitable and a new set of control gains has to be used. This is indeed the case with SMA wires as they are highly vulnerable to changes in their surrounding environment. In fact, Madill et al. [15] explicitly stated that they assumed that the

SMA wire was exposed to constant ambient temperature and that only natural convection cooled the wire. As a result, researchers started investigating other closed-loop control techniques that would be more robust in spite of parametric uncertainties, nonlinearity in the SMA model and external disturbances.

Control Using Pulse Width Modulation

An improvement made to typical linear controllers (e.g. PD) for the control of SMA actuators has been encompassing pulse width modulation in the design of the controller. PWM has several advantages. First, it is robust to any disturbances [16]. Second, it helps reduce the power consumption needed for actuation [16]. The fact that it can be easily implemented using microprocessors is also another important advantage.

In [16], Ma et al. designed a PW-modulated PD controller to control the position of SMA actuators. In order to make conclusions about the effectiveness of their proposed controller design, experiments were also conducted with a regular PD controller and a pulse-width-pulse-frequency (PWPF) modulated PD controller to compare results.

The design of the PW-modulator and PD controller was carried out in two steps. To begin with, Ma et al. [16] conducted several open-loop tests on the SMA actuator itself. The goal behind these tests was to investigate the impact of some of the actuator's properties, such as the response time and the maximum displacement, on the design of the PW-modulator and the PD controller [16]. The second step involved carrying out even more tests on the SMA wire but this time by actuating it using PWM signal. PWM parameters such as the duty cycle and frequency of the carrier signal were varied to identify the effect that each parameter has on the actuator's performance [16].

The PW-modulator implemented in [16] is depicted in Figure 13.

The PW-modulator employed in [16] is a one-way PW modulator. This means that it applies a sequence of voltage pulses to the SMA actuator only when there is a positive control signal. Otherwise, power to the SMA actuator is cut off by setting the output of the PWM signal to zero. The carrier wave generator was configured to produce a triangular wave of frequency equal to 10Hz. The amplitude of the carrier wave was chosen to be larger than the maximum amplitudes of the control signal. For the bang-bang trigger, its threshold was set to zero and its output was set to give PWM pulse amplitude of 0.075. This PWM signal was then passed

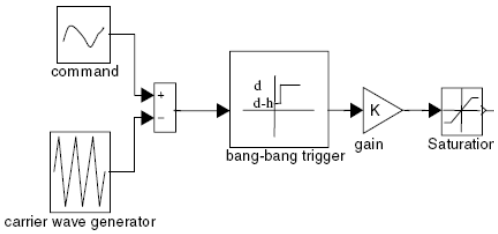

Figure 13 PW-modulator [16]

through a programmable power supply where it got magnified to 3.0V, the voltage needed to actuate the SMA wire. In order to achieve high energy efficiency and a quick response simultaneously, the duty cycle was made to range from 50% to 91%. As for the PD controller, the proportional and derivative gains were set to 0.51 and 0.07 respectively. The overall feedback control system is shown in the following figure.

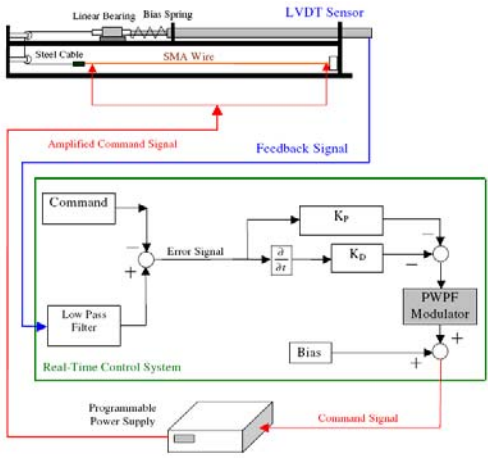

Figure 14 Feedback control system [16]

To verify the effectiveness of their controller design, Ma et al. [16] conducted the same experiments under the same conditions using PWPF-modulated PD control and continuous PD control. It was found that the PW-modulated PD controller achieved the most accurate position control and the least energy consumption among the three controllers [16]. Although, it had the longest settling time, no oscillations were observed in steady state as was the case with the other two types of controllers meaning that it added robustness to the system. This, they point out, is vital in the case of SMA actuators especially when they are exposed to an open

environment where they are susceptible to changes in convection conditions [16].

As was mentioned earlier, the use of linear controllers such as P, PI or PID controllers in the control of SMA actuators may give good performance for a certain range where the control gains are tuned. However, system performance degrades dramatically as these gains diverge away from that range. Since SMA actuators are inherently nonlinear due to hysteresis, several nonlinear controllers that are robust to system and environmental changes as well as modelling errors have been proposed. Examples of such nonlinear controls include fuzzy logic control, adaptive control and variable structure control which will be discussed in the next three subsections.

Fuzzy Modeling

An interesting paper particularly to the work presented here is the one written by Tafazola et al. [17]. In [17], Tafazola et al. investigate the applicability of using a Sugeno-type fuzzy model based on subtractive clustering to model the hysteresis inherent in SMA. For their fuzzy logic model, Tafazoli et al. [17] consider temperature to be the input and the SMA strain to be the output. They considered 1st and 2nd-order Sugeno models with the objective of finding the smallest possible set of if-then rules that will most closely model SMA hysteresis [17].

In developing their fuzzy logic model, Tafazoli et al. [17] started off by clustering their numerical data. They performed this by using Subtractive Clustering. This method has several advantages. Mainly, it is capable of automatically generating rules [17]. Another advantage is that each data point is considered a potential cluster centre. As a result, the size of the rule base is no longer dependent on the dimension of the problem [17].

The third advantage is that the fuzzy model identification algorithm is based on the cluster estimation method. Compared to other clustering algorithms where computation time grows exponentially with the dimension of the problem, this method does not involve any iterative non-linear optimization and thus, computation time grows only linearly [17]. After all the fuzzy clusters have been found and the fuzzy rules established, the latter are optimized by applying the Least Square Estimation method [17].

The second step was assuming an order of the Sugeno model. Tafazoli et al. [17] simulated both a first-order model and a second-order (quadratic) model. They then experimented with two different approaches to develop a fuzzy model for SMA hysteresis. The first approach, depicted in Figure 15 below, is called the "Mirror Image" approach [17]. It produces a continuous hysteresis curve mirroring the lower curve and then adding it to the end of the upper curve. The lower curve is mirrored around the rightmost input temperature value and the input range is then increased accordingly.

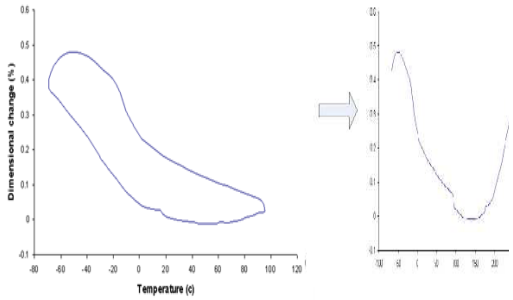

Figure 15 Mirror Image approach [17]

The second approach is called the "Separation" approach and is shown in Figure 16. Its name arises from the fact that the hysteresis curve is separated into an upper curve and a lower curve sharing a single data point to allow continuity of the model [17].

In order to make conclusions on the usefulness of their fuzzy logic model, Tafazoli et al. [17] compared it to a neural network-based model. When the "Mirror Image' approach was employed, the linear fuzzy logic model required 12 rules to model SMA hysteresis whereas the quadratic model required only 7 [17]. With the "Separation" approach, modeling the upper curve (resembling heating) of SMA hysteresis with a linear model required 6 rules whereas the quadratic one needed 4. The lower curve (resembling cooling) was modeled using 6 rules with a first-order model and only 2 with a second-order or quadratic model [17]. In all cases, the quadratic Sugeno models were found to achieve better or comparable performance compared to the linear models using a smaller number of rules, and overall, fuzzy models performed better than neural networks in terms of modeling the strain-temperature relationship in SMAs regardless of the approach (whether "Mirror Image" or "Separation") used and the order of the model employed [17].

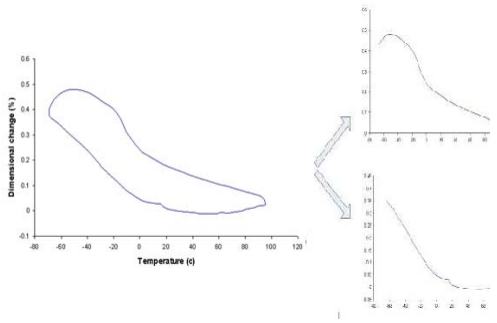

Figure 16 Separation approach [17]

Adaptive Control

Adaptive control is another nonlinear control technique that has been extensively implemented by researchers. The essence of adaptive control is an adaptation algorithm that modifies controller gains as a function of a system's operating conditions [18]. This is particularly useful in the control of SMA actuators as they are very sensitive to small changes in the surrounding environment.

In their paper, Dickinson et al. [8] discuss how they were able to control a flexible beam using an externally attached SMA wire at the tip of the beam. This was actually an extension to an earlier work performed by Dickinson et al. [10] where they demonstrated that using a proportional force feedback to control an SMA wire fixed between rigid surfaces rendered the closed loop system stable. However, when the same controller was applied to an SMA wire connected to a flexible beam, the system was unstable. In [8], Dickinson et al. devised an adaptive controller and proved that the SMA-flexible beam system was stable under the Circle Criterion.

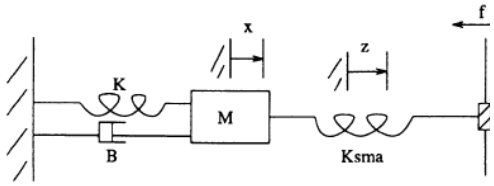

Figure 17 The SMA-flexible beam system modeled as a mass-spring-damper system [8]

The model for the entire system (SMA wire plus flexible beam) is depicted in Figure 17. It consists of a lumped model for the SMA connected to a mass-spring-damper system representing the flexible beam. The SMA wire's lumped model approximates the relationship between the rate of change in temperature of the SMA wire and convective cooling and resistive heating. This model is given by the following formula:

$$\dot{T} = -\alpha(T - T_r) + \beta u^2$$

where **α** represents the cooling coefficient, **T** the temperature of the SMA wire, $\mathbf{T_r}$ the room temperature, **β** the heating coefficient and **u** the current flowing through the SMA wire [8]. The dynamic equation of the beam is given by:

$$M\ddot{x} + B\dot{x} + Kx = f$$

Whereas **x** represents the horizontal displacement of the flexible beam, **f** represents the force applied by the SMA wire on it. The relationships between strain **ε**, stress **σ** and temperature T is given by the following 3 equations [8]:

$$\varepsilon' = H\xi$$

$$\sigma = \frac{f}{A}$$

$$\sigma H + \frac{1}{2}\Delta s \sigma^2 + \Delta\alpha_1 \sigma(T - T_r) + \rho\Delta s_0 T - \rho b\xi - Y^{**} = 0$$

The last equation depicts the hysteresis in shape memory alloys. The internal displacement of the SMA wire due to phase transformation is denoted by **z** and is related to stress, strain and temperature through a general hysteresis function given by the following equation:

$$z = g(T, \varepsilon, \sigma) = \begin{cases} g_u(T, \varepsilon, \sigma), & \dot{T} > 0 \\ g_d(T, \varepsilon, \sigma), & \dot{T} < 0 \end{cases}$$

The $\mathbf{g_u}$ and $\mathbf{g_d}$ functions are monotonically increasing with $\mathbf{g_u}$ lying strictly below $\mathbf{g_d}$ for the entire temperature range of T [8]. More details on these equations and the different parameters can be found in [8].

In [10], Dickinson et al., using simple proportional feedback and having both ends of the SMA wire fixed to rigid surfaces, were able to render the closed loop system stable provided that the proportional gain k was kept small. However, Dickinson et al. [8] note that this will cause a problem when controlling a flexible beam as it will not be feasible to tune k for every

beam deflection required. Therefore, they proposed an adaptation strategy that estimates the desired deflection x_d. The idea behind the adaptation strategy was that if the beam deflection x, is less than the steady-state deflection x^* (note that from their experiments, Dickinson et al. [8] found that x will never reach x_d but rather reaches a steady-state deflection x^*), then x_d should increase. On the other hand, if x is greater than x^* then x_d should decrease. Therefore, the desired beam deflection estimate $\hat{x}_d$ is given by:

$$\dot{\hat{x}}_d = -\gamma(x - x^*)$$

where γ represents the gain of the adaptation block. The overall control system encompassing the adaptation strategy is depicted in the figure below:

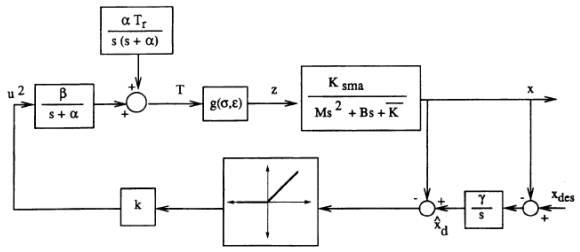

Figure 18 Feedback control system with adaptation scheme [8]

The closed loop system can be described by the following state-space equations:

$$\dot{X} = AX + BV$$

$$Y = CX$$

$$V = \phi(Y) = -(g(Y + T^*, \varepsilon, \sigma) - g(T^*, \varepsilon^*, \sigma^*))$$

where X, A, B and C are matrices given by [8]

$$X = \begin{bmatrix} \delta T \\ \delta x \\ \delta \dot{x} \\ \delta x_d \end{bmatrix}, \quad A = \begin{bmatrix} -\alpha & -\beta k_s & 0 & \beta k_s \\ 0 & 0 & 1 & 0 \\ 0 & -\frac{K}{M} & -\frac{B}{M} & 0 \\ 0 & -\gamma & 0 & 0 \end{bmatrix}$$

$$B = \begin{bmatrix} 0 \\ 0 \\ -\frac{K_{sma}}{M} \\ 0 \end{bmatrix}, \quad C = [1 \quad 0 \quad 0 \quad 0]$$

Given that the matrix A has 4 eigenvalues (3 in the open left-half plane and one at the origin) and given the Nyquist plot of the system's transfer function $G(s) = C(sI - A)^{-1}B$ shown in Figure 19, Dickinson et al. [8] were able to prove that the closed loop system was globally asymptotically stable using the Circle Criterion provided that k and γ were chosen to be sufficiently small.

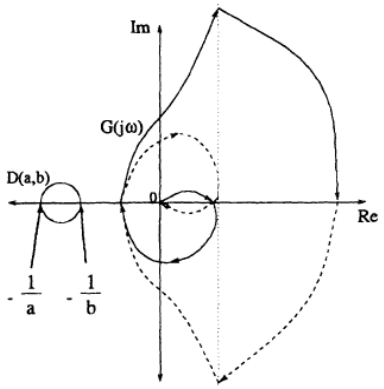

Figure 19 Nyquist plot of overall control system [8]

Variable Structure Control

Variable structure control is another nonlinear technique that has been widely used in the control of SMA actuators. It is a high-speed switching feedback controller that utilizes what is known as "sliding motion" to control nonlinear systems [18]. In other words, it can be thought of as an algorithm that switches between a set of predefined linear or nonlinear controllers as the state of the system varies. The "sliding motion" refers to this switching between the different controllers. The goal of each controller is to drive the system to a desired state. In the case of position control for example, the switching surface can be the desired position. The design of variable structure control therefore, consists of constructing the switching surfaces and the design of maximum feedback gains that will drive the system's state to these surfaces infinitely fast (ideal case) [18]. However, stability becomes an issue when using the maximum gain for high-speed switching [19]. For small disturbances, the maximum feedback gain may result in oscillatory behaviour or even instability in the system. Therefore, care has to be taken in choosing gains that are large enough to drive the system to the sliding surface as quickly as possible but without causing it to oscillate or become unstable [19].

What is most appealing about variable structure control is that relatively few physical parameters of the plant to be controlled need to be known to develop a controller design [19]. Another

advantage is its insensitivity to parameter variations [19]. This is particularly useful in controlling SMA actuators given the difficulties faced when modeling it. The major disadvantage of variable structure control however, is that it suffers from chattering [18]. This refers to the finite amount of time it takes to switch between the different controllers preventing the system from displaying ideal behaviour. Nevertheless, such a problem can be somewhat improved by introducing smooth switching laws or boundary layers close to the sliding surfaces [19].

This method of nonlinear control design was adopted by Grant et al. [19] in controlling a novel shape memory alloy actuator consisting of several thin NiTi fibers woven in a counter rotating helical pattern around supporting disks as shown in Figure 20. Given the fact that SMA wires have the drawback of achieving limited strain, the goal behind developing this new actuator was to achieve displacement amplification [19].

In [19], Grant et al. developed a two-stage variable structure controller, shown in Figure 21, that uses three different constant-magnitude pulses for the control of the SMA actuator. Two of the three constant amplitude current values are used depending on the error between the desired position and the measured position of the actuator. When the error is large, the actuator is driven with a high value current to bring the system quickly to the switching surface. As the error is reduced and approaches zero, a lower current value drives the system to prevent it from oscillating or becoming unstable. This achieves the two objectives mentioned earlier: quick response and stability [19]. The third current value was added to the controller as an indication as to whether the actuator was extended or contracted. The authors stated that this helped reduce the oscillation about the neutral position [19]. Grant et al. [19] conclude by stating that their variable structure control system actually yielded satisfactory results as it was able to accurately track step, triangular and sinusoidal waves.

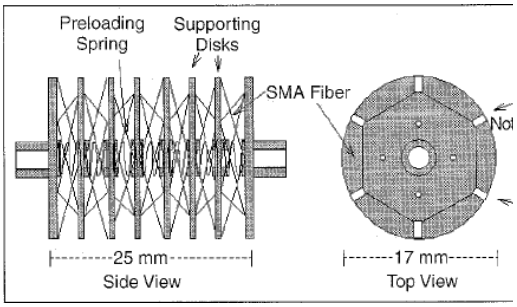

Figure 20 SMA actuator proposed by Grant et al. [19]

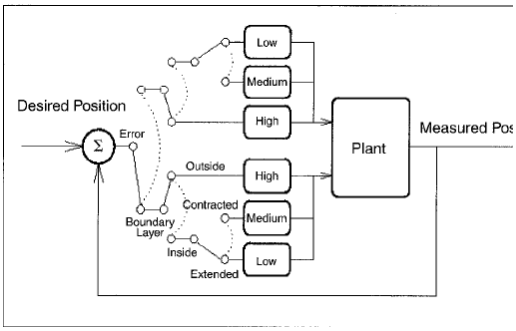

Figure 21 Two-stage variable structure controller proposed by Grant et al. [19]

III. FUNDAMENTALS OF PI AND FUZZY LOGIC CONTROL

A. PI control

A PI controller is composed of a proportional, P, controller and an integral, I, controller. The proportional controller simply multiplies the difference between the input signal and the output signal, or the error. It is denoted by the following expression:

$$u_p(t) = K_p\big(r(t) - y(t)\big) \tag{1}$$

where $u_p(t)$ represents the control variable, K_p the proportional gain, r(t) the reference input signal and y(t) the process output signal. While the proportional drawback has the advantage of reducing the rise-time by increasing the proportional gain, it does so at the expense of a steady-state error.

The integral action consists of a gain, K_i, that multiplies the integral of the control error:

$$u_i(t) = K_i \int_0^t e(\tau)d\tau \tag{2}$$

As can be seen from the equation (2), the control variable $u_i(t)$ is a function of the past values of the control error. The fact that the integral action introduces a pole at the origin of the complex plane in the frequency domain reduces the steady-state error to zero when a step reference signal is applied [21]. Therefore, implementing a PI controller will help solve the two major problems of oscillatory behaviour and steady-state error which would have detrimental effects on the control of the SMA actuator system.

B. Fuzzy logic

Fuzzy logic control, which was developed by Dr. Lotfi Zadeh in 1965, is generally useful in applications where "human reasoning" has been shown to work. In crisp set theory, an element either belongs to a set or not. In other words, it either has a membership of 1 or 0. However, in Fuzzy Set Theory, an element may partially belong to a given set and therefore its degree of membership may vary over the range [0,1]. Thus, a fuzzy set is represented by a membership function and it is these membership functions that help in developing rules that approximate human IF:THEN statements.

In the design of fuzzy controllers, human knowledge and a set of heuristic rules are implemented without the need for mathematical models [18]. A fuzzy logic system consists of four major components: 1) a fuzzifier used to transform crisp input values from a process into fuzzy sets, 2) a rule base composed of a set of linguistic description "IF-THEN" rules, 3) an inference engine that applies the set of rules in the rule base to the inputs to identify one or more outputs and 4) a defuzzifier which transforms back the fuzzy sets into crisp control signals [18] [20].

Indeed, fuzzy logic has several advantages: it is easy to implement, suitable for complex dynamic systems, highly flexible and robust in nature [18]. However, it does suffer from two major disadvantages. First, it is difficult to obtain optimal fuzzy rules and membership functions. Second, it does not have any learning capability [18].

IV. PROBLEM

Actuation of SMA wires is affected by two factors: changes in temperature and varying stress. This is made evident by the shape memory effect and pseudoelasticity which are important characteristics of all shape memory alloys. Thus, the ultimate goal of this work is to design and implement a controller that will actuate an SMA wire in a consistent time regardless of the ambient air flow conditions while fixing the stress that the SMA wire is subjected to.

This can achieved by making use of a very well-known fact of SMAs: during heating, their resistance increases to a maximum value or cusp prior to contraction then decreases to a lower austenite resistance value. The change in SMA's resistance during heating is depicted in Figure 22.

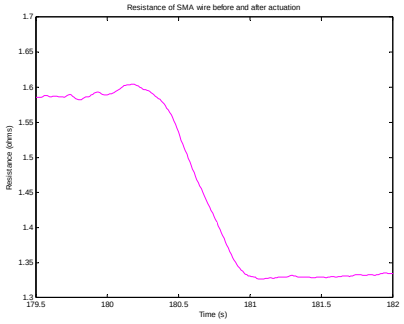

Figure 22 Resistance reaches a cusp at the onset of actuation

Therefore, if a controller design can be developed that varies the current used in pre-heating the SMA wire so that its resistance is at its maximum value prior to actuation, then it is possible to actuate the wire in a consistent time period regardless of the ambient air flow conditions without the danger of overheating it. This process will be called "priming".

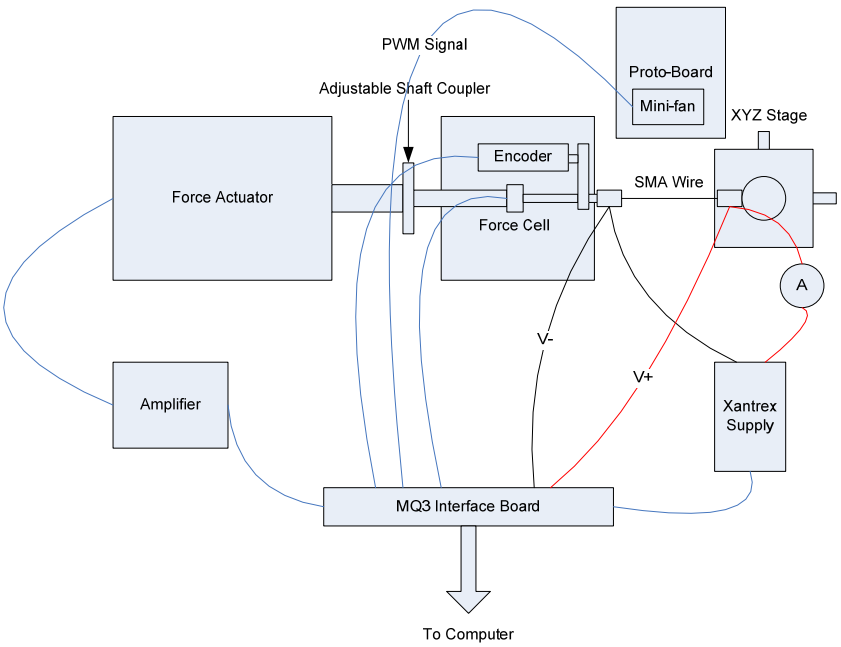

Figure 23 Block diagram of experimental setup

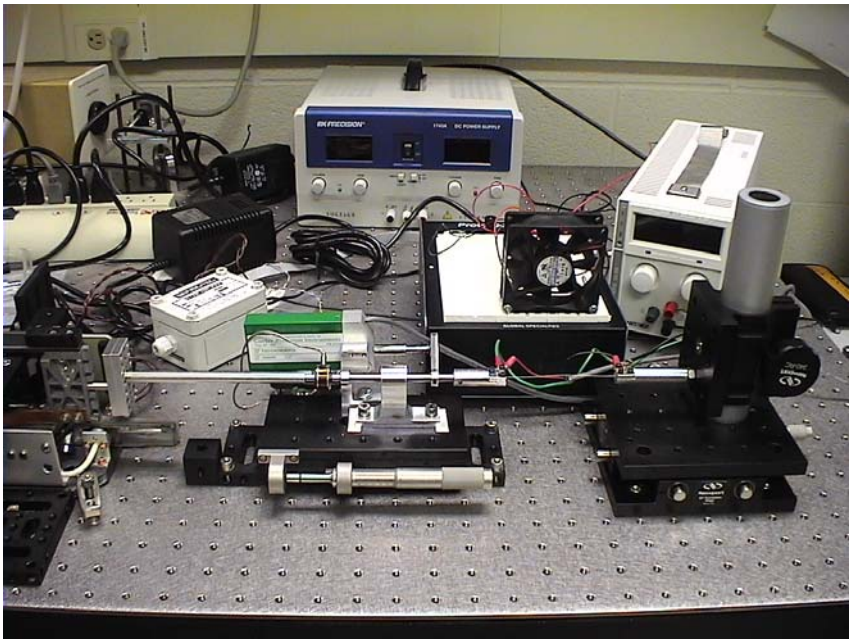

Figure 24 Actual photo of experimental setup

V. Experimental Setup

Figure 23 depicts the block diagram of the experimental setup while Figure 24 provides an actual picture of the equipment used.

The major components of this experiment include a Xantrex XPD 33-16 programmable power supply, a Newport 443 Series linear stage, a 250µm 90°C Flexinol wire from Dynalloy, a Quanser MultiQ3 data acquisition board, a Data General 6070 Force Actuator, an EG&G Current amplifier for the force actuator (model CO502-001), a Honeywell Sensotec Force Cell (model AL311 101b), Ball Bearing Optical Shaft Encoder from US Digital (model H5-1024-I-S), a Jamicon 12V 0.15A rotary DC mini-fan, and a PC loaded with MATLAB/Simulink.

As can be seen in Figure 23, one end of the SMA wire is fastened to the XYZ stage while the other end is fastened to a clamp that is connected

to the force cell and the encoder. The Xantrex power supply, the force actuator (through the current amplifier), the force cell, the encoder and the mini-fan are all interfaced to the MQ3 card.

Experiments with a sampling frequency of 100Hz are built in MATLAB/Simulink and compiled for the Real-Time Windows Target using Real-Time Workshop. They are then executed in real-time on the hardware via the MultiQ3 (MQ3) interface board. The force cell has an independent closed-loop force controller that applies forces on the SMA wire using feedback from the Honeywell Sensotec force sensor. The austenite length of the SMA wire is hand measured with a micrometer while it is heated under zero-load. The encoder count is then divided by this length to yield strain. The Xantrex power supply is configured to operate in voltage-control mode and is controlled remotely via an analog output channel on the MQ3 card. The power supply outputs a current that heats up the SMA wire. This current is measured via a built-in current monitor signal in the Xantrex using an analog input channel on the MQ3 card. Voltage across the SMA wire is also measured independently using a separate analog input channel on the MQ3. All these signals are then fedback to the Simulink model for analysis. Resistance is calculated in software by dividing the voltage and current measurements. The mini-fan is placed directly in front of the SMA wire and is used to provide varying convection coefficients. It is controlled programmatically from Simulink through an analog output channel on MQ3.

VI. Original PI Controller Design

In the original design, a typical PI controller was used to determine the priming current to be supplied to the SMA wire.

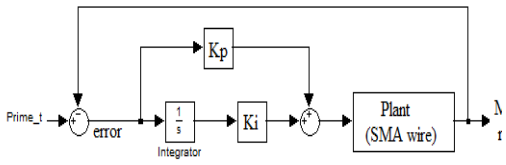

Figure 25 Original PI controller design

A sample experiment was first run, with the priming process disabled, to determine the maximum value of the wire's resistance just before it actuates (i.e. undergoes contraction) which was found to equal 1.588 Ω. This resistance value was denoted by Prime_t. The experiment was then run again, this time enabling the priming process, and the error between Prime_t and the actual measured resistance of the wire formed the input to the PI controller. The purpose of using the PI controller was to act as a servo controller servoing around Prime_t. Thus, if the measured resistance dropped below Prime_t, the PI controller kicks in increasing the value of the priming current to bring the resistance value back up again. The best results were obtained with $K_i = 10$ and $K_p = 10$.

However, there is a paradox involved. Resistance decreases below Prime_t in two situations: when the wire cools naturally without actuating, and when the wire actuates. In the latter case, increasing the value of the priming current will not increase the resistance back to Prime_t. Consequently, not knowing the cause in the decrease of the resistance value forced us to use servo controllers that erred against the conservative side to guard against spurious actuation. This was one problem we aimed to solve by incorporating fuzzy logic into the controller design that will be described in the next section.

VII. Proposed Hybrid Controller Design

In this paper, a hybrid controller is proposed combining a PI controller and a fuzzy inference system. The fuzzy set-point weighting design introduced by Visioli in [21] was adopted. In fact, Visioli [21] introduces the design of fuzzy module in conjunction with PID control. In the design of the proposed controller, the derivative action was dropped yielding a PI controller.

According to Visioli [21], a typical problem with designing a feedback controller like the one presented in this paper is achieving high performance in both reference-signal-following and load rejection disturbance simultaneously. He states that this problem can be solved by designing a two-degree-of-freedom control architecture combining both feed-forward and feedback control laws [21]. Visioli [21] achieves this by weighting the reference signal, r(t), for the proportional action which gets defined as follows:

$$u(t) = K_p\left(\beta r(t) - y(t)\right) \tag{3}$$

where $0 \le \beta \le 1$.

The transfer function of the overall PI controller is given by the following equation:

$$C(s) = K_p\left(\beta + \frac{1}{T_i s}\right) \quad (4)$$

where T_i is the integral time constant. As can be seen from Equation (4), the load disturbance rejection task, resembled by $\frac{1}{T_i s}$, is independent of the weight β and at the same time decoupled from the reference-signal-following one. Thus, the PI parameters can be tuned to achieve high load disturbance rejection performance while β can be fine tuned separately to improve the reference-signal-following performance.

Thus, Visioli [21] suggests that the set-point technique would be a good solution to implement in applications where both specifications (load disturbance rejection and set-point following) are of major importance. This is indeed the case with the problem in hand as we set to achieve two goals: 1) supply the priming current that will maintain the resistance value at its maximum (set-point following) and 2) maintain priming without falling into spurious actuation (i.e. reduce the oscillatory behaviour of the priming current).

Fuzzy set-point weighting is brought about by adopting a fuzzy inference system that determines the value of the weight β(t) depending on the current value of the system error e(t) and its derivative $\dot{e}(t)$ [21]. The idea is rather simple: β is increased when the difference between the process or plant output y(t) and the reference signal r(t) is large, and decreased when the difference between them is small [21]. Regarding the problem discussed in this paper, the plant output y(t) will be the desired maximum resistance value Prime_t and the system error e(t) resembles the difference between them.

Figure 26 depicts the design of the proposed controller.

The fuzzy inference system has two inputs: the difference between Prime_t and measured resistance of the SMA wire or the error e(t) and its derivative $\dot{e}(t)$. The fuzzy set-point technique is implemented in such a way that the output of the fuzzy module f(t) is added to the constant parameter ω resulting in the coefficient β(t) that multiplies the set-point which in this case is Prime_t.

The fuzzy set-point weighting technique involves the tuning of the following parameters: K_p, K_i and ω. Moreover, performance can be further improved by modifying the peak values of the membership functions and the fuzzy rules. All these fuzzy inference system parameters were tuned by following the procedure that Zheng outlined for fuzzy controllers in [22].

With trial and error, the parameters of the final design of the proposed controller were assigned the following values: K_p = 15, K_i = 80 and ω = 0.3. The two input signals, e(t) and $\dot{e}(t)$, and the output signal, f(t), each had 3 membership functions as depicted in Figure 27.

e(t) ranged from -0.03 to 0.3 and consisted of 3 membership functions: ZO (Zero), PS (Positive Small) and PB (Positive Big). $\dot{e}(t)$, ranging over -0.3 to 0.15, had N (Negative), ZO (Zero) and P (Positive) as its membership functions. The output f(t) ranged from -0.3 to 0.7 with 3 fuzzy sets: N (Negative), ZO (Zero) and P (Positive). A Mamdani fuzzy inference system was used with the Centroid of Area method as the defuzzification process. The fuzzy rule set consisted of the following 9 rules:

1) IF e(t) is PB AND $\dot{e}(t)$ is N, THEN f(t) is P
2) IF e(t) is PB AND $\dot{e}(t)$ is ZO, THEN f(t) is P
3) IF e(t) is PB AND $\dot{e}(t)$ is P, THEN f(t) is ZO
4) IF e(t) is PS AND $\dot{e}(t)$ is N, THEN f(t) is P
5) IF e(t) is PS AND $\dot{e}(t)$ is ZO, THEN f(t) is ZO
6) IF e(t) is PS AND $\dot{e}(t)$ is P, THEN f(t) is N
7) IF e(t) is ZO AND $\dot{e}(t)$ is N, THEN f(t) is ZO
8) IF e(t) is ZO AND $\dot{e}(t)$ is ZO, THEN f(t) is ZO
9) IF e(t) is ZO AND $\dot{e}(t)$ is P, THEN f(t) is ZO

The proposed rule base is also depicted in Table 1.

e\ $\dot{e}(t)$	N	ZO	P
PB	P	P	ZO
PS	P	ZO	N
ZO	ZO	ZO	ZO

Table 1 Proposed Rule Base

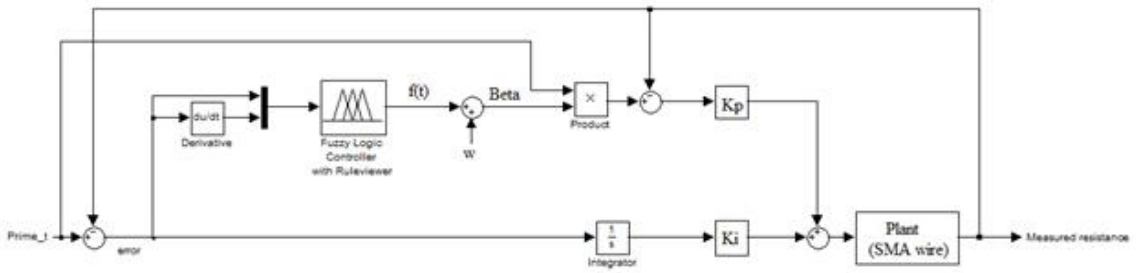

Figure 26 Proposed Hybrid Controller design

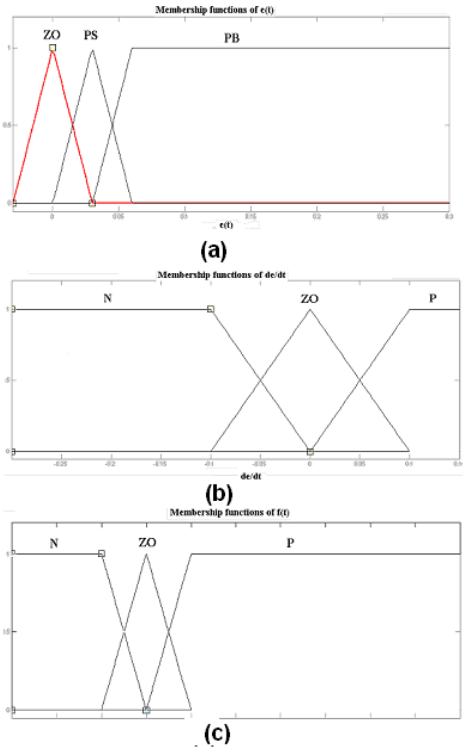

Figure 27 Membership functions of (a) e(t) (b) de/dt and

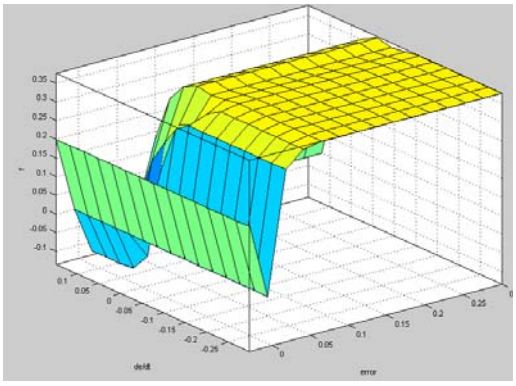

Figure 28 Control surface of proposed fuzzy logic system

VIII. EXPERIMENTAL RESULTS

Three sets of experiments were carried out. The first set of experiments involved no priming process. This served as a control experiment to demonstrate the effectiveness of using priming. The second set used the old controller design based on the PI control alone. The third set tested the feasibility of the proposed hybrid controller. In each set of experiments, the mini-fan was used to subject the SMA wire to three different wind conditions: Fans Off, Mini-Fan at 50% Duty Cycle (MF50) and Mini-Fan at 100% Duty Cycle (MF100). The wind speeds were measured using a Kestrel 1000 hand-held anemometer. The wind speed produced by MF50 was about 0.4 - 0.5m/s and the wind speed produced by MF100 was about 1.1 – 1.2m/s.

To be able to compare the effectiveness of the proposed hybrid controller versus the original PI controller design, two measures were defined: Time-to-Cusp (TTC) and Absolute Strain Time (AST). TTC is defined as the time from the start of the actuation period to the cusp. The shorter the TTC the more effective the controller design is. AST is defined as the time needed to contract the SMA wire to 1% strain from the start of the actuation period. The goal is to obtain a consistent AST under all wind conditions. One should note that this measure favours the priming controller design that causes more pre-actuation contraction.

The TTC and the AST are both functions of the average priming current and actuation current. With TTC, a higher priming current generally means that the resistance values will be closer to Prime_t prior to actuation. Moreover, a higher actuation current means that resistance values will rise faster to the maximum value Prime_t after actuation. Since AST includes TTC, it will also depend on both the priming current and the actuation current. Furthermore, a higher

actuation current would cause the SMA wire to contract faster reducing AST.

Due to noise and other real-world limitations, one would not expect the priming current and the actuation current to be uniform across the experiments with the same wind conditions, and indeed they are not. However, in order to make comparisons between the proposed hybrid controller and the original PI controller the following two postulates were formulated:

P1. A smaller or equal TTC given a lower actuation current implies a better priming controller design since a higher actuation current generally leads to a smaller TTC.

P2. A smaller or equal AST given a lower actuation current implies a better priming controller since a higher actuation current generally leads to a smaller AST. Since all the experiments use the same actuation strategy, the smaller AST must be the result of better priming.

Figures 29 and 30 show examples of TTC and AST respectively.

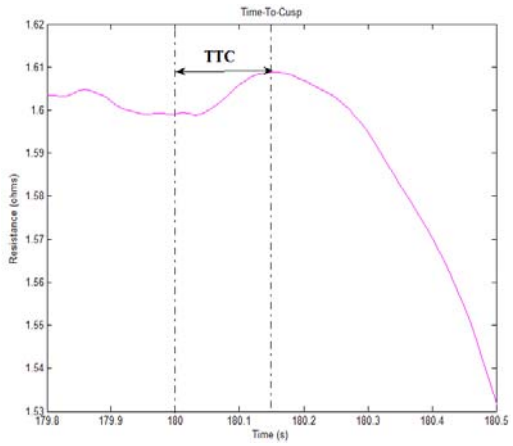

Figure 29 Time-To-Cusp (TTC)

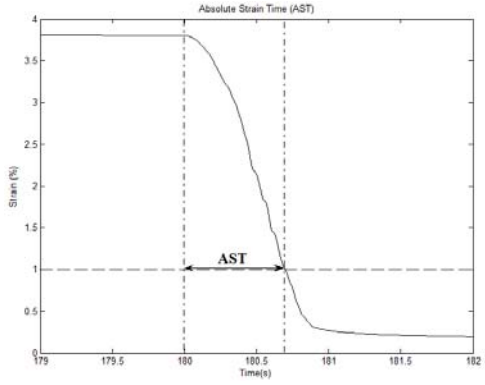

Figure 30 Absolute Strain Time (AST)

For the experiments, all the trials used the same timing sequence, force profile, initialization procedure and ending procedure. An example of an experimental trial is shown in Figure 31.

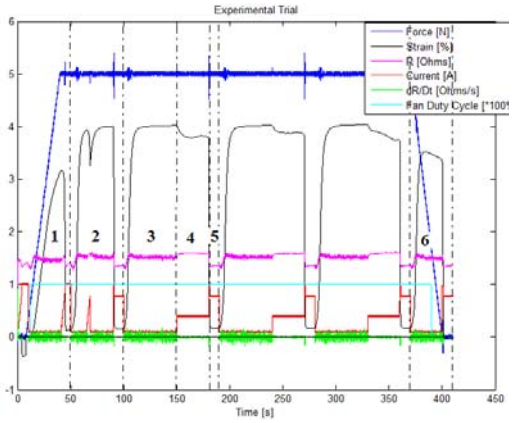

Figure 31 Experimental Trial

As can be seen from the figure, an experimental trial is divided into 6 phases, labelled 1 – 6, representing initialization, probing (which will not be defined for confidentiality reasons), cooling, priming, actuation and ending period. The cooling, priming, and actuation periods are repeated two more times to give three full actuation cycles per trial run. The three actuation cycles start at 180s, 270s and 360s. Measures are taken starting at these times and last for 30s each. The averages of these three cycles are then used to compare the TTC and AST of the two priming controller designs.

Due to the confidential nature of these experimental results, only relative performance gains are shown.

From the results obtained one could easily see the advantage of implementing the concept of priming. This was apparent from the significantly lower TTC and AST values obtained at lower actuation currents when experimenting with the two designs of the priming controller as compared to the values obtained when no priming was used. For example, when comparing the No Priming experiments with those of the original PI control, it was found that in the latter case lower average TTC and AST values were obtained at lower I_act in both the Fans Off and MF100 wind conditions. This agrees with postulates 1 and 2 that were formulated earlier in this section. For the MF50 wind condition, despite the fact that the average I_act obtained in PI control experiments was 2.7% larger than that obtained in No Priming and yielded an average AST that

was 5.75% larger, it did have an average TTC that was about 47% smaller than that in the No Priming experiments. The same thing applied when comparing the values obtained from the experiments implementing the proposed hybrid controller and No Priming. Whereas I_act and the average AST in the former were 2% and 11% larger respectively, the average TTC was almost 38% lower than in No Priming.

Comparing between the original PI control and the proposed hybrid controller was however more complex. In the Fans Off condition, although the hybrid controller yielded a lower TTC and AST, it did so using a higher I_act. While the average TTC and AST values obtained using the original PI controller were 8.13% and 13.3% larger than those obtained using the hybrid controller, I_act of the former was 2.4% less. Therefore, there is a possibility that for a higher I_act in the hybrid controller, lower TTC and AST values can be achieved. The case of the MF50 wind condition was the exact opposite. Here, the original PI controller yielded lower TTC and AST values but at a larger I_act. Therefore, increasing I_act in the hybrid controller will decrease TTC and AST possibly to values that are lower than those obtained using the original PI controller. Finally, concerning the MF100 wind condition, the original controller yielded a smaller average TTC compared to that obtained using the hybrid controller at a lower I_act. On the other hand, it suffered from a larger average AST. Nevertheless, since the average I_act in the hybrid controller was less than the one used in the original controller, it can be increased reducing the average AST and at the same time reducing the average TTC further. Consequently, given the above measurements, it was difficult to conclude which priming controller design is more effective and an extra performance measure was required.

Since the primary goal of either controller is to maintain consistent actuation time regardless of ambient air flow conditions, another measure to compare the two controllers in question would be to calculate how much the average TTC and AST values change under MF50 and MF100 wind conditions compared to the Fans Off condition as well as to one another. Tables 2 & 3 depict these percentages.

	TTC	AST
Percentage increase of MF50 over Fans Off	102%	33%
Percentage increase of MF100 over Fans Off	97.3%	24%
Percentage increase of MF100 over MF50	-2.35%	-7.3%

Table 2 The percentage change in TTC and AST between the 3 wind conditions for the proposed hybrid controller

	TTC	AST
Percentage increase of MF50 over Fans Off	58.125%	10.4%
Percentage increase of MF100 over Fans Off	68.75%	11.4%
Percentage increase of MF100 over MF50	6.72%	0.9%

Table 3 The percentage change in TTC and AST between the 3 wind conditions for the original PI controller

Comparing the percentages in Tables 2 & 3, one can conclude that the original priming controller is more effective at attempting to maintain consistent actuation periods under the different air flow conditions.

IX. Conclusions and Future Work

One advantage of using the hybrid controller is that, whereas the original priming controller design faces the paradox as to whether the decrease in the resistance value is due to actuation or to the wire cooling naturally, this is not the case with the proposed controller design. The situation the wire is experiencing (actuation or natural cooling) can be determined from the error e(t) and its derivative $\dot{e}(t)$. For example, if e(t) is positive and $\dot{e}(t)$ is negative then the wire is cooling. If e(t) is positive and $\dot{e}(t)$ is positive big, then the wire has undergone actuation.

Another thing to note is that despite the fact that the design of the original PI controller was more effective at maintaining consistent, and under some wind conditions lower actuation periods, the values obtained using the proposed hybrid controller were very promising and comparable to those obtained using the PI controller. Thus, using fuzzy logic in the design of the priming controller is a plausible idea. In fact, since the design of the hybrid controller that yielded the best results was achieved through trial and error, there is no guarantee that this is the optimal solution. Consequently, as future work, one could use genetic algorithms to find the optimum membership functions and fuzzy set rules as these may possibly yield results that are even better than those obtained from the original PI controller. One possibility would be to follow the procedure outlined in [23] whereby Homaifar et al. simultaneously design membership functions and rule sets for fuzzy controllers particularly as these two components are interdependent.

Finally, another recommendation for future work is concerned with the ambient conditions. Although the mini-fan was used to provide different convection coefficients by changing the wind speeds, this cannot be considered a proxy for varying ambient temperatures. Since the effect of priming is anticipated to be more evident under different temperatures, a further refinement to the experiment would be to run it outdoors in summer and winter and compare the results obtained from the two different priming controller designs.

REFERENCES

[1] D. R. Reynolds and P. Kloucek, "Numerical Modeling of Nonlinear Thermodynamics in SMA Wires", *Eighth Copper Mountain Conference on Iterative Methods*, March 2004

[2] 2001 SMA/MEMS Research Group, "Shape Memory Alloys", available online at http://www.cs.ualberta.ca/~database/MEMS/sma_mems/sma.html [accessed on November 14th, 2007]

[3] C. Mavroidis, C. Pfeiffer and M. Mosley, "Conventional Actuators, Shape Memory Alloys, and Electrorheological Fluids", available online at http://www.resonancepub.com/actuator.htm [accessed on March 2nd, 2008]

[4] K. Ikuta, "Micro/miniature shape memory alloy actuator", *IEEE International Conference on Robotics and Automation*, Vol. 3, pp. 2156-2161, May 1990

[5] S. B. Choi, Y. M. Han, J. H. Kim and C. C. Cheong, "Force Tracking control of a flexible gripper featuring shape memory alloy actuators", *Mechatronics*, Vol 11, pp. 677-690, 2001

[6] J. L. Pons, D. Reynaerts, J. Peirs, R. Ceres and H. VanBrussel, "Comparison of Different Control Approaches to Drive SMA Actuators", *International Conference on Advanced Robotics*, pp. 819-824, July 1997

[7] G. Song, B. Kelly and B. N. Agrawal, "Active position control of a shape memory alloy wire actuated composite beam", *Smart Material Structures*, pp. 711-716, August 2000

[8] C. A. Dickinson and J. T. Wen, "Feedback Control using Shape Memory Alloy Actuators", *Journal of Intelligent Material Systems and Structures*, Vol 9, pp. 242-250, April 1998

[9] N. Ma, G. Song, and H-J Lee, "Position control of shape memory alloy actuators with internal electrical resistance feedback using neural networks", *Smart Materials and Structures*, Vol 13, p777–783, June 2004

[10] C. A. Dickinson, D. C. Hughes and J. T. Wen, "Hysteresis in shape memory alloy actuators: the control issues", *Proceedings of the 1996 Mathematics and Control in Smart Structures Conference*, Vol 2715, pp. 494-506, 1996

[11] R. Gorbet, "Control of Hysteretic Systems with Preisach Representations", Doctoral thesis, University of Waterloo, Waterloo, ON, 1997

[12] M. H. Elahinia and H. Ashrafiuon, "Nonlinear Control of a Shape Memory Alloy Actuated Manipulator", *Transactions of the American Society of Mechanical Engineers*, Vol 124, pp. 566-575, October 2002

[13] M. Hashimoto, M. Takdeda, H. Sagawa, I. Chiba and K. Sat, "Application of Shape Memory Alloy to Robotic actuators", Vol 2, pp. 3-25, 1985

[14] K. Ikuta, M. Tsukamoto and S. Hirose, "Shape Memory Alloy Servo Actuator System with Electric Resistance Feedback and Application to Active Endoscope", *Proceedings of the 1988 IEEE International Conference on Robotics and Automation*, Vol 1, pp. 427-430, 1988

[15] D. Madill and D. Wang, "Modeling and L2-Stability of a Shape Memory Alloy Position Control System", *IEEE Transaction on Control Systems Technology*, Vol 6, No 4, pp. 473-481, 1998

[16] N. Ma and G. Song, "Control of shape memory alloy actuator using pulse width modulation", *Smart Materials and Structures*, Vol 12, pp. 712-719, 2003

[17] S. Tafazoli, M. Leduc and X. Sun, "Hysteresis Modeling using Fuzzy subtractive modeling", *International Journal of Computational Cognition*, Vol 4, pp. 15-27, September 2006

[18] G. Mester, "Neuro-Fuzzy-Genetic Controller Design for Robot Manipulators", in *Proceedings of the 21st International Conference on Industrial Electronics, Control and Instrumentation*, 1995, Vol. 1, pp. 87-92

[19] D. Grant and V. Hayward, 'Variable Structure Control of Shape Memory Alloy Actuators', *IEEE Control Systems Magazine*, Vol 17, No 3, pp. 80-88, 1997

[20] M. Y. Cheng and C. H. Ko, "A genetic-fuzzy-neuro model encodes FNNs using SWRM and BRM", *Engineering*

Applications of Artificial Intelligence, Vol. 19, pp. 891-903, 2006

[21] A. Visioli, *Practical PID Control*, London: Springer, 2006, pp. 61 – 91

[22] L. Zheng, "A practical guide to tune of proportional and integral (pi) like fuzzy controllers", in *Proceedings of the IEEE International Conference on Fuzzy Systems*, pp. 633-640, 1992

[23] A. Homaifar and E. McCormick, "Simultaneous Design of Membership Functions and Rule Sets for Fuzzy Controllers Using Genetic Algorithms", *IEEE Transactionson Fuzzy Systems*, Vol. 3, No. 2, pp. 129-139, 1995